2008

Study of left-handed materials

Jiangfeng Zhou
Iowa State University

Study of left-handed materials

by

Jiangfeng Zhou

A dissertation submitted to the graduate faculty

in partial fulfillment of the requirements for the degree of

DOCTOR OF PHILOSOPHY

Major: Electrical Engineering

Program of Study Committee:
Costas M. Soukoulis, Co-major Professor
Gary Tuttle, Co-major Professor
Jinmin Song
Rana Biswas
Mani Mina

Iowa State University

Ames, Iowa

2008

TABLE OF CONTENTS

LIST OF FIGURES

ACKNOWLEDGMENTS

First and foremost, I would like to thank my advisors Prof. Costas Soukoulis and Prof. Gary Tuttle, who provide me the great opportunity to pursue my study and complete my thesis at Iowa State University. I am deeply indebted to them for their enthusiasm, encouragement, patience, guidance, and financial support, which helped me during my research and the writing of this thesis. Without their support, this thesis would not have been possible.

I would like to express my gratitude to Prof. Rana Biswas, Prof. Jiming Song, and Prof. Mani Mina, for serving on my PhD examination committee. The knowledge I learned during my courses with Prof. Song, Prof. Biswas, and Prof. Mina was very valuable to my research.

My colleagues from Iowa State University supported and helped me so much in my research work. Especially, I thank Dr. Thomas Koschny for kindly and patiently answering my questions. I benefited greatly from discussions with him on various research projects. I would like to thank my office mate, Lei Zhang, for her kind help and discussions during my course study and research. I also thank Dr. Marcus Diem for his helpful discussions and suggestions.

Finally, and very importantly, I wish to thank my family for their constant support.

ABSTRACT

Left handed materials (LHMs) are artificial materials that have negative electrical permittivity, negative magnetic permeability, and negative index of refraction across a common frequency band. They possess electromagnetic (EM) properties not found in nature. LHMs have attracted tremendous attention because of their potential applications to build the perfect lens and cloaking devices. In the past few years there has been ample proof for the existence of LHMs in the microwave frequency range. Recently, researchers are trying hard to push the operating frequency of LHMs into terahertz and the optical regime.

In this thesis, we start with the theoretical prediction of left handed materials made by Veselago 40 years ago, introducing the unique electromagnetic properties of the left handed materials. After discussing the realization of LHMs by the split ring resonators (SRRs) and wire designs, we briefly review the development of LHMs from microwave frequency to the optical regime. We discuss the chiral metamaterial, which provides an alternative approach to realize negative refractive index.

In Chapter 2, we discuss the electromagnetic properties of the SRRs and the breakdown of linear scaling properties of SRRs at infrared and optical frequencies. By discussing the current modes, and the electric and magnetic moments, we study three resonance modes of SRR with respect to different polarizations of EM waves. Through numerical simulations, we find the breakdown of linear scaling, due to the free electron kinetic energy for frequencies above 100 THz. This result is important. It proves that researchers cannot push metamaterials into the optical regime by just scaling down the geometrical size of metamaterial designs used at low frequency.

Due to the breakdown of the linear scaling property, a much smaller structure size of LHMs

design is required in the optical regime, so new designs with simpler topology are needed.

In Chapter 3, we discuss a short wire pair design, which has a distinct advantage over conventional SRRs. We systemically study the electromagnetic properties of the short wire pair design. We determine the criteria overlaps the electric and magnetic resonances of short wire pairs. Using an H-shaped short wire pairs design, we demonstrate negative refractive index experimentally.

In Chapter 4, we introduce a LHM design using short wire pairs with long wires, which avoid the difficulty of overlapping the electric and magnetic resonances. We also discussed the relationship between three important LHM designs suitable for the optical regime: double gap SRRs, the short wire pairs, and the fishnet structure.

Compared to LHMs at microwave frequencies, the current designs at optical frequencies suffer from high losses which limit their potential applications in the area requiring low losses, such as the perfect lens. In Chapter 5, we investigate the role of losses of the short wire pairs and the fishnet structures. We find the losses can be reduced substantially by increasing the effective inductance to capacitance ratio, L/C, especially at THz frequencies and in the optical regime.

CHAPTER 1. LEFT-HANDED MATERIALS: THE CONCEPT AND THE HISTORY

About 40 years ago, a Russian scientist, Victor Veselago, had the idea that materials with negative refractive indices can bend light into the backward direction and behave in many other counterintuitive ways [2]. However, due to the absence of such materials in nature, this idea has been silent for four decades. Until 10 years ago, Sir J. B. Pendry proposed artificial designs that can achieve negative permeability. For the first time, this brought Veselago's idea into reality and opened up the new field of left-handed materials.

1.1 The Concept of Left-Handed Materials

The term "left-handed material" (LHM) was first introduced by Veselago [2] in 1968, who predicted there exists such a medium in which the electric field, **E**, the magnetic field, **H**, and the wave vector, **k**, form a left-handed orthogonal set. Left-handed materials (LHMs), which in a wider sense, are also referred to as negative index materials (NIMs), simultaneously have negative permittivity, ϵ, negative permeability, μ, and negative refractive index, n, over a common frequency band. Let's follow Veselago's theoretical work and consider such a medium.

1.1.1 Theoretical prediction of left-handed materials

To investigate the electromagnetic properties of such a medium, it was first studied how the electromagnetic wave behaves when $\epsilon < 0$ and $\mu < 0$. The source-free Maxwell equations and the constitutive relations in an isotropic medium are

$$\begin{aligned} \nabla \times \mathbf{E} &= -\frac{\partial \mathbf{B}}{\partial t} \\ \nabla \times \mathbf{H} &= \frac{\partial \mathbf{D}}{\partial t} \end{aligned} \tag{1.1}$$

and

$$\mathbf{B} = \mu\mathbf{H}$$
$$\mathbf{D} = \epsilon\mathbf{E}. \tag{1.2}$$

Looking for plane wave solutions, i.e., all fields are proportional to $e^{\mathrm{i}(\mathbf{kz}-\omega t)}$, the equations in (1.1) reduce to

$$\begin{aligned} \mathbf{k}\times\mathbf{E} &= \omega\mu\mathbf{H} \\ \mathbf{k}\times\mathbf{H} &= -\omega\epsilon\mathbf{E}. \end{aligned} \tag{1.3}$$

It can be seen from Eq. (1.3) that when $\epsilon < 0$ and $\mu < 0$, **E**, **H** and **k** form a left-handed triplet of vectors. This is the reason that the medium is named as the left-handed medium.

The direction of the energy flow is given by the Poynting vector,

$$\mathbf{S} = \mathbf{E}\times\mathbf{H}. \tag{1.4}$$

The non-zero Poynting vector, always forms a right-handed coordinate system with **E** and **H**, independent on the signs of ϵ and μ. Therefore, in a left-handed material, the wave vector, **k**, is in the opposite direction of the energy density flow, **S**. Such a wave is called *backward wave*. In contrast, in a normal right-handed material (RHM), the wave vector, **k**, and the energy flow, **S**, are in the same direction and the wave is a *forward wave*. The directions of **E**, **H**, and **k** for both RHM and LHM are shown in Fig. 1.1.

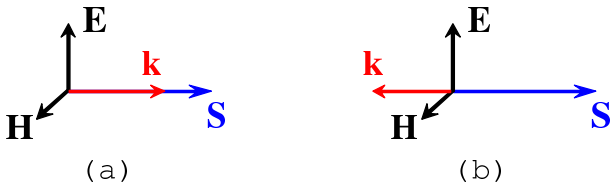

Figure 1.1 (a) RHM, in which the **E**, **H** and **k** form a right-handed vector system, and the wave vector **k** and energy density flow **S** are in the same direction. (b) LHM, in which the **E**, **H**, and **k** form a left-handed vector system, and the wave vector, **k**, and energy density flow, **S**, are in the opposite direction. .

The dispersion relation of an isotropic medium is given by

$$k^2 = \omega^2\epsilon\mu. \tag{1.5}$$

In a lossless isotropic medium, where $\epsilon, \mu \in \mathcal{R}$, a wave can either propagate or decay depending on the signs of ϵ and μ. When $\epsilon \cdot \mu > 0$, $k = \omega\sqrt{\epsilon\mu}$, and the wave propagates; on the other hand, when $\epsilon \cdot \mu < 0$, $k = \mathrm{i}\omega\sqrt{|\epsilon\mu|}$, and the wave decays exponentially. Figure 1.2 shows a plane of ϵ and μ, divided into four quadrants, based on the signs of ϵ and μ. The first quadrant contains the majority of dielectrics, where ϵ and μ are positive. Substances with one negative constitutive parameter are easy to find in nature. For example, the plasma medium, such as ionized gas or free electrons gas in metal, has negative ϵ all the way up to the plasma frequency, and belongs to the second quadrant. Materials such as ferromagnets and antiferromagnets can have negative magnetic permeability near the ferromagnetic resonance and belong to the fourth quadrant. However, left-handed materials, which belong to the third quadrant, do not exist in nature. Until recently, artificial structures with simultaneous negative ϵ and μ were

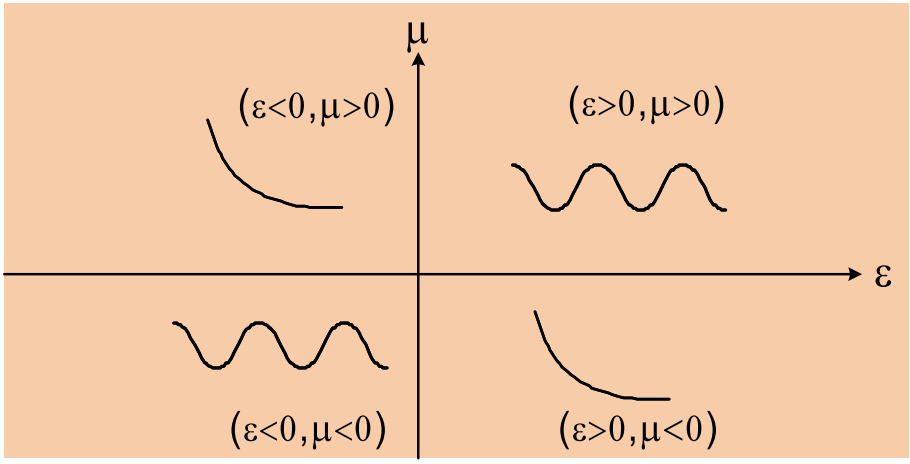

Figure 1.2 ϵ and μ coordinate system. Wave propagate in I and III quadrant, where $\epsilon \cdot \mu > 0$ and attenuate in II and IV quadrant, where $\epsilon \cdot \mu < 0$.

proposed theoretically [3, 4] and investigated experimentally [5, 6] at microwave frequencies. In these designs, the negative ϵ and μ were realized separately by periodically arranging long wires and split ring resonators (SRRs), respectively, and then the composite structures have both negative ϵ and μ over a common frequency band, and, therefore, have negative n as well. Very recently, researchers have made a great deal of effort on moving the working frequency from microwave frequency all the way up to optical frequency.

1.1.2 Dispersive and dissipative natures of LHMs

The negative values of ϵ and μ can be realized simultaneously, only if the material has frequency dispersion. This can be seen immediately from the formula of the energy density of non-dispersive media,

$$W = \epsilon E^2 + \mu H^2. \tag{1.6}$$

If $\epsilon < 0$ and $\mu < 0$, the energy density, W, would be negative. When there is frequency dispersion, i.e., $\epsilon = \epsilon(\omega)$ and $\mu = \mu(\omega)$, the total energy density is given by Ref. [7],

$$W = \frac{\partial(\epsilon\omega)}{\partial\omega} E^2 + \frac{\partial(\mu\omega)}{\partial\omega} H^2. \tag{1.7}$$

The energy density is always positive if

$$\begin{aligned} \frac{\partial(\epsilon\omega)}{\partial\omega} &= \epsilon + \omega\frac{\partial\epsilon}{\partial\omega} > 0 \\ \frac{\partial(\mu\omega)}{\partial\omega} &= \mu + \omega\frac{\partial\mu}{\partial\omega} > 0. \end{aligned} \tag{1.8}$$

This clearly indicates that ϵ and μ can be simultaneously negative, given the medium is frequency *dispersive* and Eq.(1.8) is fulfilled. Therefore, a left-handed material must be *dispersive*.

Moreover, a medium with frequency dispersion is always dissipative. Following the causality principal, the real and imaginary parts of the permittivity, $\epsilon(\omega) = \epsilon'(\omega) + \mathrm{i}\epsilon''(\omega)$, are related by the Kramers-Kronig relations [7, 8]:

$$\begin{aligned} \frac{\epsilon'(\omega)}{\epsilon_0} &= 1 + \frac{2}{\pi} P \int_0^\infty \frac{\omega'\epsilon''(\omega')/\epsilon_0}{\omega'^2 - \omega^2} \mathrm{d}\omega' \\ \frac{\epsilon''(\omega)}{\epsilon_0} &= -\frac{2\omega}{\pi} P \int_0^\infty \frac{\epsilon'(\omega')/\epsilon_0 - 1}{\omega'^2 - \omega^2} \mathrm{d}\omega', \end{aligned} \tag{1.9}$$

where P stands for the principal value of the integration. The real and imaginary parts of permeability, $\mu(\omega) = \mu'(\omega) + \mathrm{i}\mu''(\omega)$, obey the same relations. Since the imaginary parts of the permittivity, the permeability and the refractive index always coexist with the real parts in dispersive media, the left-handed material must be dissipative. A recent study [9, 10] shows a lower limit of electric and magnetic losses in the left-handed material. If losses are eliminated or significantly reduced for any reason, including compensated by active (gain) media, then the negative refractive will disappear.

1.1.3 Negative refraction

The reflection and the refraction of light at a plane interface between two media of different dielectric properties are familiar phenomena. The refractive angle, the transmission, and the reflection coefficients are determined by Snell's Law and Fresnel formulas [8]. Many interesting effects happen at the interface, such as total internal reflection and the Brewster angle effect.

Now, let's consider the refraction that occurs at the interface between a right-handed medium and a left-handed medium. Applying the boundary conditions for the electric and the magnetic fields, and considering the consistency of the energy flow across the interface, one obtains *negative refraction*. Figure 1.3 shows the reflection and refraction of an s-polarized EM wave at the interface between an RHM and an LHM. The relation between the refractive

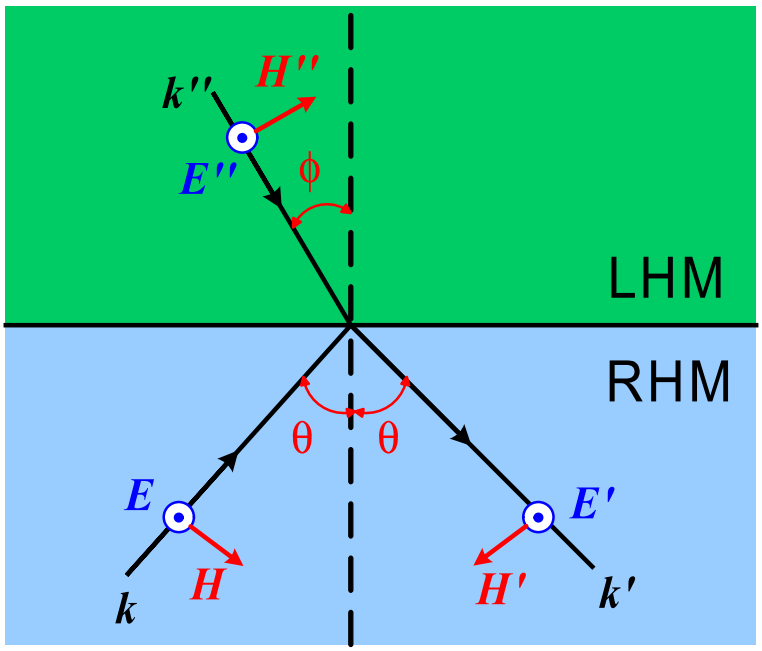

Figure 1.3 The reflection and refraction of an s-polarized (with **H** in the plane given by the incident rays and incident normal) EM wave at the interface between a right-handed medium and a left-handed medium. The incident EM wave, **k**, the reflect wave, **k**′, and the refractive wave, **k**″, are shown.

angle, ϕ, and the incident angle, θ, is determined by Snell's Law:

$$\frac{\sin(\phi)}{\sin(\theta)} = \frac{n_2}{n_1} = \frac{-\sqrt{\epsilon_2\mu_2}}{\sqrt{\epsilon_1\mu_1}}, \tag{1.10}$$

where n_1, ϵ_1, and μ_1 are the refractive index, permittivity and permeability of the RHM, respectively, and n_2, ϵ_2, and μ_2 are corresponding quantities for the LHM. According to the boundary condition and energy flow, we must choose the negative sign of the square root for the LHM, i.e., $n_2 = -\sqrt{\epsilon_2 \mu_2}$ for the case $\epsilon_2 < 0$ and $\mu_2 < 0$. The negative sign in Snell's Law Eq.(1.10) indicates the refractive wave undergoes the negative direction.

One may also notice in Fig. 1.3 that the wave vector of the refractive wave, $\mathbf{k}''$, heads toward the interface, which indicates that the refractive wave travels along the backward direction. On the other hand, the energy flows away from the interface. Therefore, the energy velocity, $\mathbf{v}_e$, is along the opposite direction of the phase velocity, $\mathbf{v}_p$.

1.1.4 Phase velocity, group velocity, and energy velocity

As mentioned previously, the phase velocity and the energy velocity are anti-parallel in left-handed materials. In this section, we will discuss three velocities[1]: the phase velocity, $\mathbf{v}_p$, the group velocity, $\mathbf{v}_g$, and the energy velocity, $\mathbf{v}_e$. We will show that both the group velocity and the energy velocity are along the opposite direction of the phase velocity in LHMs [11, 12] and the energy velocity is the same as the group velocity. Following the same definition as for right-handed materials, the phase velocity in left-handed materials is given by

$$\mathbf{v}_p = \frac{\omega}{|\mathbf{k}|}\hat{\mathbf{k}}, \tag{1.11}$$

where $\hat{\mathbf{k}} = \mathbf{k}/|\mathbf{k}|$ is the unit vector along $\mathbf{k}$ direction. The group velocity is defined as $\mathbf{v}_g = \nabla_k \omega = \frac{\mathrm{d}\omega}{\mathrm{d}|\mathbf{k}|}\hat{\mathbf{k}}$. Using the dispersion relation $\mathbf{k} = \frac{\omega}{c_0}|n|\hat{\mathbf{k}}$, one can obtain

$$\mathbf{v}_g = \frac{\mathbf{v}_p}{\alpha}, \tag{1.12}$$

where $\alpha = 1 + \frac{\omega}{n}\frac{\mathrm{d}n}{\mathrm{d}\omega}$, which has the same sign as n.

The energy velocity is given by $\mathbf{v}_e = \bar{\mathbf{S}}/\bar{w}$ [13], where $\bar{\mathbf{S}}$ and $\bar{w}$ are the time average Poynting vector and time average power density, respectively. It can be shown that the energy velocity has the following relation to the phase velocity

$$\mathbf{v}_e = \frac{\mathbf{v}_p}{\alpha}. \tag{1.13}$$

[1] Detail discussions are given by Appendix

Eqs. (A.5) and (A.8) show the group velocity and the energy velocity are identical. In addition, since α has the same sign as the refractive index, n, in left-handed materials, both the group velocity and the energy velocity are in the opposite direction of the phase velocity.

1.2 Realization of LHMs

Although left-handed materials have been theoretically predicted and studied a few decades ago, it was only recently that such materials were realized experimentally after Sir J. B. Pendry proposed a *split ring resonators* (SRRs) design [4], which can provide negative permeability, μ, around its resonance frequency, ω_m. Together, with a continuous wires array [3] which gives negative permittivity, ϵ, up to the plasma frequency, ω_p, due to the plasmas response, the composite structure, SRRs plus wires give a negative refractive index, n.

1.2.1 Negative permittivity medium and negative permeability medium

In left-handed materials, negative permittivity and negative permeability can be realized separately. As discussed in section 1.1.1, negative permittivity materials exist in nature. Plasma media, e.g., all the metals, have negative permittivity up to the plasma frequency. However, the usage of solid metal in LHM is limited by the fact that the absolute value of the negative ϵ is too large at the target frequency, i.e., from microwave to optical frequency. So, one must determine a method to scale the value of ϵ to a reasonable value on the order of -1. Usually the permittivity of a metal can be described by the Drude model [8],

$$\epsilon(\omega) = 1 - \frac{\omega_p^2}{\omega(\omega + \mathrm{i}\omega_c)}, \tag{1.14}$$

where ω_c is the damping frequency, and ω_p is the plasma frequency given by

$$\omega_p^2 = \frac{ne^2}{\epsilon_0 m_{\text{eff}}}, \tag{1.15}$$

where n is the electron density and m_{eff} is the effective mass of free electrons.

Plasma frequency is extremely high in metals, e.g., silver has $\omega_p = 2\pi \times 2184$ THz and $\omega_c = 2\pi \times 4.35$ THz. As a result, the absolute value of permittivity is extremely large, $\mathrm{Re}(\epsilon) < -10^8$, and, therefore, not suitable for LHM. Pendry proposed a wire array design, which

can significantly decrease the plasma frequency and realize negative permittivity $\epsilon \approx -1$ at microwave frequencies. Moreover, the value of ϵ and the frequency are completely controllable via the geometrical parameters [3]. As shown in Fig. 1.4(a), the wire array structure consists of periodically arranged "infinite" long wires with separation, a, and radius, r. The effective permittivity of wire arrays is similar to the permittivity in bulk metal, except the plasma frequency is much lower. As shown in Fig. 1.4 (b), the real part of permittivity, $\mathrm{Re}(\epsilon(\omega))$, is negative under the plasma frequency, ω_p, which falls in the region that can be utilized in left-handed materials.

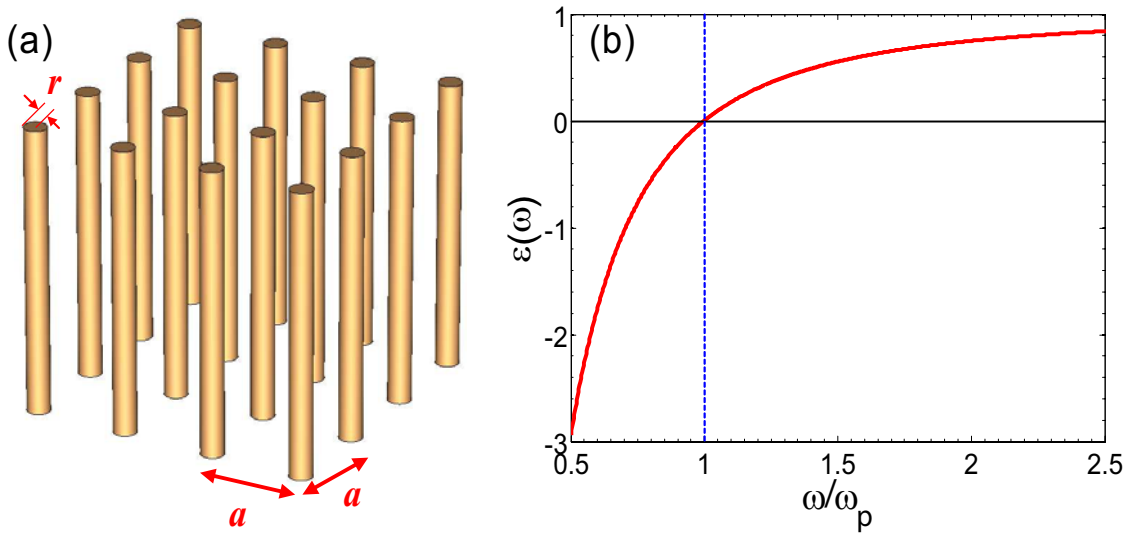

Figure 1.4 (a) The metallic wire arrays with radius of wire r and separation between wires a. (b) The real part of the permittivity, $\mathrm{Re}(\epsilon(\omega))$, as a function of the frequency, ω/ω_p. $\mathrm{Re}(\epsilon(\omega))$ increases with frequency from negative values at low frequency and crosses over zero at the plasma frequency, ω_p.

Two effects contribute to the decrease of the plasma frequency of the wire array [3]. First, the effective electron density is significantly diluted, due to the factor that the volume occupied by the metallic thin wire is much less than the vacuum space. The effective electron density can be obtained by the ratio of the volume of the metal and the vacuum, $n_{\mathrm{eff}} = n\pi r^2/a^2$. On the other hand, due to self-inductance of the thin wires, the motion of the electrons slowed down. The magnetic field energy, which is proportional to $\ln(a/r)$, corresponding to this self-inductance equivalently increases the effective mass of electrons substantially. Combining those

two effects, the plasma frequency, ω_p, of the wire array is significantly lower than for the bulk metal. The plasma frequency, ω_p, of the wire array is given by

$$\omega_p^2 = \frac{2\pi c_0^2}{a^2 \ln(a/r)}. \tag{1.16}$$

One can see that the plasma frequency, ω_p, only depends on the radius of wire, r, and the lattice constant, a. By changing these geometric parameters, one can control the plasma frequency and therefore control the value of the permittivity.

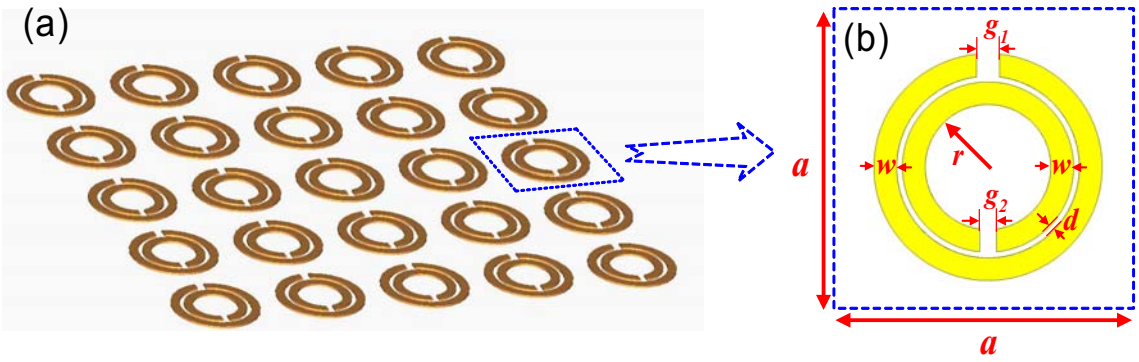

Figure 1.5 (a) The split ring resonator arrays (SRRs) with repeating distance, a. (b) Single unit cell of the SRR with geometric parameters given as following: radius of inner ring, r, the ring width, w, the gap between inner and outer ring, d, and the gap on the inner and outer ring, g_1 and g_2.

Although negative permittivity can be realized by plasma medium such as metallic structures, one cannot achieve the negative medium, due to the fact that no material exists in nature with negative permeability. Subsequently, Pendry proposed a split ring resonator (SRR) design [4], which can provide a narrow frequency band with negative permeability under certain polarization of incident EM wave. As shown in Fig. 1.5(a), the SRR arrays consist of periodically arranged arrays of double split ring structures, made from good conductors such as copper, with the lattice constant, a. Figure 1.5(b) shows the single unit cell of the SRRs. If we apply an incident EM wave with a magnetic field, $\mathbf{H}$, perpendicular to the plane of SRR, circular currents will be induced on both the inner and outer rings, and also charges will accumulate across the gaps in both the inner and outer rings, respectively. Thus, each individual SRR acts as a series LRC circuits with the inductance, L, of the rings and the capacitance, C, between

the two rings. The effective permeability, μ_{eff}, can be approximated as,

$$\begin{aligned} \mu &= 1 - \frac{A\omega^2}{\omega^2 - \omega_m^2 + \mathrm{i}\omega\Gamma_m}, \\ \omega_m &= \frac{3ac_0^2}{\pi \ln \frac{2w}{d} r^3}, \\ \Gamma_m &= \frac{2a\sigma}{r\mu_0}, \\ A &= \frac{\pi r^2}{a^2}, \end{aligned} \tag{1.17}$$

where μ_0 is the permeability in vacuum; ω_m and Γ_m are the resonance frequency and the damping factor, respectively. Both ω_m and Γ_m are functions of the geometric parameters, a, w, d, and r, and the conductivity, σ, of the metal. Figure 1.6 shows the effective permeability of SRRs array as a function of the frequency. Negative values of μ are achieved within a narrow frequency band above the resonance frequency, ω_m.

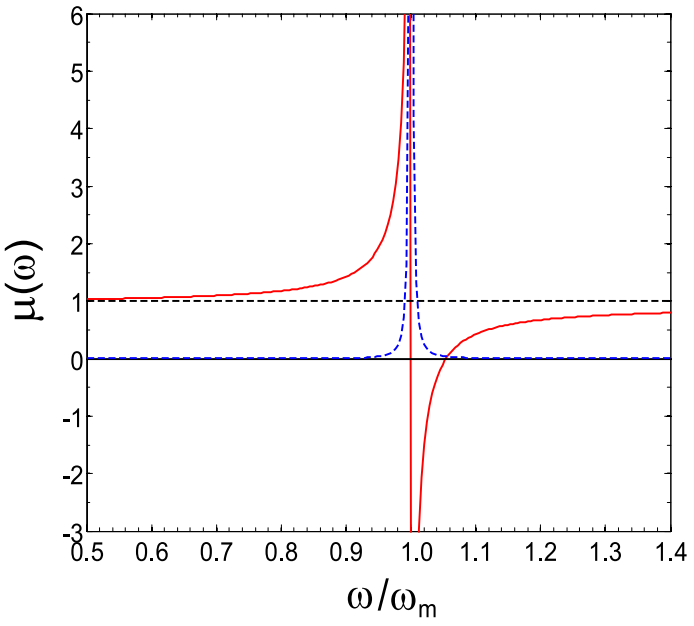

Figure 1.6 The real part (red solid) and the imaginary part (blue dashed) of the permittivity, $\mu(\omega)$, are functions of the frequency, ω/ω_m, where ω_m is the resonance frequency.

1.2.2 Effective medium theory

The wire and SRR arrays possess negative permittivity and negative permeability, respectively. Can we use these designs to obtain a negative permittivity and negative permeability medium? To answer this question, let us recall the concept of permittivity and permeability. The original objective in defining permittivity, ϵ, and permeability, μ, is to present a *homogeneous* view of the electromagnetic properties of a medium. The macroscopic electric and magnetic properties of a material, e.g., polarization and magnetization, are average behaviors of electrons and atoms in the external electric and magnetic fields of EM waves. In this sense, the normal materials are also composites, where the individual ingredients are atoms and molecules. The sizes of these ingredients are much smaller than the wavelength of EM waves.

So, we can consider periodic structures, defined by a unit cell with dimension, a, as a homogenous medium. The total EM properties of structures inside a unit cell will be considered as an effective response of the unit cell as a whole. Clearly, there must be some restrictions on the dimension of the unit cell, defined as follows:

$$a \ll \lambda, \tag{1.18}$$

If this condition is obeyed, the external EM wave will not "see" the fine details of each individual structure inside the unit cell, and the periodic structure can be considered as a homogenous medium. So, the effective permittivity and permeability are valid concepts. On the contrary, if this condition is not fulfilled, the internal structure of the unit cell could diffract and refract EM waves, which leads to material properties not seen in homogenous media.

1.2.3 Experimental realization of LHM

To obtain a substance with both negative electric permittivity and negative magnetic permeability simultaneously, a composite structure combining the long wire arrays and SRR arrays was proposed. Assuming these two structures will not interfere with each other, the composite structure will preserve both the negative permittivity from wires and negative permeability

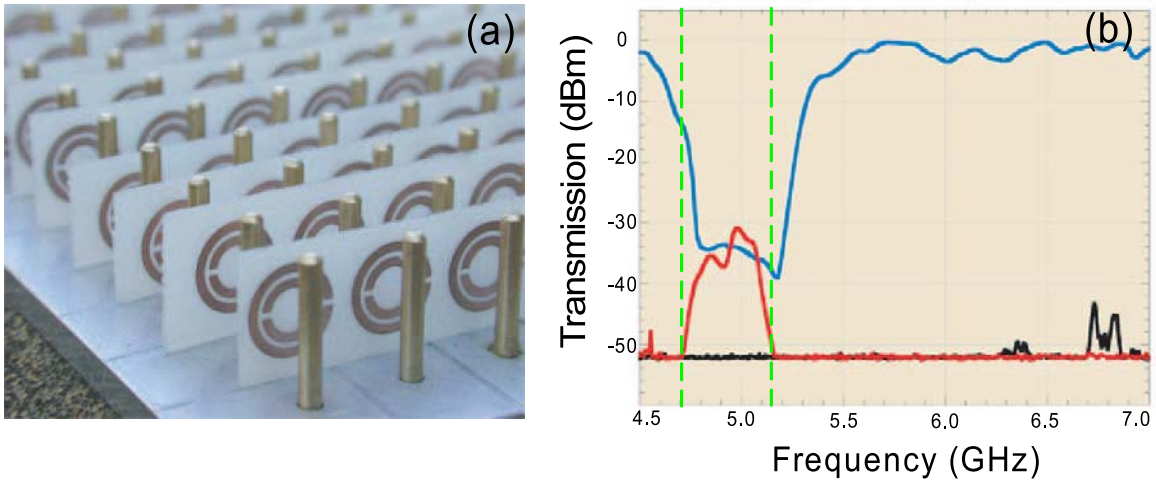

Figure 1.7 a) The composite LHM employed by Smith et al., which consists of SRRs, created by lithography on a circuit board, and metallic posts. b) The transmission coefficient of wires only (black), SRRs only (blue), and both wires, and SRRs (red). By adding the wire and SRRs together, a passband occurs where ϵ and μ are both negative.

from SRRs, and, therefore achieves a negative refractive index. The experimental demonstration of such a left-handed material was first accomplished by Smith et al. [5] in 2000 using the design shown in Fig. 1.7(a). In this work, the transmission of wire arrays alone, SRR arrays alone, and the combination of wire and SRR arrays were measured. As shown in Fig. 1.7(b), the stopband of the SRR structures caused by a magnetic resonance with the negative permeability, μ, disappeared when the wires arrays were added. Instead, a passband existed, where the effective permittivity, ϵ, and the effective permeability, μ, are both negative. Later on, various new LHM samples were fabricated and confirmed the existence of left-handed materials [14, 15, 16, 17, 18, 19, 20, 21, 22, 23, 24, 25]. The negative refraction was demonstrated by a two-dimensional left-handed medium shaped like a prism [6, 26]. In this experiment, a beam of microwaves was directed onto the flat surface of the prism, passed the LHM prism undeflected, and then refracted at the second surface of the prism. The refractive angle of the transmitted beam through the prism was measured. It was shown that the refractive beam bent toward

the "wrong" direction. The measured refractive angle was consistent with Snell's Law when n was assumed to be negative. Further experiments were performed by other groups [17, 21, 26], who confirmed this composite metamaterial design indeed exhibits left-handed behavior.

1.3 Characterization of Left-Handed Materials

In left-handed materials, negative permittivity and negative permeability are realized separately by wire arrays and SRR arrays, respectively. The composite metamaterials consisting of both wires and SRRs possess left-handed behavior. In early experiments, the transmission, T, of wires alone, T of SRRs alone, and T of the composite structure were measured. If a peak in the transmission of the composite structure was observed in the stopband for the wires alone and for the SRRs alone, then the peak was considered to be the left-handed peak. This is under the assumption that the wires and SRRs in the composite structures behave in the same manner as the medium consisting of wires alone or SRRs alone. However, this assumption is not always true. It has been shown that the effective plasma frequency, ω_p', in the composite materials is substantially lower than the plasma frequency of the wires, ω_p [27]. If the effective plasma frequency, ω_p', is lower than the magnetic resonance frequency, ω_m, then the peak in the transmission considered to be the left-handed peak is actually the right-handed peak with both $\epsilon > 0$ and $\mu > 0$. So, the transmission responses are not sufficient to distinguish the left-handed and the right handed behavior. There is a need to calculate the effective parameters explicitly.

In order to obtain the effective electromagnetic parameters of LHM, i.e., the effective permittivity, ϵ and the effective permeability, Smith et al. proposed a retrieval procedure [28]. The idea was to model the metamaterial as an *isotropic homogeneous* slab, and calculate the effective parameters, ϵ and μ, of the homogenous slab, from the measured or simulated metamaterial transmission, T, and the reflection, R, by using the theoretical formulas for the slab. The resonance behavior of the retrieved permeability and the negativeness of the retrieved permittivity were observed for the composite structure consisting of wire array and SRR array. However, further numerical studies showed the effective parameters differ considerably from

the theoretical prediction of Eqs. (1.14) and (1.17), respectively. The resonance/anti-resonance coupling was found in the extracted effective parameters [28, 29, 30, 31, 32]. The anti-resonance structure in the real part was accompanied by a negative imaginary part [31, 32]. In addition, truncated resonances were observed. These effects were interpreted as a periodicity effect, due to the periodic property of metamaterials [33]. Later on, the retrieval procedures for inhomogeneous metamaterials [34] and bi-anisotropic metamaterials [35] were studied for the case of asymmetric structures along the propagation direction of the EM wave and for a few special polarizations of SRRs, respectively.

1.4 The Development of LHM from Microwave Frequency to the Optical Regime

Since the first demonstration of an artificial left-handed material at microwave frequency [5] in 2000, researchers have made a great deal of effort on pushing operating frequency of LHM from microwave frequency all the way up to the optical regime. Figure 1.8 shows the progress of LHM developing from microwave frequency to optical regime [1].

By scaling down the geometric sizes of SRRs from a few millimeters to the order of one hundred nanometers, researchers from different groups have successfully fabricated and demonstrated the magnetic response of SRR structures operating at 1 THz [36], 2 THz [37], 100 THz [38], and 200 THz [39]. Due to substantial technical difficulties, the measurement of the transmission coefficient, T, of parallel incident EM wave with respect to the SRR plane is not realizable for micron and nanometer scale structures. Therefore, in most of the THz experiments, only a single layer of SRR structure was made and T was measured for the normal incidence of EM wave, utilizing the property of the electric coupling to magnetic resonance (EEMR) [40]. Using this approach, an electric resonance was observed at the magnetic resonance frequency, ω_m, and the existence of magnetic resonance was demonstrated indirectly.

At low frequency regimes, up to several THz, the magnetic resonance frequency scales reciprocally with respect to the structural size. At high frequencies, however, this linear scaling breaks down, due to the free electron kinetic energy [41, 42], negligible at low frequencies.

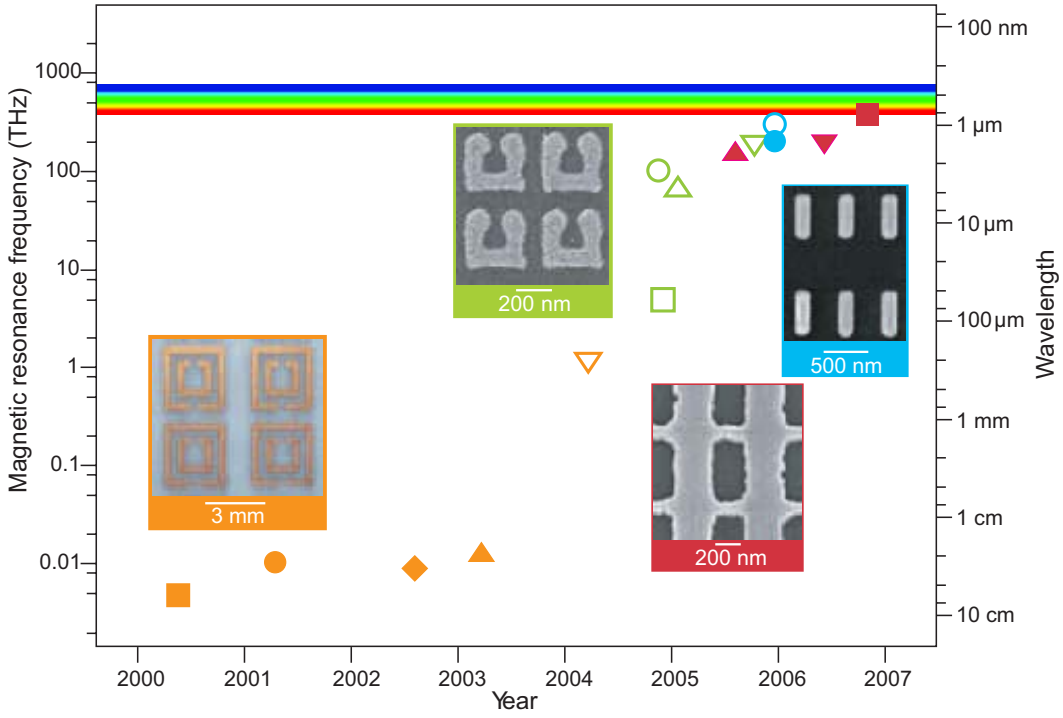

Figure 1.8 The progress in the negative permeability, μ, and negative index, n, materials development in the last seven years. The solid symbols denote $n < 0$; the open symbols denote $\mu < 0$. Orange: data from structures based on the double split-ring resonator (SRR); green: data from U-shaped SRR; blue: data from pairs of metallic short-wire pair; red: data from the "fishnet" structure. The four insets give pictures of fabricated structures in different frequency regions. Reprinted with permission from Ref. [1]. Copyright (2007) AAAS.

Above the linear scaling regime, the resonance frequency saturates, while the amplitude of the resonance permeability decreases, and ultimately ceases to reach a negative value. Because of the breakdown of the linear scaling, it is more difficult to increase the resonance frequencies. Much smaller geometric sizes and more complicated topologies, such as multiple gap SRRs are needed. For instance, the smallest SRR so far with the resonance frequency at 200 THz, has a width w=50 nm, which already reached the limit of current available nano-fabrication technique. Thus, researchers must look for alternative designs suitable for THz and optical regimes. The short wire pair designs were realized and published independently by two different groups in 2005 [43, 44, 45]. These designs show that pairs of metallic wires, separated by a dielectric spacer, can provide magnetic resonance and negative μ. The magnetic resonance originates

from the anti-parallel currents in the wire pairs and the opposite sign charges accumulated at the corresponding ends. For the short wire pair design, the incidence of EM waves is normal to the sample surface, which is much easier to implement experimentally in the optical regime compared to the parallel incidence for the conventional SRRs and wires.

In addition, the short wires also support electric resonance with $\epsilon < 0$, which results from the parallel current in the wires. Although short wire pairs can provide both the magnetic resonance and the electric resonance, overlapping these resonances is very difficult [46]. In order to obtain a left-handed material, additional structures providing negative permittivity are needed. One method is to introduce extra continuous wires next to the pairs [45], and another method is to change the shape of the wires. A fishnet structure was introduced [47, 48], realizing both $\epsilon < 0$ and $\mu < 0$ at infrared frequencies and later on in the optical regime [49]. The fishnet structure consists of double layers of infinite long metallic wire arrays along two orthogonal directions spaced by a dielectric spacer. The wires along the magnetic field, **H**, direction act as a magnetic resonator, providing negative permeability, μ, due to anti-parallel currents induced by the magnetic field of the incident electromagnetic wave. The wires along the electric field, **E**, direction of the incident electromagnetic wave excite the plasmonic response and produce negative permittivity ϵ. The fishnet and the short wire pair structures have intrinsic relationship with the SRRs. The transformation from the two-gap SRR to the short-wire pair and the fishnet structure have been studied in Ref. [46]. The fishnet structure was considered as the best LHM design in the optical regime, and a few variants of fishnet structures were studied in Refs. [50, 51].

1.5 Losses of LHM

Although recent development has realized left-handed materials in the optical regime, the current designs at high frequencies have many unsolved problems, which have limited their potential applications. Most importantly, both experiment and simulation results show that losses increase as the frequency increases.

In Fig. 1.9, the transmission loss of the existing metamaterials is presented in the unit of

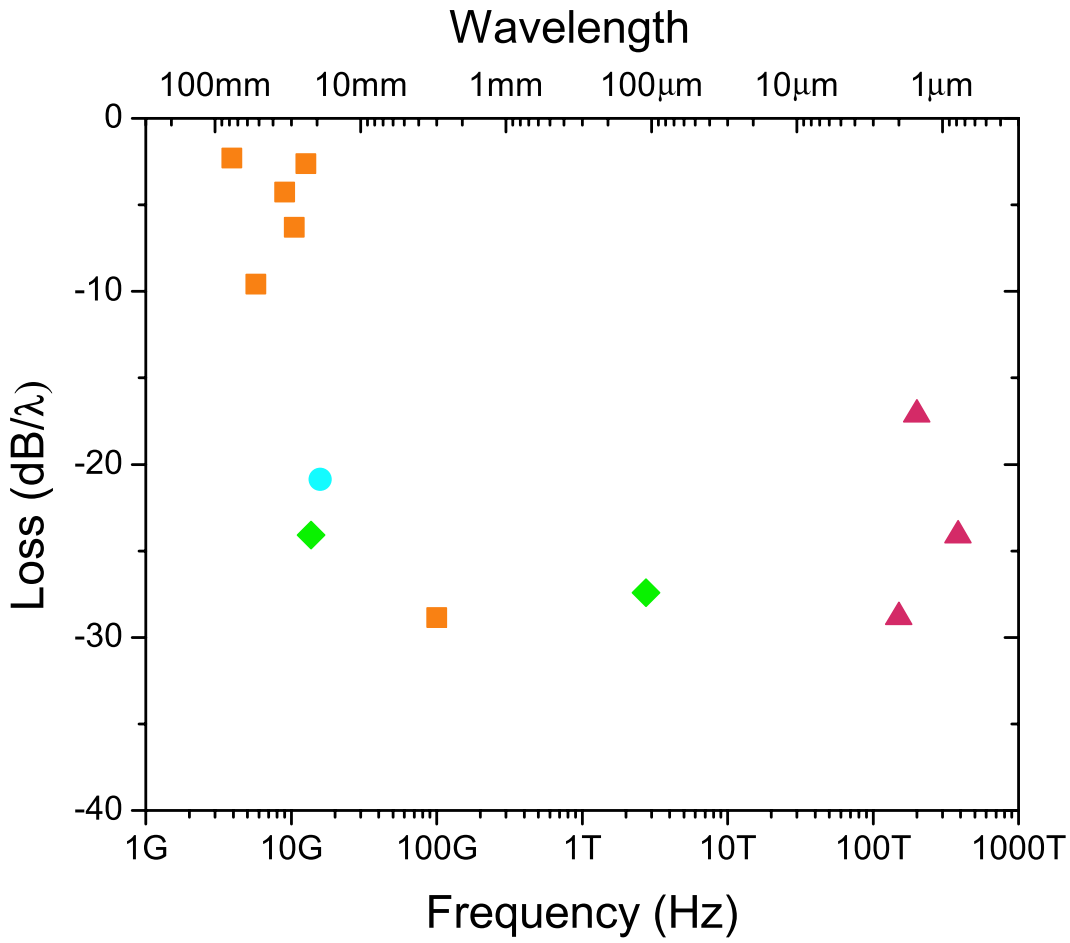

Figure 1.9 Transmission loss, in the unit of dB/λ versus frequency for all the existing experimental structures that show a negative n. Orange: data from structures based on the double split-ring resonator (SRR); green: data from U-shaped SRR; blue: data from pairs of metallic cut-wires; red: data from the "fishnet" structure. The symbols correspond to data shown in Fig. 1.8

dB/λ versus frequency [52]. The symbols in Fig. 1.9, from low to high frequency, correspond to experimental studies of LHM from microwave frequency to optics regime in Refs. [25, 51, 15, 6, 45, 53, 54, 55, 40, 56, 48, 49]. One can see clearly that the losses at low frequencies are small (of the order of 1-5 dB/λ). As the frequency increases, the loss increases, almost approaching 30 dB/λ. The loss was calculated from the experimental transmission values, measured for a given structure thickness. Another factor to measure loss, namely the figure of merit (FOM), is the ratio of real and imaginary parts of the refractive index, $|\mathrm{Re}(n)/\mathrm{Im}(n)|$, which drops from the order of 100 for SRRs at microwave frequency to 0.5 for the fishnet structure at optical

frequency [49, 57]. So, loss becomes a serious problem, limiting the potential applications of metamaterials such as the perfect lens [58, 59]. Therefore, we need to reduce the losses, especially at high frequencies.

One way to reduce loss is to use good conductors because losses in the LHM are dominated by metal losses. Silver exhibits the lowest losses at optical frequencies, due to the low damping frequency, ω_τ. Therefore the use of silver [56] instead of gold [48, 44, 47] will reduce the losses at similar frequencies. On the other hand, it is shown that the losses are closely related to the effective inductance, L, and the effective capacitance, C, in the RLC model of LHM. Increasing the effective inductance to capacitance ratio, L/C, will reduce the losses and increase the FOM substantially [60]. Using active medium [61] or active circuit parts [62] in the LHM design to compensate the loss was also proposed.

1.6 Chiral Metamaterials

Recently, chiral metamaterials were proposed as an alternative to realize negative refractive index [63, 64, 65]. Chiral metamaterials are metamaterials made of unit cells without symmetry planes. The unit cell size in a chiral metamaterial can be much smaller than the wavelength. It has been shown that backward waves exist in chiral media [63, 65]. A chiral material slab can focus the incident EM beams and can be used as a perfect lens [66, 67]. Canonical helix [65] and twisted Swiss-role metal structures [64] for microwave applications have been discussed as possible candidates to achieve negative refractive index. Later, the bilayer rosette shaped chiral metamaterial was proposed and fabricated at microwave frequency [68] and at optical regime [69, 70, 71]. It exhibited a very strong rotary power in the microwave, near-infrared and visible spectral ranges. For example, in the microwave spectral region, in terms of rotary power per wavelength, the bilayer structure rotates five orders of magnitude stronger than a gyrotropic crystal of quartz [68]. It has been shown that the strong gyrotropy originates from the magnetic resonance of the bilayer metallic structure, resulting from the anti-parallel current in the bilayer metal wires [72]. In this sense, the bilayer chiral structure is the chiral version of the material consisting of short wire pair [43, 45, 44]. Later, planar chiral structure [73, 74]

and chiral photonic crystal [75] were proposed and fabricated. More recently, a chiral SRR consisting of double layers of SRRs was proposed and expected to provide negative refractive index [76].

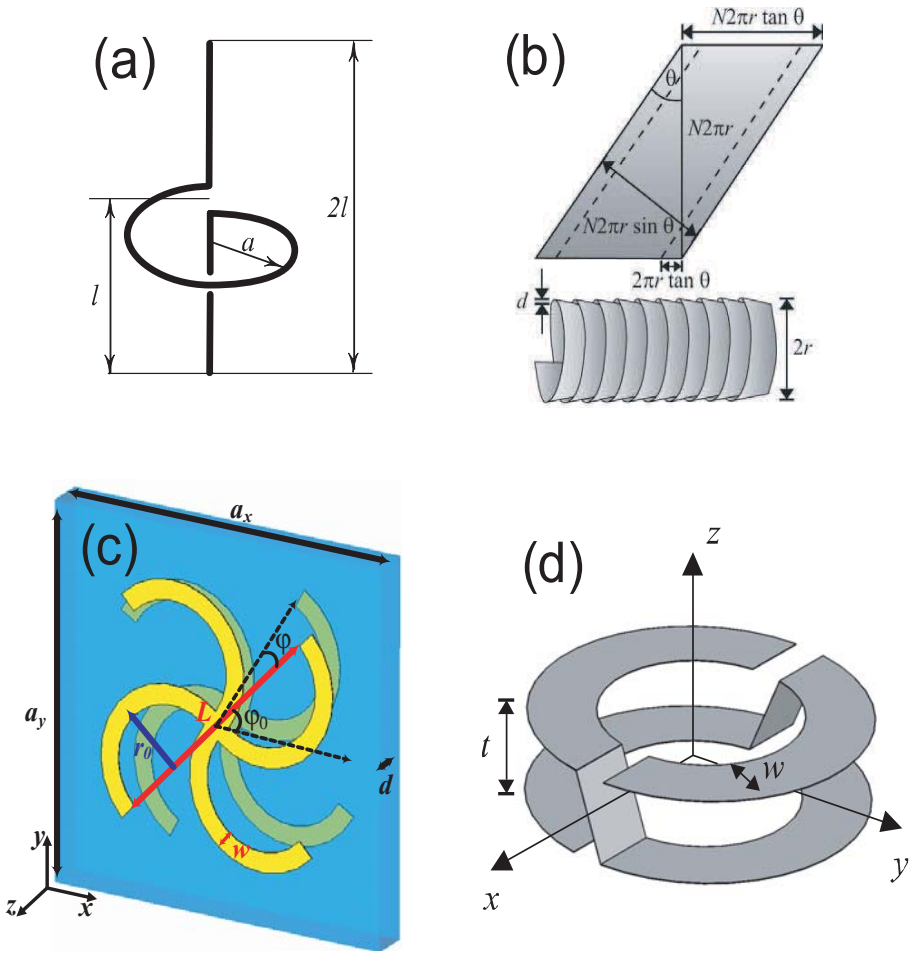

Figure 1.10 Chiral metamaterial designs. (a)Canonical helix; (b) Twisted Swiss-role metal structure; (c) Bilayer rosette structure (d) Chiral SRRs.

The chiral metamaterial can be modeled as a reciprocal bi-isotropic medium and the constitutive equation is given by

$$\begin{pmatrix} \mathbf{D} \\ \mathbf{B} \end{pmatrix} = \begin{pmatrix} \epsilon_0\epsilon & -\mathrm{i}\kappa/c_0 \\ \mathrm{i}\kappa/c_0 & \mu_0\mu \end{pmatrix} \begin{pmatrix} \mathbf{E} \\ \mathbf{H} \end{pmatrix}, \tag{1.19}$$

where ϵ_0, μ_0, and c_0 are the permittivity, permeability, and the speed of light in vacuum, respectively. Assuming $\exp(-\mathrm{i}\omega t)$ time dependent, the eigen solution of electromagnetic wave in bi-isotropic media is circular polarized plane waves, and the polarization is either left-handed

circular polarized (LCP) or right handed polarized (RCP). The refractive indices for LCP and RCP are given by [77, 78]

$$n_{\pm} = \sqrt{\epsilon\mu} \pm \kappa, \tag{1.20}$$

where $(+)$ and $(-)$ denote RCP and LCP. Both LCP and RCP have the same impedance given by $z/z_0 = \sqrt{\mu/\epsilon}$, where z_0 is the impendence of the vacuum.

From Eq. (1.20), one can immediately see that $n < 0$ for one of the polarizations if κ is large enough such that $\sqrt{\epsilon\mu} < \kappa$. It has been shown that the polarization azimuth rotation, θ, shows the rotary power is proportional to the chiral parameter, κ. Specifically, $\theta = \kappa k_0 d$, where k_0 and d are the wave vectors in a vacuum and the thickness of the bi-isotropic slab. Thus, the chiral materials with large rotary power, such as the bilayer structures and chiral SRRs, possibly possess the negative refractive index. Very recently, the negative refractive index has been confirmed experimentally by using the bilayer rosette structures [79].

1.7 Conclusions

Left-handed materials have brought significant impact to the field of physics, engineering, and material sciences. These materials can exhibit exotic phenomena that cannot be obtained with natural materials, such as perfect lensing and cloaking. Since such materials were first realized seven years ago, intense theoretical, computational, and experimental studies have been devoted to this field. Researchers from different groups made great efforts and managed to build LHM from microwave frequencies up to the optical regime. New designs, such as the short wire pairs and the fishnet, were proposed and realized. Nowadays, new topics, such as nonlinear metamaterials, active metamaterials, and chiral metamaterials, etc., have become subjects under investigation.

CHAPTER 2. ELECTROMAGNETIC PROPERTIES OF SPLIT-RING RESONATORS

The split-ring resonator (SRR) is the common constituent to provide magnetic response in metamaterials. Before we start our journey of left-handed materials, we should first study the electromagnetic properties of SRRs. Next, we will show the electric and magnetic response of SRRs of incident EM waves under different polarizations. We will discuss the retrieval procedure, which allows us to extract the effective parameters, ϵ and μ, from the transmission and the reflection coefficients. Finally, we will show the breakdown of the linear scaling property of SRRs, which will cause trouble in bringing the operating frequency of SRRs up to the optical regime. Therefore, there is a need to search for alternative designs suitable for the optical regime.

2.1 Electric and Magnetic Response of SRRs

In 1999, Pendry et al. [4] suggested a design made of two concentric metallic rings with gaps, called split ring resonators (SRRs), which exhibit a $\mu < 0$ around the magnetic resonance frequency ω_m. Immediately after, Smith et al. [5] fabricated the first negative index material at GHz frequencies. Theoretical and experimental studies [80, 37, 40] have proven that an effective SRR can be built from a single-ring design, exploiting only the capacitance across and near the gaps. This simplifies fabrication, especially for small structural sizes, and potentially reduces dielectric losses, since the fields get strong only in and around the gaps but not between the rings. Later, the U-shaped SRRs design was proposed and investigated at 200 THz [39], which has a smaller capacitance, and, therefore, is able to work at higher resonance frequency compared to the traditional SRRs design.

We systematically studied the electric and the magnetic resonance responses of single ring U-shaped SRRs for difference polarizations of incoming EM waves. The effective electric permittivity, ϵ, and the magnetic permeability, μ, will be extracted by the retrieval procedure [28, 34, 33]. In addition, the current distribution along the sides of the U-shaped SRR will be shown.

The SRR in its simplest form consists of a highly conductive metallic ring broken in one (or several) location(s) by a non-conductive gap of air or other dielectric materials. If this ring is placed in a temporally varying magnetic field, an electric circular current is induced in the metallic ring, which, in turn, leads to charge accumulation across the gaps. Due to the charge at the gap, the electric field which builds counteracts the circular current, leading to energy stored in the vicinity of the gaps and magnetic field energy concentrated in the region enclosed by the ring. Thus, the SRR is a resonator which couples to a perpendicular magnetic field and can be characterized by the effective capacitance of the gaps and effective inductance of the loop defined by the ring. It can be understood in terms of a resonant LC circuit with a resonance frequency $\omega_m^2 = 1/LC$, where L is the inductance and C is the capacitance of the SRR. The resonant response of the circular current in the SRR to an external magnetic field leads to a resonant magnetic moment, which may reach large negative values for an array of SRRs. If the size of the SRR is much smaller than the wavelength of an incident electromagnetic wave around the resonance frequency, the SRR array behaves as a homogeneous effective medium with negative (resonant) permeability $\mu_{\text{eff}}(\omega)$.

2.1.1 EM response of SRRs in three polarizations

Our numerical simulations are completed with CST Microwave Studio$^{\text{TM}}$ (Computer Simulation Technology GmbH, Darmstadt, Germany), which uses a finite-integration technique, and Comsol Multiphysics$^{\text{TM}}$, which uses a frequency domain finite element method. The schematic of the periodic U-shaped SRRs arrays and the geometry of a single unit cell used in our numerical simulations are shown in Fig. 2.1(a) and (b), respectively. The SRRs exhibit different responses to the incident electromagnetic (EM) wave with respect to different config-

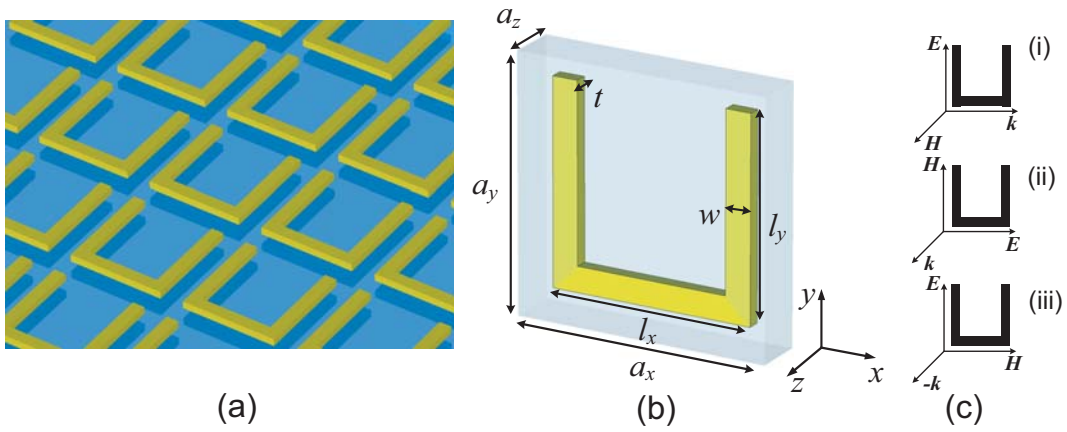

Figure 2.1 (a) Schematic of periodically arranged U-shaped SRR arrays; (b) A single unit cell with geometrical parameters; (c) three different configurations of incident electric field, **E**, magnetic field, **H**, and wave vector, **k**.

urations of the incident electric field, **E**, magnetic field, **H**, and wave vector, k, as shown in Fig. 2.1(c). First, it is well know that the incident EM wave excites a magnetic resonance at ω_m [4, 81, 82, 83, 84, 1], if the external magnetic field, **H**, is perpendicular to the SRR plane and the wave vector, **k**, is parallel to the SRR plane (Fig. 2.1(c.i)). Second, further study reveals that the incident EM wave with **k** perpendicular to the SRR plane and **E** parallel to the bottom part of SRR (Fig. 2.1(c.ii)) also excite a magnetic resonance at ω_m [40]. This magnetic resonance results from a circular current induced by the external electric field, **E**, because of the asymmetry of the SRR in the direction of **E**, and, therefore, was called the electric excitation coupling to the magnetic resonance (EEMR). The EEMR is very valuable for the experimental demonstration of the magnetic resonance at optical frequencies, because it is very difficult to measure the transmission and reflection with the incident EM wave parallel to the SRR plane at high frequencies [36, 38, 39, 37, 40]. Third, the SRRs also exhibit a short-wire-like electric resonance [27] at ω_0 with the incident electric field, **E**, parallel to the side part of SRRs (Fig. 2.1(c.iii)). The electric resonance frequency ω_0 depends on the length of the side part of SRRs, l_y, being higher for shorter l_y.

The transmission spectra for these three cases are shown in Fig. 2.2. All these responses result in dips in the transmission, which indicate a resonance at the corresponding frequencies.

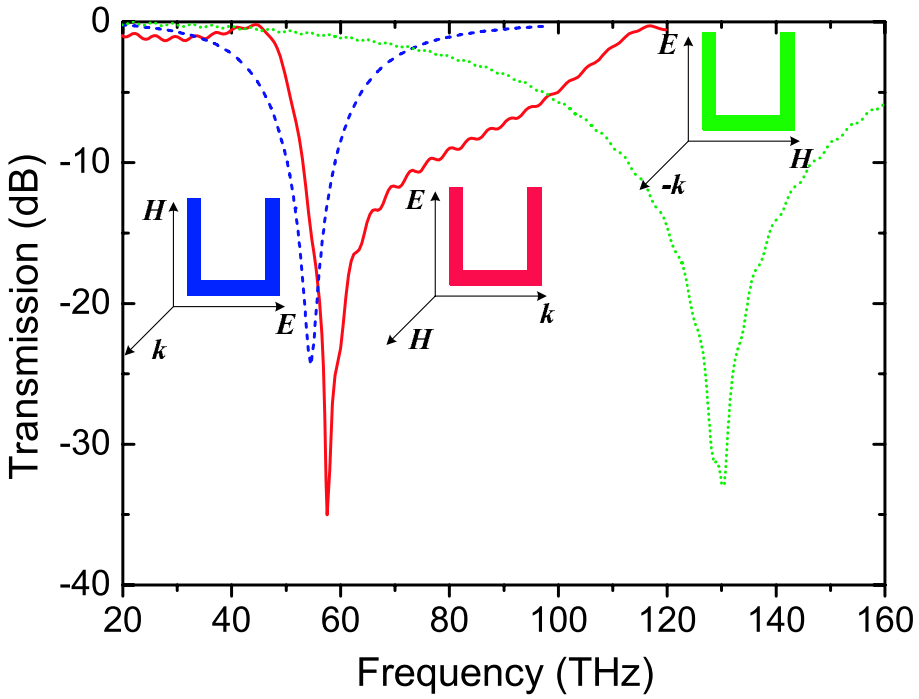

Figure 2.2 Transmission spectra for the magnetic resonance (red solid), the electric excitation coupling to the magnetic resonance (EEMR) (blue dashed) and the short-wire-like resonance (green dotted) of USRRs. The geometric parameters are $a_x = a_y = 1$ μm, $a_z = 0.2$ μm, $l_x = l_y = 0.8$ μm, $w = 0.1$ μm and $t = 0.05$ μm.

One can see that the magnetic resonance and the EEMR occur roughly at the same frequency, $f_m \approx$55 THz, while the short-wire-like electric resonance happens at a much higher frequency, $f_e \approx$130 THz.

Using the retrieval procedure [28, 34, 33], we calculated the effective permittivity $\epsilon(\omega)$ and permeability $\mu(\omega)$, both the real and the imaginary part, from the simulated transmission, T, and reflection, R. Figure 2.3 shows the extracted real part of the effective permittivity $\mathrm{Re}(\epsilon(\omega))$ and permeability $\mathrm{Re}(\mu(\omega))$ for three different polarized incident EM waves as shown in Fig. 2.1(c). As expected, the magnetic resonance, measured by μ (red solid), occurs around $\omega_m = 55$ THz. The EEMR gives a similar resonance for ϵ (blue dashed) at roughly the same frequency, which indicates the response is due to the electric coupling of the incident EM wave to SRR. At a higher frequency, $\omega_0 = 135$ THz, the short-wire-like electric resonance of the SRR occurs, given by the resonance behavior of ϵ (green dotted). Due to the periodicity effect,

whenever a magnetic resonance occurs in Re(μ), an electric anti-resonance will be seen in Re(ϵ) simultaneously and vice versa [33, 32]. The periodicity effect becomes more noticeable as the

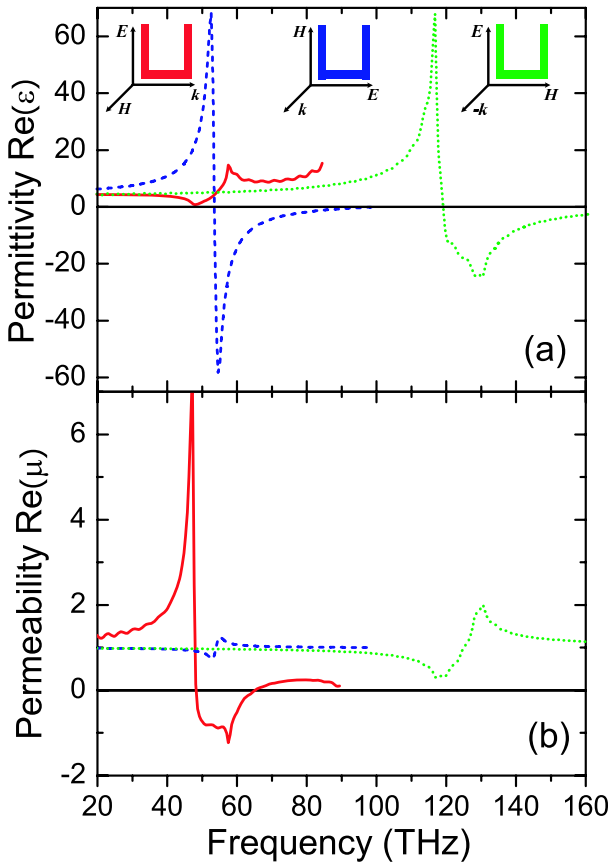

Figure 2.3 Extracted effective permittivity Re($\epsilon(\omega)$) (a) and effective permeability Re($\mu(\omega)$) (b) for the magnetic resonance (red solid), the electric excitation coupling to the magnetic resonance (EEMR) (blue dashed) and the short-wire-like resonance (green dotted) of USRRs. The geometric parameters are $a_x = a_y = 1$ μm, $a_z = 0.2$ μm, $l_x = l_y = 0.8$ μm, $w = 0.1$ μm and $t = 0.05$ μm.

wavelength of the EM wave is comparable with the lattice constant of the SRR lattice. For the magnetic resonance (red solid), the lattice constant, $a_x = 1$ μm, in the propagating direction along the wave vector, $\mathbf{k}$, is comparable to the resonance wavelength, $\lambda_m = 5.45$ μm; hence, a strong distortion in the negative part of resonance in Re(μ) and a significant anti-resonance in Re(ϵ) can be observed. On the other hand, for the EEMR, the lattice constant, $a_x = 0.2$ μm, is much smaller than λ_m, so the periodicity effect is much weaker and, therefore, a sharp resonance in Re(ϵ) (blue dashed) with a weak anti-resonance in Re(μ) occurs.

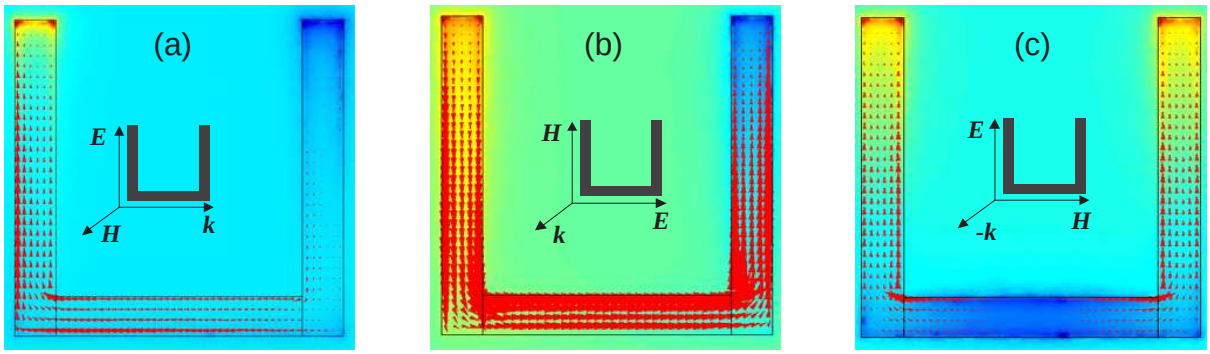

Figure 2.4 Distribution of the perpendicular component of the surface electric field (color scale; red positive, blue negative) and the bulk current density (arrows) for the three resonance coupling of the SRR. The SRR metal is described by a Drude model for gold ($f_p = 2175$ THz, $f_\tau = 6.5$ THz), the geometry parameters are: $a_x = a_y = 1$ μm, $a_z = 200$ nm (unit cell size), $l_x = l_y = 800$ nm (arm length), $w = 100$ nm, $t = 50$ nm (ring width and thickness, respectively). The current distributions are shown temporally $\pi/2$ phase shifted against the charge distribution.

2.1.2 Current modes of SRRs

Figure 2.4 shows the distribution of the current and the charge density for the three resonant modes of a U-shaped SRR. The current density is obtained directly from the simulation results, and the charge density is related to the perpendicular electric field at the surface of the metal. All fields are time harmonic; the current distributions are shown temporally $\pi/2$ phase shifted against the charge distribution. Figure 2.4(a) shows the magnetic resonance for parallel incidence to the SRR with the magnetic field coupling to the SRR, which induces a circular current with charges of the opposite sign accumulating at the ends of the side arms of the SRR. Since the magnetic field is perpendicular to the SRR plane, we expect a symmetric current with respect to the center axis of the SRR along the y-direction. However, one can see that the current density in the two side arms is not symmetric. This is due to the fact that the incident electric filed polarizes two side arms of the SRR and results in linear currents. The total current shown in Fig. 2.4(a) is the superposition of the circular current induced by the magnetic field and the linear current caused by the electric filed and, therefore, shows asymmetry. The circular current generates a magnetic moment. Figure 2.4(b) shows the EEMR

resonance for normal incidence to the SRR with the electric field breaking the symmetry of the SRR and, thus, we have coupling to the "magnetic" resonance [40]. The surface electric field distribution is qualitatively equivalent to the pure magnetic coupling in Fig. 2.4(a), which case is hard to realize experimentally at high THz frequencies. Unlike the magnetic resonance, only circular current is excited by the electric field in the EEMR, so the current distribution shows very good symmetry. The electric excitation of EEMR occurs via the polarization of the bottom arm of the SRR (by the electric field of the incident EM wave). Similar as the magnetic resonance, the EEMR also lead to a magnetic moment coming from the circular currents flowing along the three arms.

For the other polarization shown in Fig. 2.4(c), (normal incidence to the SRR with the electric field along the symmetry axis of the SRR), we see a short-wire-like resonance. The current distribution has a mirror symmetry with respect to the center axis of the SRR along the y-direction, and thus cannot have a magnetic moment. However, the short-wire-like resonance does possess an electric dipole moment in the **E**-direction, i.e., along the two parallel arms of the SRR, and represents a purely electric response of the SRR.

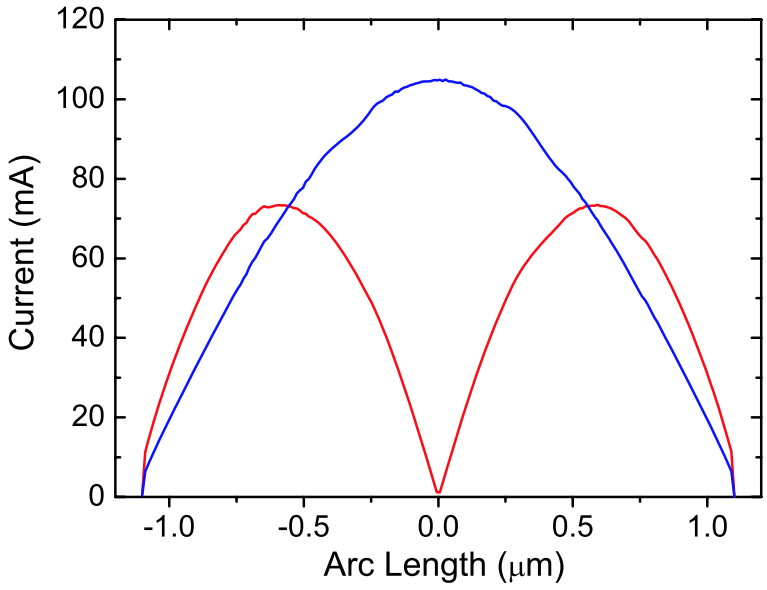

Figure 2.5 Current distribution for the EEMR response (blue) and the short-wire-like response (red).

Figure 2.5 shows the distribution of the total current (current density, **J**, integrated over

the cross-section of the SRR ring) over the arc length around the SRR ring for the EEMR and the short-wire-pair-like resonance, respectively. We clearly see the magnetic resonance has a $\lambda/2$ current mode over the whole length of the SRR, while the short-wire-like resonance has a full λ current mode.

2.1.3 Electric and magnetic moments of SRRs

We also studied the electric moment and the magnetic moment for the electric excitation of the magnetic resonance (EEMR) and the short-wire-like resonance of the U-shaped SRRs with different length of two parallel side arms, l_y. The electric moment is calculated by the integration of the difference between the electric displacement, $\mathbf{D}$, and vacuum electric displacement, $\epsilon_0\mathbf{E}$, over the volume of the whole unit cell.

$$\mathbf{p} = \int (\mathbf{D} - \epsilon_0\mathbf{E})\mathrm{d}r^3,$$

Then the electric polarization, normalized by incident electric field, $\mathbf{E_0}$, $\mathbf{P} = \mathbf{p}/(VE_0)$ is shown in Figs. 2.6(a) and 2.6(b) for the EEMR and the short-wire-like response of the SRRs, respectively. It is clearly seen that the electric resonances generate strong electric moments. In Fig. 2.6(a), the electric polarization, P_x, decreases as the length of two parallel arms, l_y, decreases, because the EEMR response becomes weaker and finally disappeared as the length, l_y, close to zero (green dotted curve). However, the electric polarization, P_x, does not vanish in the limiting case of $l_y = 0$, (green dotted curve), because the EEMR degenerates to the short-wire-like electric resonance of the bottom arm of the SRR, which results in the non-zero electric polarization. The polarization density along the y-direction, P_y, of the short-wire-like resonance of the SRR (Fig. 2.6(b)) with the incident electric field $\vec{E}$ parallel to the side arms of the SRR, also decreases and shifts to higher frequencies as l_y decreases.

The magnetic moment is calculated by employing the formula:

$$\mathbf{m} = \frac{-\mathrm{i}\omega}{2} \int \vec{r} \times (\mathbf{D} - \epsilon_0\mathbf{E})\mathrm{d}r^3.$$

In Fig. 2.7(a), we show the magnetic moment, normalized by the magnetic field of the incident EM wave, $\mathbf{H_0}$, $\vec{M}_z = \vec{m}_z/(VH_0)$, and in Fig. 2.7(b), the extracted permittivity, $\mathrm{Re}(\epsilon)$,

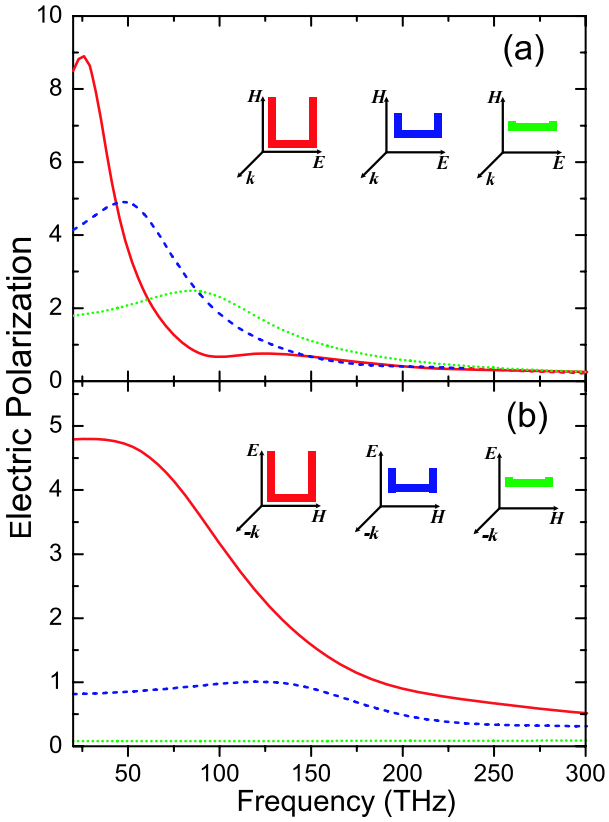

Figure 2.6 Magnitude of the normalized polarization density, P, of the U-shaped SRRs with $l_y = 0.8$ μm (red solid), 0.4 μm (blue dashed) and 0.11 μm (green dotted), respectively. (a) P_x component as **E** parallel to the bottom part of SRRs. The other two components P_y and P_z are nearly zero; (b) P_y component as **E** is parallel to the side part of SRRs. The other two components P_x and P_z are nearly zero. The polarizations of the incident EM wave are shown as the insets in the panels (a) and (b).

for the magnetic resonant modes of the SRR as a function of frequency for three different U-shaped SRRs with different lengths of the two parallel arms, l_y. It is clearly seen that the magnetic resonance provides a strong magnetic moment at frequency ω_m, but the magnetic moment is non-zero at frequency above ω_m, due to the contribution of higher order excitations. As one expects, reducing the length of the parallel arms reduces the magnetic moment. It also shifts the magnetic resonance to higher frequencies. This is a combined effect of the shortened arc length and reduced the geometric loop inductance. In the limit of only the bottom arm left (i.e. a straight rod) the magnetic response vanishes (green dotted curve), and no magnetic

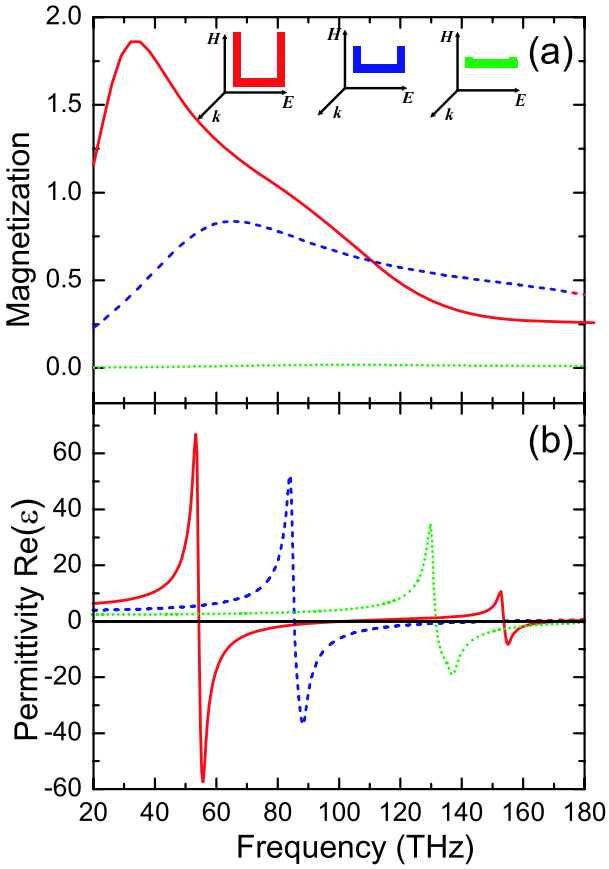

Figure 2.7 (a) Magnitude of the normalized magnetization, M_z, and (b) the extracted permittivity, Re(ϵ), of the U-shaped SRRs with the length $l_y = 0.8$ μm (red solid), 0.4 μm (blue dashed) and 0.11 μm (green dotted), respectively. The polarizations of the incident EM wave are shown as the insets in the panel (a). The short-wire-like resonance with incident EM wave polarized as shown in Fig. 2.1(c.ii) has zero magnetic moment, and, therefore, is not shown here.

response is seen. In this limiting case, the resonance in Re(ϵ) still exists, a result of the electric resonance of the bottom arm of SRR. Note, the magnitude of the resonance in Re(ϵ) decreases much slower than the magnetic moment does as the arm length, l_y, decreases. The reason is the magnetic moment, m_z, resulting from the circular current flowing in the loops of the SRR, vanishes immediately as the side arms disappear, but the resonance in Re(ϵ) always exist as long as the short-wire-like electric resonance exists, shown in Fig. 2.4(c) in the bottom part of the SRR. However, as shown in the green curve of Fig. 2.7(a), this short-wire-like electric resonance cannot provide any magnetic moment.

The short-wire-like resonance with the propagating direction of the incident EM wave perpendicular to the SRR plane and the electric field, **E**, parallel to the side arms of the SRR (Fig. 2.1(c.ii)), has no magnetic moment.

2.2 Retrieval procedure

Smith et al. proposed a retrieval procedure [28] to obtain the effective electromagnetic parameters of LHM, i.e., the effective permittivity, ϵ and the effective permeability. The idea was to model the metamaterial as an *isotropic homogeneous* slab, and to calculate the effective parameters, ϵ, and μ of the homogenous slab, from the measured or simulated metamaterial transmission, T, and the reflection, R, by using the theoretical formulas for the slab. For an isotropic homogeneous slab in a vacuum space, the transmission, t, and reflection, r, have the following relation with the refractive index, n, and the impedance, z, of the slab,

$$t^{-1} = \cos(nkd) - \frac{\mathrm{i}}{2}\left(z + \frac{1}{z}\right)\sin(nkd) \tag{2.1}$$

$$\frac{r}{t} = -\frac{\mathrm{i}}{2}\left(z - \frac{1}{z}\right)\sin(nkd), \tag{2.2}$$

where k and d are the wave vector in vacuum and the thickness of the slab, respectively. Eqs. (2.1) and (2.2) can be inverted to calculate n and z from t and r. By completing this inversion, we obtain,

$$z = \pm\sqrt{\frac{(1+r)^2 - t^2}{(1-r)^2 - t^2}} \tag{2.3}$$

$$\cos(nkd) = \frac{1}{2t}\left(1 + t^2 - r^2\right)., \tag{2.4}$$

Although Eqs. (2.3) and (2.4) have a relatively simple form, both are complex functions with multiple branches, which lead to ambiguities to determine the final expression of ϵ and μ. We need additional information about material properties to fix these ambiguities. Normally, the materials are passive, so the real part of the impedance $Re(z) > 0$, which fixes the sign in Eq. (2.3). Similarly, the requirement for the imaginary part of the refractive index, $Im(n) < 0$, for the passive material, fixes the sign of n:

$$\mathrm{Im}(n) = \pm\mathrm{Im}\left(\frac{\cos^{-1}\left(\frac{1}{2t}\left(1 + t^2 - r^2\right)\right)}{kd}\right). \tag{2.5}$$

It is worth noting that, from Eq. (2.2), one can see that the sign of z and n are correlated, i.e., the same sign must be chosen in Eqs. (2.3) and (2.5). Once the sign of $\mathrm{Im}(n)$ is chosen, the sign of $\mathrm{Re}(n)$ is unambiguously decided.

Thus, we have resolved ambiguities caused by the sign of n and z. However, since the cosine function has multiple branches, we still have ambiguity in the real part of n, which is given by

$$\mathrm{Re}(n) = \pm \mathrm{Re}\left(\frac{\cos^{-1}\left(\frac{1}{2t}\left(1+t^2-r^2\right)\right)}{kd} \right) + \frac{2\pi m}{kd}, \tag{2.6}$$

where m is an integer. Eq. (2.6) shows the branches can be very close to each other when d is large, which makes the selection of the correct branch difficult in the case of dispersive medium. So we should take the smallest possible thickness sample in the simulation or experiment. Even in the case of a small thickness sample, it can be very difficult to choose the correct branch from the frequencies close to the resonance, where n changes rapidly. A common way to choose the correct branch is to start with a frequency far below the resonance, where n is close to 1, and calculate n successively by assuming the continuity of n as the frequency increases.

The effective permittivity, ϵ, and the permeability, μ, can be obtained by $\epsilon = n/z$ and $\mu = nz$.

The retrieval procedure described above is under the assumption that the metamaterial can be viewed as a homogenous medium. In this case, the internal structure inside the unit cell of the metamaterial must be symmetric along the propagating direction of the EM wave. If the structure does not have this symmetry, e.g., the sample is prepared on a substrate, the reflections, r_{12} and r_{21}, from both side of the slab are no longer identical. Therefore, the homogenous retrieval procedure is not valid. However, it has been proven that one can use the same equations to handle the asymmetric structures by taking the average reflection, $r = \sqrt{r_{12}r_{21}}$ [34].

2.3 Frequency saturation of the magnetic resonance of a SRR in the optical regime

As we have mentioned in Chapter 1, there is a sustained effort in the community to push the operating frequency of the metamaterials deeper and deeper into the THz region to reach ultimately optical frequencies. This is so important because there are no natural materials that would still have magnetic properties at such high frequencies. At low frequency regimes, up to several THz, the magnetic resonance frequency scales reciprocally with the structural size. At high frequencies, however, this linear scaling breaks down as we show later in this section. The resonance frequency saturate as geometric size decreases down to a certain limit, which makes it more difficult to push the working frequency of LHM even higher. Our studies show that the breakdown of this linear scaling properties is due to the kinetic energy of electrons.

2.3.1 Effective inductance due to kinetic energy of electrons

Although in principle the dielectric materials could also show an explicit frequency dependence of their material parameters, it is the metal that first limits the operation of the SRRs. At high frequencies the kinetic energy of the electrons in the metal (both in the SRRs and the wires) cannot be neglected anymore in comparison with the magnetic energy. Indeed the kinetic energy of the electrons in the SRR adds a term to the magnetic energy which can be written as $L_e I^2/2$, where the electron self-inductance L_e is given by

$$L_e = \frac{l'}{S'\omega_p \epsilon_0} \tag{2.7}$$

where $l' = 4(l-w) - d$ is the length of the axis of the wire making the ring (see Fig. 2.8). S' is the effective cross-section of the ring, smaller than $S = wt$ (because of the skin depth and the asymmetry of the current distribution between the center and the external sides of the ring), and ω_p is the plasma frequency of the material. The geometrical dimensions are defined in Fig. 2.8; the gap-size is $d = 0.2L$.

The formula of L_e shown in equation 2.7 can be derived in a straightforward way by taking into account that the electronic kinetic energy, $L_e I^2/2$, is $N_e m_e v_e/2$, where $v_e = j_e/(en_e)$,

$I = \int j_e \mathrm{d}s = S' j e$, v_e is the average electron velocity, j_e the current density, n_e the free electron concentration, $N_e = l' S' n_e$ is the total number of electrons participating in the current, and $S' = \gamma S$ with $\gamma < 1$. Notice that L_e scales as $1/a$, where a is the unit cell size. In contrast to the magnetic field inductance, L_m, which scales as a (since all the geometric parameters scale proportional to a).

The capacitance, C, of the split ring scales also proportional to a, so that the resonance frequency, f_m, of the SRR has the following a dependence

$$f_m = \frac{1}{2\pi} \frac{1}{\sqrt{(L_m + L_e)C}} = \frac{1}{2\pi} \frac{1}{\sqrt{(c_1 a^2 + c_2)}} \tag{2.8}$$

where c_1 and c_2 are independent of the length L in the framework of the LC circuit model. For smaller structural size also surface scattering effects become dominant that also break the scaling and increase the ohmic losses. Taking everything together, as we push the magnetic resonance frequency higher by reducing the structural size of the SRR, we expect to see a breakdown of the linear scaling together with a diminishing strength of the SRR resonance that ultimately renders the SRR dysfunctional.

2.3.2 Numerical studies of the magnetic resonance of SRRs in the optical regime

Via numerical simulations, we investigate how high we can push the magnetic resonance frequency of a realistic SRR design made from aluminum. As shown in Fig. 2.8 we have considered single ring SRRs as well as multi-gap SRRs. The SRR is made of aluminum, simulated by using a Drude-model permittivity (f_p =3570 THz, f_{tau} =19.4 THz), separated from the $0.343a$ thick substrate (glass, ϵ =2.14). Keeping in mind the need for higher dimensional isotropic metamaterials the unit cell has to be symmetric. Hence, a symmetric SRR design [85] is required, as the 4-gap one. This, as the 2-gap one, avoids the undesirable excitation of the magnetic resonance by the electric field [40, 86].

We simulate single-ring SRR-only metamaterial designs, using the commercial CST Microwave Studio. The metamaterial is defined as a periodic repetition of a single rectangular unit cell containing a single SRR as shown in Fig. 2.8. The gap size has been reduced according to the number of cuts, expecting to approximately preserve the total capacitance, C, and

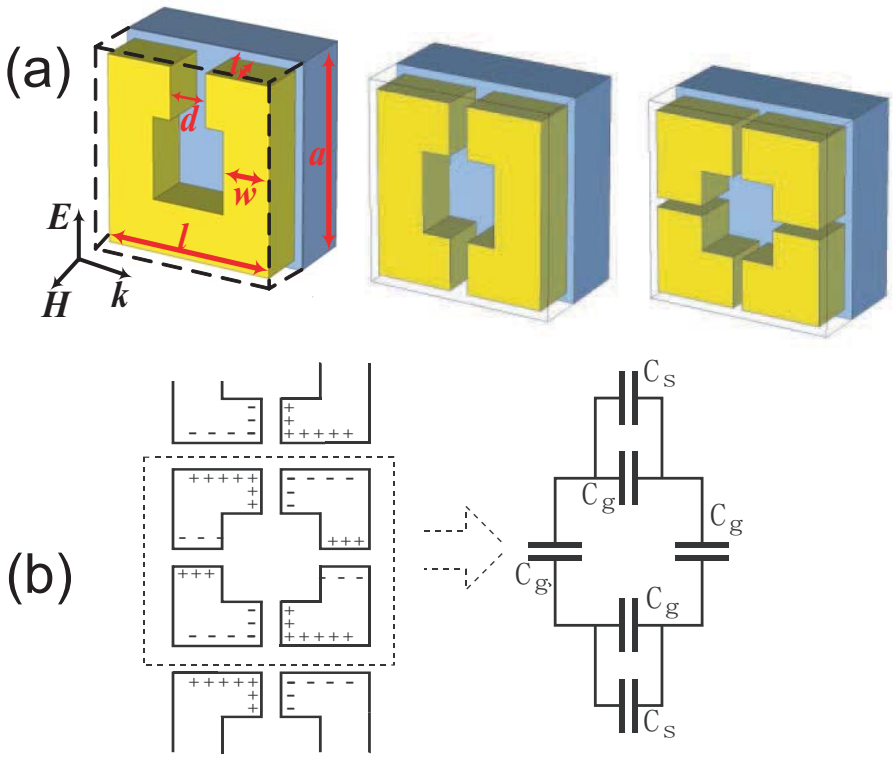

Figure 2.8 (a): The geometries of the 1, 2 and 4-gap single-ring SRR are shown; the unit cell has the dimensions $a \times a$ in the SRR plane and $0.614a$ perpendicular to it. The parameters of the SRR are: side length $l = 0.914a$, width and thickness $w = t = 0.257a$ and gap-width 0.2a, 0.1a and 0.05a for the 1, 2 and 4-gap SRR, respectively. (b) The left panel shows the charge accumulation in a 4-cut SRR, as a result of the periodic boundary conditions in the **E** (and **H**) direction. The right panel shows the equivalent LC circuit describing this SRR. C_g is the gap capacitance and C_s the side capacitance resulting from the interaction with the neighboring SRR.

the total inductance, L_m, of the effective LC circuit constituted by the SRR (assuming that $C \sim wt/d$, and $L_m \sim l'$). The direction of propagation and the electric field are parallel to the SRR plane. The orientation of the SRR is such that mirror symmetry with respect to the electric field vector is preserved, thus only the magnetic field couples to the resonance of the circular currents in the SRR ring.

In Fig. 2.9 we show the results of our simulation for f_m, together with the outcome of the LC circuit model given in equation 2.8. It is worthwhile to point out that the simple formula 2.8 with realistic values of c_1 and c_2 reproduces the simulation well, especially for the 4- and

the 1-gap cases; the saturation value of the 2-gap case is lower than the simulation value by 19%; this discrepancy is attributed to a breakdown of the homogeneous effective medium (see below). On the basis of the simple formulae $C \sim wt/d$, and $L_m \sim l'$, it is expected that the three simulation curves ought to more or less coincide, since l' is the same for the 1-, 2-, 4-cut case and $C_2 = C_4 = C$, since $C_2 = Cd/(2d_2)$, $C_4 = Cd/(4d_4)$and $d_2 = d/2$ and $d_4 = d/4$ (the subscript in capacitance and cut-width refers to the 2- and 4-gap case). However, as is shown in Fig. 2.9, the ratio of the f_m in the linear regime is $f_{m2}/f_{m1} = 1.39$, $f_{m4}/f_{m1} = 2.1$, which implies, assuming $L_{m4} \approx L_{m2} \approx L_{m1}$, that $C_1/C_4 = 4.4$ and $C_1/C_2 = 1.93$. There are two physical reasons why those ratios are so different from one. First, the formula $C \sim wt/d$ is not valid because d is not much smaller than w. Numerical electrostatic calculation of the capacitance by employing the method of moment, (approximately including the presence of the dielectric substrate) at each cut gives $C_g^1 = 10.5a$ pF, $C_g^2 = 12.7a$ pF, and $C_g^4 = 18a$ pF (a in meters) where the superscript refers to the 1-, 2-, 4-cut case, respectively. Second, because of the periodic boundary conditions along the direction of the electric field only (in the simulations there is only one unit cell along the $\mathbf{k}$ direction) there is a charge accumulation to the sides of the cuts as shown in Fig. 2.8(b) for the 4-cut case. This adds a side capacitance, C_s^n , n =1,2,4, which was found numerically to be (including an estimated increase due to the dielectric substrate) $C_s^1 = 13.109a$ pF, $C_s^2 = 18.81a$ pF, and $C_s^4 = 20.22a$ pF. Combining these electrostatically calculated capacitances we found $C_1 = 23.609a$ pF, $C_2 = 15.755a$, $C_4 = 6.118a$. The ratio of the electrostatically calculated capacitances, and $C_1/C_4 = 3.86$ and $C_1/C_2 = 1.50$ turn out to be lower than but not far from the ones inferred from the simulations. The difference can be attributed to retardation effects present in the simulation but absent in the LC circuit modeling.

We calculated also the inductance, $L_m = L_m^{\text{out}} + L_m^{\text{in}}$, by employing the formulae given in Ref. [7], $L_m^{\text{out}} = (\mu l'/2\pi)[\log(8r/b) - 1.75]$ (inductance of a circular ring of radius r, with a circular cross-section of radius b), where $r = l'/2\pi$, $\pi b^2 = wt$ and $l' = 4(l - w) - d$, for the inductance outside the metal, and $L_m^{\text{in}} = (\mu_0 l'/8\pi)$ for the internal inductance in the metal. The final result is $L_m = 0.76a$ μH ($a$in meters). In obtaining these values we have ignored the

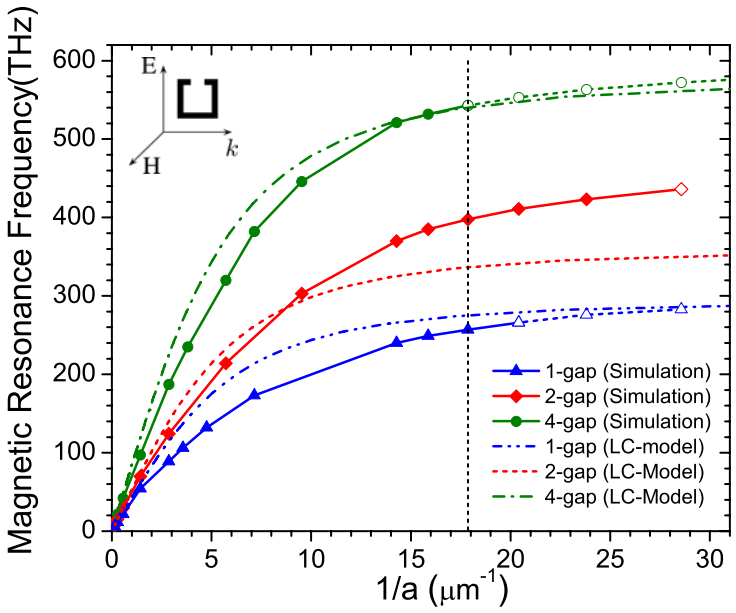

Figure 2.9 The scaling of the magnetic resonance frequency f_m as a function of the linear size a of the unit cell is shown for the 1-, 2-and 4-cut SRR. Up to the lower terahertz region the scaling is linear, $f_m \propto 1/a$. The maximum attainable frequency is strongly enhanced with the number of cuts in the SRR ring. The hollow symbols as well as the vertical line at $1/a = 17.9\mu m^{-1}$ indicate that no $\mu < 0$ is reached anymore. The broken lines shows The scaling of f_m vs a calculated through equation 2.8 (LC circuit model) for the 1-, 2-and 4-gap SRR.

mutual inductance due to the periodicity along the **H** direction (see Fig. 2.8), because of the rather large separation ($0.614a$); on the other hand we corrected the above values taking into account that the periodic boundary conditions (along the direction of the electric field) imply mutual inductances which reduce the value of L_m by a factor estimated to be 0.75. Thus, $L'_m = 0.75L_m = 0.57a$ μH (a in m meters).

Using the formula for L_e derived before (with $\gamma = 2/3$) and the total capacitance values, we find the c_2 of equation 2.8; for the 1-gap case, $c_2 = 0.29 \times 10^{-30}$, using our numerical results, equation 2.8 is reduced to

$$f_m^n = \frac{159 \text{ THz}}{\sqrt{c'_n}\sqrt{(6.43a^2 + 0.14)}}, \qquad n = 1, 2, 4. \tag{2.9}$$

where a is in μm, and c'_n=2.08, c'_n=1.39, c'_n=0.54.

2.3.3 Disappearance of negative μ at high frequency

We expect the magnetic resonance to become broader and weaker for each of the three cases studied here as the size becomes smaller and the resonance frequency increases; this is due to the losses that are increasing linearly with the resonance frequency. Furthermore, the permittivity of the metal, described in our simulations through the Drude model formula, becomes smaller as the frequency increases, and hence the contrast to vacuum decreases, while ohmic losses are increasing leading to a weaker resonance of the SRR. The permittivity of the dielectrics is still considered frequency independent in our simulations, using its typical values in the THz regime.

The transition to purely positive $Re\left((\mu(\omega))\right)$ is indicated by the change from full to hollow symbols in Fig. 2.9. Interestingly this transition occurs pretty consistently for all SRR designs for a specific size around 50 nm rather than for a specific frequency. This behavior can be deduced from the LC circuit analysis. Indeed, one can obtain a rough estimate of the permeability $\mu = \mu_0(1+\chi)$, where χ is the magnetic susceptibility. Using the well known formulae $\chi = M/H = m/VH$,$m = IA$, $I = E/Z$, $E = -d\phi/dt = \mathrm{i}\omega HA$, where M is the magnetization, m the magnetic moment of the unit cell of volume V, $H = B/\mu$, B is the magnetic field, I is the current. $A = l'^2$ is the area of the loop, Φ is the magnetic flux through the loop, Z is the impedance, $Z = R + iLt\omega[1-(\omega_m/\omega)^2]$, $R = l'/S'$, $\rho = 1/\sigma$, where $\sigma = -i\omega(\epsilon - \epsilon_0)$ is the AC conductivity given by the Drude formula. The final result is of the form $\chi = \Lambda/(1-\Lambda)$, where Λ for $\omega \approx \omega_m$ and $\omega \gg \omega_m$ turns out to be independent of ω_m and proportional to length square. On the other hand, the LC circuit model gives χ always less than unity, which means μ_{eff} positive, in disagreement with the $|\chi|$ simulations and the experiment.

In Fig. 2.10 we show the disappearance of the μ_{eff} region in the magnetic response with decreasing structure size for all SRR designs. The effective permeability $\mu(\omega)$ has been obtained by employing the retrieval procedure from the simulated scattering data. Qualitatively, as we pointed out before, with decreasing size of the unit cell, ω_m moves to higher frequencies but slower than it would be expected form the linear scaling. Simultaneously, the strength of the resonance, hence the amplitude of the resonant μ_{eff} , decreases. Starting from $\mu_{\mathrm{eff}} \approx 1$ far

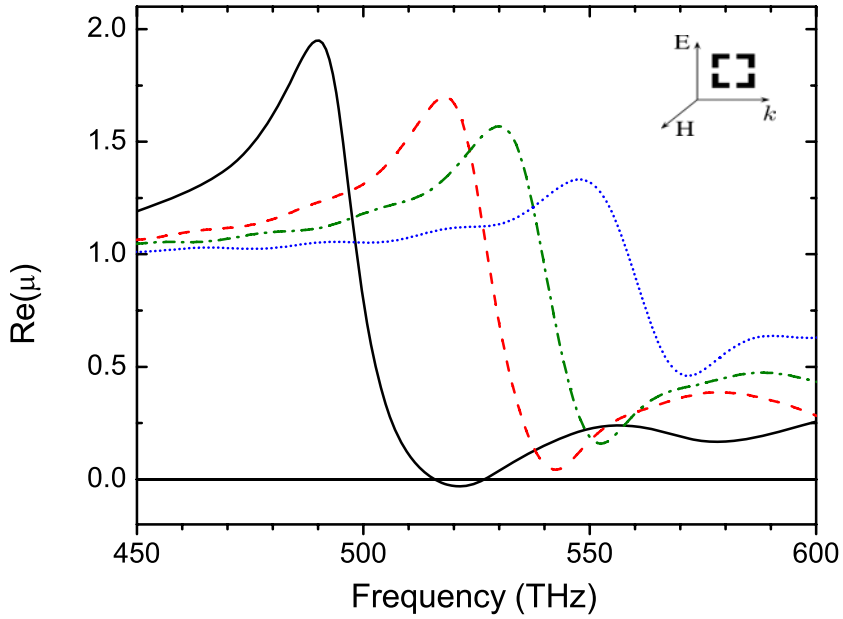

Figure 2.10 Simulation of the dependence of the shape and amplitude of the magnetic resonance in $Re\left((\mu(\omega))\right)$ of the 4-gap SRR for unit cell size a = 70, 56, 49 and 35 nm (left to right)

from ω_m,a weak resonant μ_{eff} can not reach negative values anymore, although the presence of the magnetic resonance can be confirmed up to very small unit cells. However, even in those cases, uninteresting for constructing left-handed metamaterials, the resonance frequency does not significantly increase. It must be stressed that the 4-cut design retains the negative $Re\left((\mu(\omega))\right)$ region for higher frequencies (up to about 550 THz) than the 2-cut design (up to 420 THz) and the 1-cut case (up to 280 THz). The explanation for this superior performance of the 4-cut case can be inferred from the dependence of the disappearance of the negative μ regime mainly on the length scale and the fact that more cuts produce higher frequency for the same length scale. The 2-cut case needs further discussion. For a given structural size the resonance frequency ω_m increases with the number of cuts, which brings the resonant refractive index, n_{eff}, closer in frequency to the edge of the Brillouin zone, $n_{\text{BZ}} = \pi c/\omega a$, promoting periodicity artifacts. In contrast, two effects counteract the periodicity: Generally the breakdown of the linear scaling limits the increase of ω_m while the edge of the Brillouin

zone continues to scale geometrically leading to reduced periodicity artifacts deeper in the saturation regime, i.e. for smaller structural size. Second, the increasing losses at higher frequency reduce the amplitude of the magnetic resonance and increase the separation of the resonant n_{eff} from the n_{BZ} in vertical direction (i.e. in magnitude) despite a larger $\lambda_{\text{vacuum}}/a$ ratio. Consequently, we see very weak periodicity artifact for the single-cut SRR, becoming strong for the 2-cut SRR, but decreasing again for the 4-cut SRR. The periodicity leads to a deformation of the μ_{eff} resonance, as has been discussed in great detail in Ref. [33], which saturates and widens the $\mu_{\text{eff}} < 0$ region.

We stress the fact that the 4-cut single ring SRR design is favorable for more-dimensional metamaterials not only for its highest attainable magnetic resonance frequency but also for its inherent symmetry, without bi-anisotropy or electric coupling to the magnetic resonance. For the 2-gap design, the role of elongating the two non-gap sides is worthwhile to explored, since this way one may induce a negative ϵ response as well.

2.4 Conclusions

We discussed three resonances, namely the magnetic resonance, the electric excitation coupling to the magnetic resonance (EEMR), and the short-wire-like resonance, of SRRs with respect to different polarization of the EM wave. It was shown that both the magnetic resonance and the EEMR were excited by the loop current, while the short-wire-like resonance was excited by the linear current. The magnetic resonance of SRRs at optics frequencies was studied via numerical simulations. We found the linear scaling properties of the magnetic resonance breakdown for frequencies above 100THz. The underlying reason is the free electron kinetic energy is not negligible at such high frequencies. Because the breakdown of the linear scaling properties, it is more difficulty to push the resonance frequency into the optical regime. Therefore, there is a need to search for new designs suitable for the optical regime.

CHAPTER 3. THE SHORT WIRE PAIR DESIGN

The idea of the cut-wire pair structure stems from the study of multiple gap SRRs, when we search for suitable LHM designs working at infrared or even the optical regime. To design an LHM at the optical regime, we face two serious technical difficulties. First, due to the break-down of the linear scaling property in the optical regime, the magnetic resonance frequency increases much slower as the size reduces than at microwave frequencies. Consequently, an extremely small geometry size, typically on the order of $\sim$ 10nm, is required for the multiple gap SRRs, which is far beyond the current available nano-fabrication technique. Second, the SRR type of LHM designs requires the incident EM wave to be parallel to the SRR plane, and, therefore, multiple layers of sample are needed to observe strong enough left-handed responses. It is very difficult to realize the parallel incidence in the optical regime.

By using the short wire pair structure, these technique difficulties can be overcome. The short wire pairs are simple enough to be realized by the current nano-fabrication process. In addition, the incident EM wave is perpendicular to the sample plane. This allows us to obtain a strong enough left-handed response from only one layer of sample. Using short wire pair design, we are able to realize left-handed materials from microwave frequency up to the optical regime.

3.1 Geometry of Short Wire Pair

As mentioned previously, the short wire pair geometry can be viewed as an extreme case of a two-gap SRR. Figure 3.1 shows the transformation from a two-gap SRR to the short wire pair by increasing the gap size. We systematically studied the magnetic resonances of two-gap SRRs as we gradually increased the size of the gap. It turns out the magnetic resonances

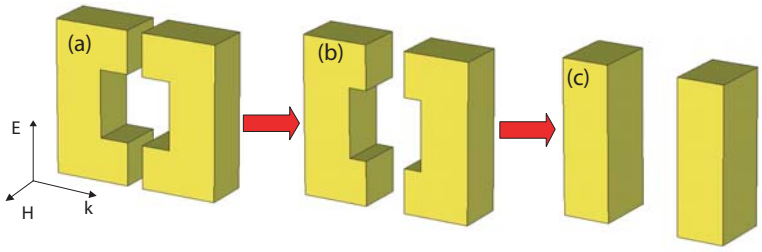

Figure 3.1 By gradually increasing the gap size of a two-gap SRR (a,b), the short wire pair structure (c) is obtained.

always exist as the size of gap increases from case of 3.1(a) to 3.1(c).

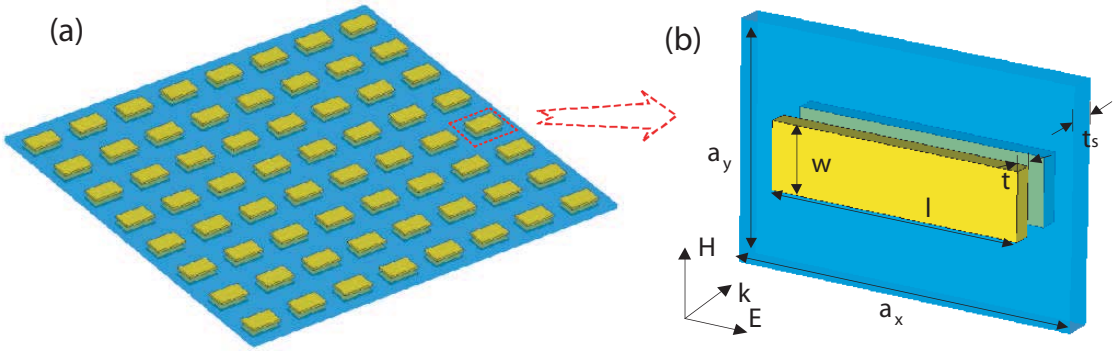

Figure 3.2 (a) The short wire pair arrays (SRRs) with repeating distance, a_x and a_y. (b)Single unit cell of the SRR with geometric parameters given as following: the length, l, the width, w, and the thickness, t, of the wires, the thickness of the dielectric spacer, t_s.

Unlike the SRRs, which must be fabricated as a planar structure on the top of a substrate, the short wire pair can be fabricated on a dielectric substrate layer-by-layer separated by a dielectric material. For microwave frequency applications, it is even more convenient to fabricated it on two sides of a PC board. An array of short wire pairs together with a detailed view of a single unit cell are shown in Fig. 3.2. The short wire pair consists of a pair of metal patches separated by a dielectric spacer of thickness t_s. In essence, the short wire pair is a "two-gap" SRR that has been flattened to result in the wire-pair arrangement [44]. For an electromagnetic wave incident with wave vector and field polarization as shown in Fig.

3.2(b), the short wire pair will exhibit both inductive (along the wires) and capacitive (between the upper and lower adjacent ends of the short wires) behavior and will possess a magnetic resonance providing a negative permeability.

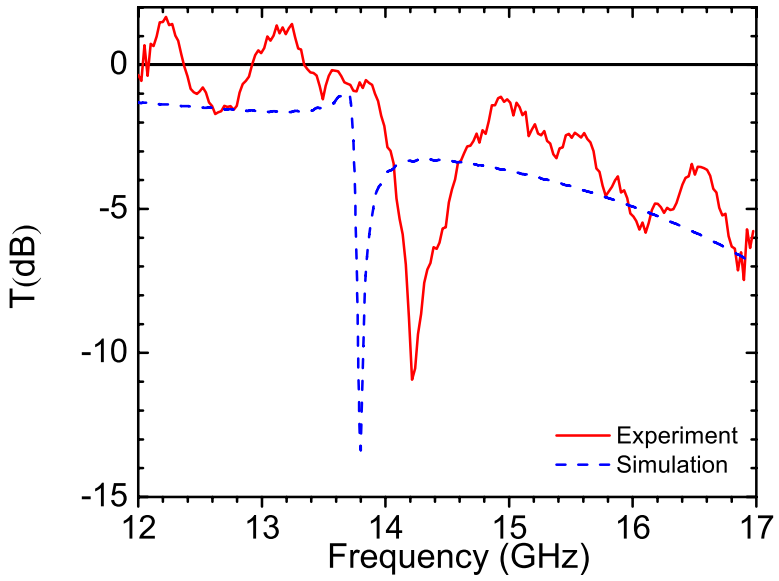

Figure 3.3 Measured (red solid) and simulated (blue dash) transmission of the short wire pair with $l = 7$ mm, w=1 mm, $t = 10$ μm, t_s=0.254 mm. (Definition of parameters see Fig. 1.2)

Figure 3.3 shows the transmission spectra of the short wire pair structure under a normal incidence of plane EM wave with the polarization shown in Fig. 3.2(b). The red and blue curves show measured and simulation results, respectively. The sample was prepared on a Rogers 5880 PC board with dielectric constant, $\epsilon_r = 2.53$, and the wires were made from copper. A dip at 14.3 GHz in the measured curve and at 13.8 GHz in the simulation curve were shown. Further study shows that the transmission dips are due to magnetic resonances. One may notice there is considerable discrepancy between the measured and the simulated curves, which is related to a few factors in the experiment and fabrication process. We will return to this issue later after we discuss the mechanism of the magnetic resonances.

3.2 Magnetic Resonance of the Short Wire Pair

The transmission spectra of the short wire pair in Fig. 3.3 show resonance dips under normal incidence of EM waves. As we know, the resonance could be either an electric response or a magnetic response. The magnetic resonance usually originates from the circular current, while the electric resonance usually is excited by the linear current. In order to determine the resonance of the short wire pair, we studied the electric and magnetic fields distributions and the current distributions.

3.2.1 The electric field, E, and the magnetic field, H, distribution

The electric field, **E**, in the region between the short wires is shown in Fig. 3.4(a) and (b).

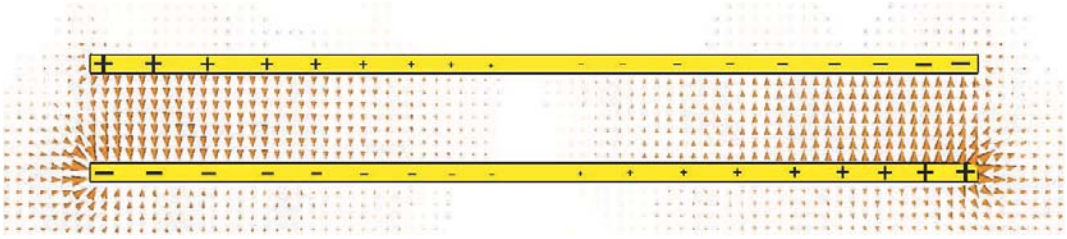

(a)

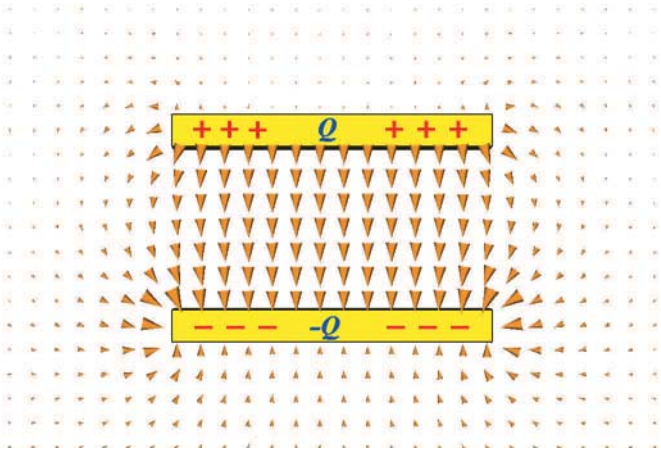

(b)

Figure 3.4 The electric field at 13.8 GHz on the plane perpendicular to the magnetic field, **H**, direction (a) and on the plane perpendicular to the electric field, **E**, direction (b).

We found the following properties of the electric field distribution:

1. Strong localized electric field, $\mathbf{E}_{\text{loc}}$, exists in the space between the short wires. The magnitude of localized field is much larger the electric field of the incident EM wave, $\mathbf{E}_{\text{i}}$, and the direction of $\mathbf{E}_{\text{loc}}$ is perpendicular to $\mathbf{E}_{\text{i}}$.

2. $\mathbf{E}_{\text{loc}}$ reaches its maximum magnitude at the ends of wires and decreases to zero at the center.

3. $\mathbf{E}_{\text{loc}}$ at the ends of the wires are along opposite directions, which indicates the opposite sign charges accumulating at those ends (Fig. 3.4(a)).

Figures 3.5(a) and (b) show the magnetic field distribution.

We found the following properties of the magnetic field distribution:

1. Strong localized magnetic field, $\mathbf{H}_{\text{loc}}$, exists in the space between the short wires. The magnitude of localized field is much larger the magnetic field of the incident EM wave, $\mathbf{H}_{\text{i}}$, and the direction of $\mathbf{H}_{\text{loc}}$ is same as $\mathbf{H}_{\text{i}}$.

2. The magnitude of $\mathbf{H}_{\text{loc}}$ reaches maximum value at the center of the short wires and decreases to zero toward the ends.

3. According to $\mathbf{H}_{\text{loc}}$ field distribution, anti-parallel currents flow in the short wires.

From the magnetic field distribution shown in Fig. 3.5(b), we clearly see the anti-parallel currents exist in the short wires. These anti-parallel currents, induced by the magnetic field of the incident EM wave, behave similarly as the loop currents in SRRs, and, therefore, result in a magnetic resonance.

3.2.2 *RLC* effective circuit model

Similar to SRRs, the short wire pair can also be modeled as an RLC circuit which consists of two inductors and two capacitors in series as shown in Fig. 3.6. The resonant frequency of this RLC circuit is given by,

$$f = \frac{1}{2\pi\sqrt{LC}} \quad , \tag{3.1}$$

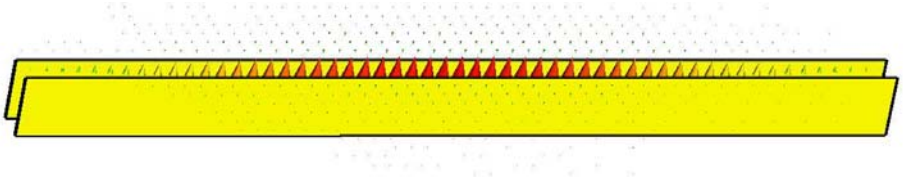

(a)

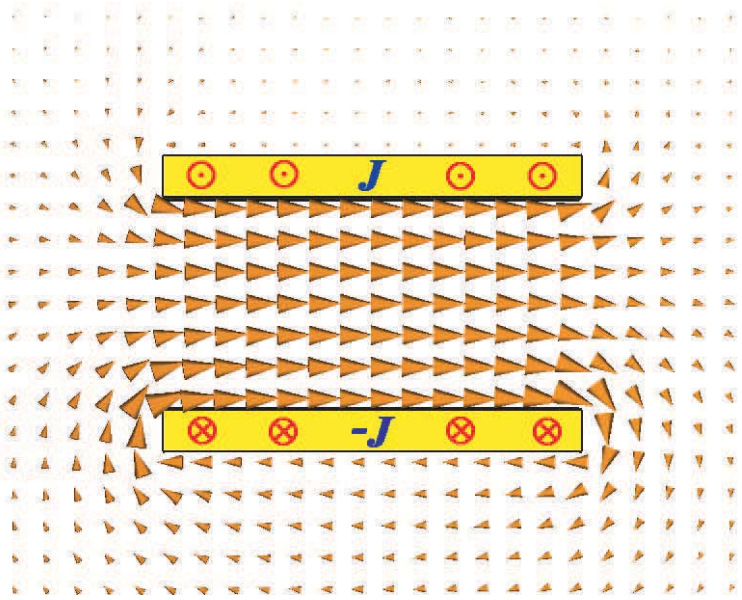

(b)

Figure 3.5 The magnetic field at 13.8 GHz on the plane perpendicular to the magnetic field, **H**, direction (a) and on the plane perpendicular to the electric field, **E**, direction (b).

where L and C is the total inductance and total capacitance of the RLC circuit.

At the resonant frequency, anti-parallel currents are induced by the magnetic field of the incident EM wave, therefore, an effective inductance, L, can be defined by

$$L = \frac{\Phi}{I} \quad , \tag{3.2}$$

where Φ is the magnetic flux flowing through the area enclosed by the short wires. On the other hand, charges with opposite signs accumulate at the ends of the short wires as shown in Fig. 3.4(a), so the an effective capacitance can be defined by,

$$C = \frac{Q}{U} \quad , \tag{3.3}$$

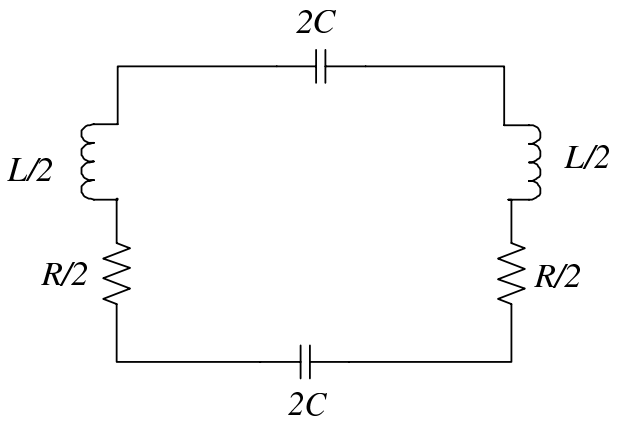

Figure 3.6 The RLC effective circuit model

where U is the voltage difference between the ends of short wires.

The short wire pair can be considered as two parallel plates, so the inductance, L, is approximately given by

$$L = \mu \frac{t_s}{w} l \quad , \tag{3.4}$$

where l and w are the length and width of the short wires, respectively, and t_s is the thickness of the dielectric spacer. [1]

The capacitance, $2C$, of the short wire pair are the capacitance of parallel plates, given by,

$$2C = \epsilon_r \frac{w}{t_s} \frac{l}{2}.$$

where ϵ_r is the dielectric constant of the dielectric spacer. The total capacitance, C, of the series RLC circuit is given by

$$C = \epsilon_r \frac{w}{t_s} \frac{l}{4} \quad . \tag{3.5}$$

Thus, we obtain the magnetic resonance frequency as the following,

$$f_m = \frac{1}{2\pi\sqrt{LC}} = \frac{1}{\pi\sqrt{\epsilon\mu}} \frac{1}{l} = \frac{c_0}{\pi\sqrt{\epsilon_r}} \frac{1}{l} \quad , \tag{3.6}$$

where c_0 is the speed of light in a vacuum. One immediately sees that the resonance frequency, f_m, is inverse proportional to the length of the wires, l, and does not depend on other geo-

[1] This formula describes the inductance of parallel plate with infinite length. Since the separation between short wires, $t_s = 0.254$ mm, is much smaller than the length $l = 7$ mm, this formula is valid for the short wire pair.

metric parameters, such as the width, w, and the separation between the short wires, t_s. This interesting property has been confirmed by numerical simulations as shown later in Fig. 3.12.

3.2.3 Inductance L and capacitance C of short wire pair

As mentioned in the previous section, Eq. (3.6) also shows that the resonance frequency, f_m, does not depend on the geometric parameters, w and t_s. This observation coincides with our numerical simulations. In addition, our simulations show that Eq. (3.6) is valid even for a very thin short wire pair, i.e., $w \ll t_s$, where the inductance and capacitance cannot be modeled by a pair of parallel plates, and hence Eq. (3.4) and Eq. (3.5) are invalid. To explain this behavior, we studied the capacitance and inductance of two extreme cases,

- $l \gg t_s$ and $w \gg t_s$. This is the case of two parallel plates as shown in Fig. 3.7(a).
- $l \gg t_s$ and $w \ll t_s$. This is the case of two parallel thin wires as shown in Fig. 3.7(b).

Next, we will discuss the inductance and capacitance of parallel plates and parallel wires by using Eq. (3.2).

Figure 3.7(a) shows a parallel plates model of the short wire pair with $l \gg t_s$, $w \gg t_s$. Assuming the electric and magnetic field are uniform in the region between the parallel plates, the magnetic flux is given by

$$\Phi = \mu \int \mathbf{H} \cdot \mathrm{d}\mathbf{S} = \mu H \cdot t \cdot l \quad .$$

According to the analysis in section 3.2.1, anti-parallel current exists on the plates. Employing Ampère's Law

$$\oint \vec{H} \cdot \mathrm{d}l = H \cdot w = I \quad .$$

So, the effective inductance L is obtained by

$$L = \mu \frac{t}{w} l \quad ,$$

which is already given in Eq. (3.4). The capacitance of the parallel plates is given by Eq. (3.5) (well-known plate capacitor formula). Thus, in the product of L and C, w and t cancel, hence,

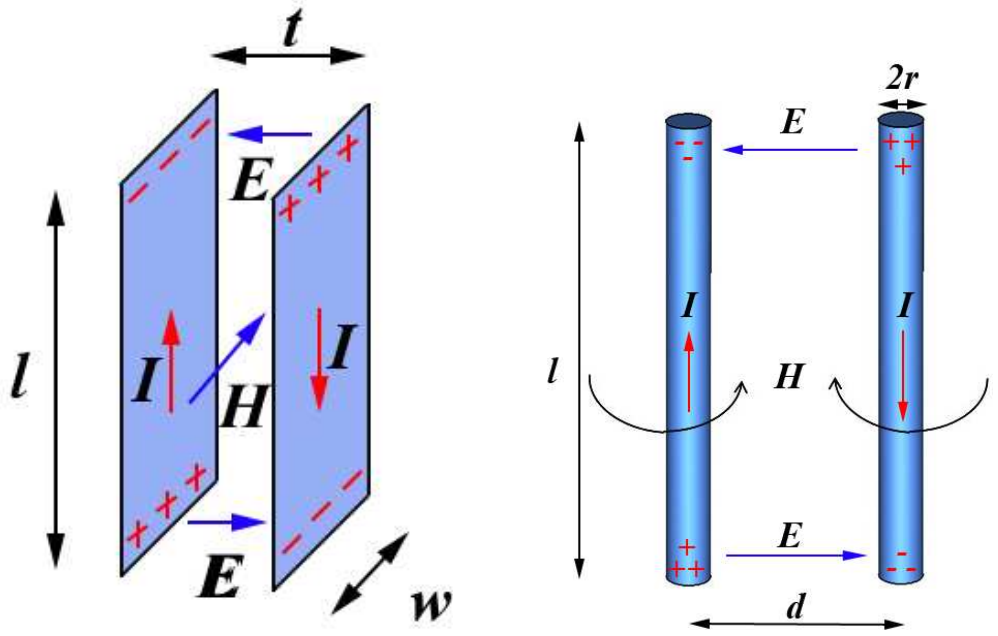

(a) (b)

Figure 3.7 (a): The parallel plates model of a short wire pair with $l \gg t_s$ and $w \gg t_s$, (b): The parallel thin wires model of a short wire pair with $l \gg t_s$ and $w \ll t_s$, The current, I, charges, Q, the electric fields, $\mathbf{E}$, and the magnetic field, $\mathbf{H}$ are shown.

the magnetic resonant frequency f_m is given by

$$f_m = \frac{c_0}{\pi\sqrt{\epsilon_r}}\frac{1}{l} \quad ,$$

which is same as Eq. (3.6).

Figure 3.7(b) shows a parallel thin wires model of the short wire pair with $l \gg t_s$, $w \ll t_s$. The total magnetic field is the superposition of the magnetic field around two individual wires. On the plane through the center line of two wires, the magnetic field is along the normal direction. Using Ampère's Law, the magnetic field in the region between the wires is given by,

$$H = \frac{I}{2\pi}\Big(\frac{1}{x} + \frac{1}{d-x}\Big) \quad ,$$

where the origin of the x-axis is the center of the left wire. The magnetic flux is evaluated by the integration of $\mathbf{H}$ in the area between the wires,

$$\Phi = \mu \int \mathbf{H}\cdot \mathrm{d}\mathbf{S} = \frac{\mu I}{2\pi}\int_r^{d-r}\Big(\frac{1}{x} + \frac{1}{d-x}\Big)\mathrm{d}x = \frac{\mu I}{\pi}\ln\Big(\frac{d-r}{r}\Big).$$

Thus the inductance is given by,

$$L = \frac{\Phi}{I} = \frac{\mu l}{\pi} \ln\Big(\frac{d-r}{r}\Big). \tag{3.7}$$

where d is the distance between the wires and r is the radius of the each wire.

According to Eq. (3.3), to evaluate the capacitance between the wires, one needs to know the voltage difference between the wires, given by the integration of the **E** field. Employing Gaussian Law,

$$\oint \mathbf{E} \cdot \mathrm{d}\mathbf{S} = \frac{Q}{\epsilon} \quad .$$

Thus, the electric field, **E**, is along the radial direction and its magnitude is given by

$$E = \frac{Q}{2\pi\epsilon l}\Big(\frac{1}{x} + \frac{1}{d-x}\Big) \quad .$$

So the voltage difference between wires is given by,

$$U = \int_r^{d-r} E\mathrm{d}x = \frac{Q}{2\pi\epsilon l}\int_r^{d-r}\Big(\frac{1}{x} + \frac{1}{d-x}\Big)\mathrm{d}x = \frac{Q}{\pi\epsilon l}\ln\Big(\frac{d-r}{r}\Big) \quad .$$

Thus, we obtain the capacitance,

$$C = \frac{Q}{U} = \frac{\pi\epsilon l}{\ln\left(\frac{d-r}{r}\right)} \quad . \tag{3.8}$$

From the Eq. (3.7) and (3.8), in the product of L and C, r (which corresponds to w for short wire pair) and d (which corresponds to t_s for short wire pair) cancel again; hence, the magnetic resonant frequency f_m is given by

$$f_m = \frac{c}{\pi\sqrt{\epsilon_r}}\frac{1}{l} \quad ,$$

which is also same as Eq. (3.6).

As shown above, both the parallel plates model and the parallel thin wires model give the same equation for the resonance frequency. This explains the unexpectedly wide range of the observed $1/l$ dependence.

After understanding the relationship between the magnetic resonance frequency, f_m, and geometric parameters, let's return to the issue about the discrepancy of magnetic resonance between the measured and simulated transmission curves shown in Fig. 3.3. The frequency

discrepancy of the magnetic resonances is a result of several factors. First, the dielectric constant used in the simulation, $\epsilon_r = 2.53$, given by the data sheet of Rogers 5880 PC board, may be slightly different to the actual value at the resonance frequency, due to the frequency dispersive nature of the real dielectric material. Since the resonant frequency is proportional to $1/\sqrt{\epsilon_r}$ (as shown in Eq. (3.6)), the actually value of ϵ_r is smaller than 2.53. Second, after measuring the length and the width of the short wires under the microscope, we found the short wires are over-etched in the fabrication process. Thus the actual lengths of the short wires are shorter than the designed length. As shown in Eq. (3.6), the magnetic resonant frequency is proportional to $1/l$, a shorter length, l, will increase the resonance frequency. Moreover, since the wires are over-etched in a nonuniform manner, the actual lengths of wires are different. Consequently, the resonance frequencies of the short wire pair are also different. This explains the fact that the width of the dip of the measured curve is much wider than the simulated one. Finally, during the fabrication process, the short wires must be fabricated on both sides of the PC board, so misalignment between the two sides of the PC board may happen. The misalignment of the short wires will shorten the length of the short wire pair effectively, and, therefore, increase the resonant frequency, f_m.

3.3 Effective Parameters for the Short Wire Pair

Figure 3.8 shows the simulated transmission, T, reflection, R, and loss, A for the short wire pair structure with the same geometric parameters shown in Fig. 3.3. The loss is calculated by $A = 1 - T - R$. As expected, a dip in the transmission at 13.8 GHz is observed. In addition, the peak in the loss at the same frequency indicates significant absorption exists at the magnetic resonance frequency. A major contribution to the absorption comes from the ohmic loss in the metallic wires.

Figures 3.9(a)-3.9(d) show the effective parameters, i.e. the refractive index, n, the permeability, μ, the permittivity, ϵ, and the impedance, z, of the short wire pair design, which are extracted by a retrieval procedure [28]. A resonance behavior was shown in the refractive index (Fig. 3.9(a)); however, similar to the SRRs, the short wire pair alone does not provide a

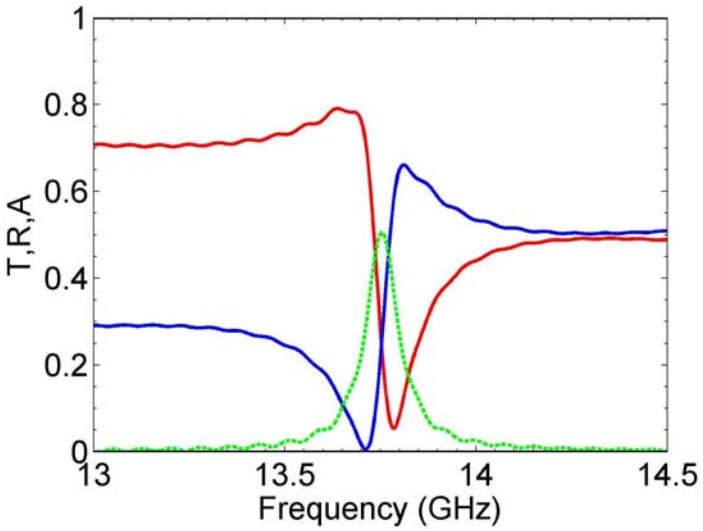

Figure 3.8 Simulated transmission, T (blue), reflection, R (red), and losses, A (green) using short wire pair structure shown in Fig. 3.2.

negative refractive index. Figure 3.9(b) clearly shows a magnetic resonance at 13.8 GHz, which leads to negative values of the permeability around the resonance frequency. An anti-resonance of the permittivity appears in Fig. 3.9(c), due to the periodicity effect [33].

3.4 Electric Response of Short Wire Pair

Similar to the short-wire-like response discussed in Chapter 2, the short wires also support electric resonance. Figure 3.10 shows the electric field distribution of a short wire pair at the electric resonance frequency f_e. Unlike the case of the magnetic resonance shown in 3.4(a), the electric field of the electric resonance is along the wire direction and mainly confined in the space between the nearest neighbor edges of the two pairs of bars belonging to consecutive unit cells. The charges accumulate at the ends of the wire pair and have the same sign at the same end. Such charge distributions indicate the symmetric current mode exists in the wires.

The electric resonance can also be modeled as an RLC circuit. Considering the field and current configurations for both the antisymmetric mode of the magnetic resonance and the symmetric mode of the electric resonance, the short wire pairs can be modeled by equivalent R, C, L circuits as shown in Fig. 3.11 (where for simplicity the resistor elements have been

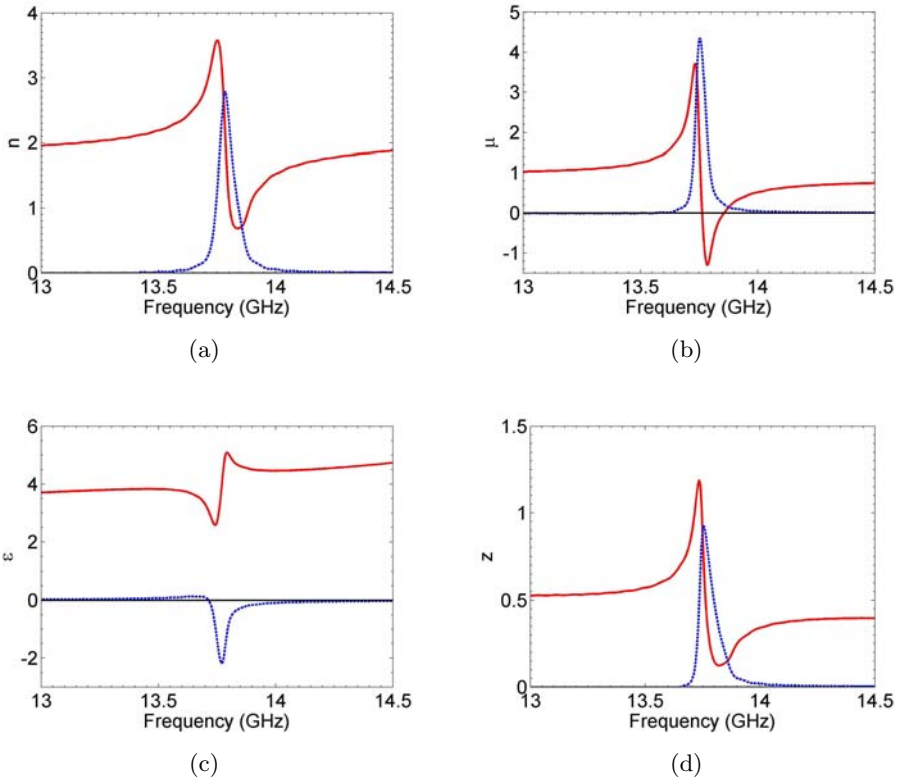

Figure 3.9 Retrieval calculation using simulation data. (a): refractive index n, (b): permeability μ, (c): permittivity ϵ, (d): impedance z. Red curves show the real part and blue curves show the imaginary part.

omitted). Near the magnetic resonance frequency where the current configuration is as shown in Fig. 3.11(c), the magnetic field is between the two plates and, to a good approximation, uniform (Fig. 3.5(b)). Hence, the total inductance L, as calculated by the magnetic field flux, is given by Eq. (3.4) and rewritten as,

$$L = 2L_m \simeq \mu \frac{t_s}{w} l,$$

where l is the length of the wire, t_s is the thickness of the dielectric spacer, and w is the width of the wire.

Notice that at telecommunication or optical frequencies, where the linear dimensions are in the tens or hundreds of nm, the kinetic energy of the drifting electrons makes a contribution comparable or larger than the magnetic energy. Hence, another additional inductance must be added to the right-hand side of Eq. (3.4) [41].

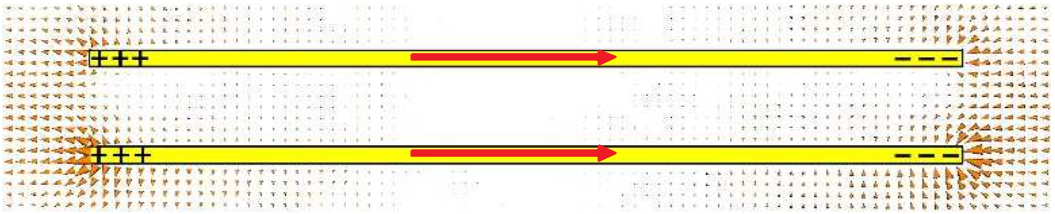

Figure 3.10 Electric field distribution at the electric resonance frequency, f_e. The sign of charges and the direction of current (red arrows) are also shown.

Each of the capacitance, C_m, is already given by a Eq. (3.5) and rewritten as,

$$C_m = \frac{\epsilon w l}{t_s} \quad . \tag{3.9}$$

The capacitance, C_e, can be approximated by that of two parallel wires of radius, t_m, and length, w, at a distance, b, apart

$$C_e = \frac{\pi \epsilon w}{\ln(b/t_m)}, \tag{3.10}$$

where t_m is the thickness of each metallic bar and b is the separation of the neighboring pairs Fig. 3.11(a,b) ($b = a_y - l$). The magnetic resonance frequency, ω_m, is obtained by equating the impedance Z (of L_m and C_e in parallel) minus the impendence $-i/C_m\omega$ of the capacitance C_m.

Since $Z = iL_m\omega/(1 - L_m C_e \omega^2)$, we obtain

$$\omega_m = \frac{1}{\sqrt{L_m(C_m + C_e)}} \simeq \frac{1}{\sqrt{L_m C_m}} \quad . \tag{3.11}$$

The last relationship follows because, for the values we have used, ($l = 7\text{mm}, w = 1\text{mm}, t_s = 0.254\text{mm}, t_m = 10\mu\text{m}$ and $b = 0.3\text{mm}$), $C_e \simeq 0.1 C_m$. Combining Eqs. (3.4) and (3.9) we find that

$$f_m = \frac{\omega_m}{2\pi} = \frac{1}{\pi\sqrt{\epsilon_r}} \frac{c_0}{l} \quad , \tag{3.12}$$

where $\epsilon_r = 2.53$ is the reduced dielectric constant of the dielectric, $\epsilon_r = \epsilon/\epsilon_0$. In Fig. 3.12 we compare our result of Eq. (3.12), which shows that f_m is a linear function of only $1/l$, with detailed simulations results. Figure 3.12 shows the dependence of the magnetic resonance frequency as obtained from the retrieved resonant effective μ on the inverse length of the parallel

metallic bars (Fig. 4.5b), for different widths w (separation between parallel bars $t_s = 0.254mm$ fixed) and two different separations t_s (width of bars $w = 1mm$ fixed). Complete quantitative agreement is obtained if $c_1 = 0.22$. Notice the independence of the simulation results on the width w and the dielectric thickness t_s. It is worthwhile to point out that the result $f_m \sim 1/l$ is robust over a wide range of parameters, even if Eqs. (3.4) and (3.9) are invalid. To see this point, consider the extreme case of a pair of thin wires (as discussed in section 3.2.3) of length, l, cross-section radius, r, at a distance, d, apart such that $r \ll d \ll l$. For such a system $L = (\mu/4\pi)[1 + 4\ln(d/r)] \simeq (\mu l/\pi)\ln(d/r)$ and $C \simeq \epsilon\pi l/\ln(d/r)$. Thus, again $f_m \sim 1/\sqrt{\epsilon\mu}l$.

For frequencies near the electric resonance, because of mirror symmetry in Fig. 3.11(d), there is no current passing through the capacitances, C_m. As a result the electric resonance frequency, f_e, is given by

$$f_e = \frac{1}{2\pi\sqrt{C_e L_e}} \quad , \tag{3.13}$$

where L_e is expected to be of the form $(\mu/\pi)g(w/l)$, where $g(x)$ is a function which for $x \to 0$ behaves as $-\ln(x)$.

3.5 LHM Based on Short Wire Pairs

Since short wire pairs have both the magnetic resonance and the electric resonance providing negative μ and ϵ, respectively, can we overlap the two resonances and realize a left-handed medium? Our numerical studies show it's very difficult to obtain both negative ϵ and μ at the same frequency band. The electric resonance is much stronger than the magnetic resonance because the electric coupling is much more efficient than the magnetic coupling. Therefore, when the magnetic resonance approaches the electric resonance frequency, the magnetic response will be killed by the strong electric response. The only possibility is to tune the magnetic resonance very carefully and move it to the frequency range where the electric response is weak as shown in Fig. 3.14(b). This requires the electric resonance frequency to be lower than the magnetic resonance frequency, i.e., $f_e < f_m$. We managed to obtain this overlapping at microwave frequency, but are not able to realize it optic regime.

We found that f_e is a rather sensitive function of the small distance, b, because C_e depends

on b, while L_e is practically independent of b. Indeed, the ratios $f_e(2b)/f_e(b)$ and $f_e(3b)/f_e(b)$ for $b = 0.1$mm, according to the equation of C_e and equation of f_e are, respectively 1.14 and 1.215, in good agreement with the simulation results in Fig. 3.13 (1.13 and 1.21, respectively); the dependence of both f_m and f_e on $a_y/l = 1 + b/l$ is shown in Fig. 3.13.

Figure 3.13 in combination with Fig. 3.14 suggest the optimum design parameters for making the two bar scheme to produce a negative index n: One must avoid the crossing region, where essentially to a considerably degree, the two resonances cancel each other. Since the electric resonance is much stronger and, hence, much wider, we must bring the magnetic resonance within the negative region of ϵ, i.e., we must have f_e lower than f_m as seen in Fig. 3.14(b), rather than the other way around, i.e., we must have

$$\left(\frac{f_e}{f_m}\right)^2 = \frac{L_m}{L_e}\left(1 + \frac{C_m}{C_e}\right) < 1 \quad . \tag{3.14}$$

This can be achieved by increasing C_e either by decreasing b or by increasing at the ends of each bar the width, w, choosing a double H shape for each bar [54] as discussed in the next section.

3.6 LHM by a H-Shaped Short Wire Pair Design

As we have mentioned, we can modify the short wire pair to increase C_e and therefore shift the electric resonance to lower frequency. One of the design is the H-shaped wires shown in Fig. 3.15(a).

The H-shaped short wire pairs were fabricated using Rogers 5880 printed circuit board stock with dielectric-layer thickness of 254 μm and listed relative dielectric constant of 2.53. The circuit board was coated on both sides with 10-μm thick layers of copper. The copper was formed in the wire-pair patterns using conventional photolithography techniques. For the samples reported here (both simulations and experiments), the width of the metal wires was 1 mm. The length and the width of the metal bars at each end of the wire pairs was 4mm and 0.2 mm respectively. The length of the short wire pairs was 4 mm, and the unit cell size was 4.2 mm $\times$ 8 mm $\times$ 2.274 mm. The total sample size was 9 x 17 x 1 unit cells, resulting

in approximately square samples. A photograph of one side of a complete sample is shown in 3.15(b). With these patterned dimensions on the printed-circuit board material, the resonances for LHM-behavior were expected to occur near 15.8 GHz.

The calculated and measured transmission spectra are shown in Fig. 3.16. There is good qualitative agreement between simulations and measurements. To demonstrate the appearance of the expected left-handed transmission band more clearly than it is visible from the single unit cell spectra, we include the simulated transmission through five unit cells as the dashed line.

The extracted refractive index is shown in Fig. 3.17 and the extracted permittivity and permeability are shown in Fig. 3.18. The plots show that the real part of the permittivity is negative over most of the measured range. The real part of the permeability is negative over a resonance band above 15.8 GHz for both of the simulation (approximate 15.87-16.00 GHz) and the measurement (approximate 15.82-15.98 GHz). The extracted real part of the refractive index is negative over a narrow band around 15.8 GHz for both of the simulations (15.59-16.17 GHz) and the experiments (15.67 -16.02 GHz), dipping as low as -2.66 using measured data and -2.86 from the simulation. The ratio of the imaginary part of n to the real part of n reaches 1/3 above the resonance, which means that we have left-handed propagation with and n negative. The simplicity of the short-wire pair design and the alleviation of the need for continuous wires generating the negative effective permittivity is expected to facilitate scaling of the structure to achieve left-handed response well within the THz region. However as we discussed in chapter 2, straightforward geometric scaling of the present design is not possible as the behavior of the metals changes from lossy conductors in GHz to lossy, negative dielectrics in the higher THz region [41].

3.7 Conclusions

The short wire pair design, which has a distinct advantage over the conventional SRRs design, is more suitable for building LHM at the optical regime. The short wire pairs support both the electric and the magnetic resonances, which are exited by the parallel current and

the anti-parallel current, respectively. After studying the fields and currents distributions, we present an effective RLC circuit model of the short wire pairs. Negative refractive index can be realized by overlapping the electric and the magnetic resonances. We discuss the criteria to overlap these two resonance. Finally, we demonstrate the negative refractive index experimentally by using a H-shaped short wire pair design.

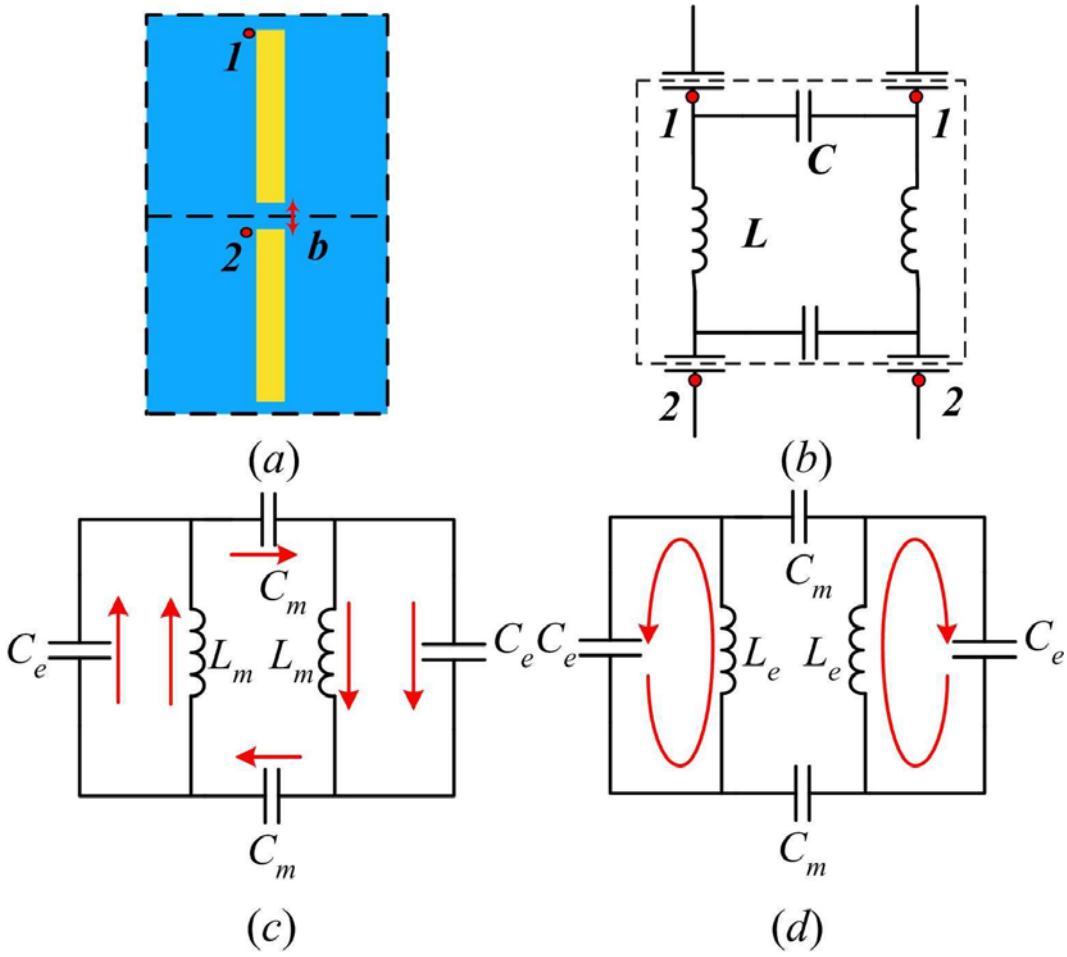

Figure 3.11 (Color online) Current distribution of the two parallel metallic bar design (a) (side view, the parallel plates are behind one another) can be accounted for by the equivalent circuit (b), which, since points 1 and 2 are equivalent because of the periodicity, reduces to circuit (c) and (d) for the magnetic (c) and electric (d) resonance respectively.

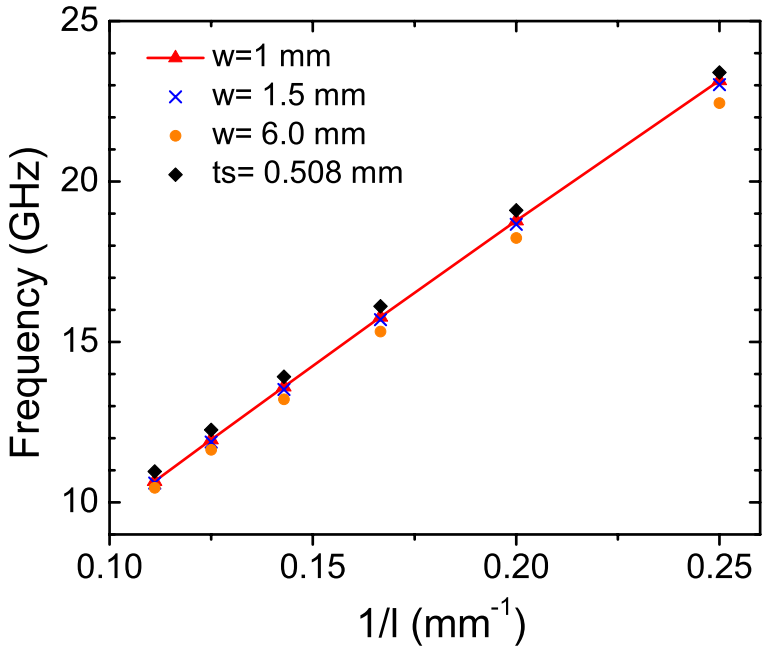

Figure 3.12 (Color online) Linear dependence of the magnetic resonance frequency, f_m, as obtained by simulation, on the inverse length l; this result as well as its independence on w and t_s is in agreement with the simple formula (3.12). ($t_s = 0.254mm$ for triangular, cross, circle; $w = 1mm$ for diamond; and for all cases, $b = 0.5 \sim 5.5mm$, $a_x = 20mm$).

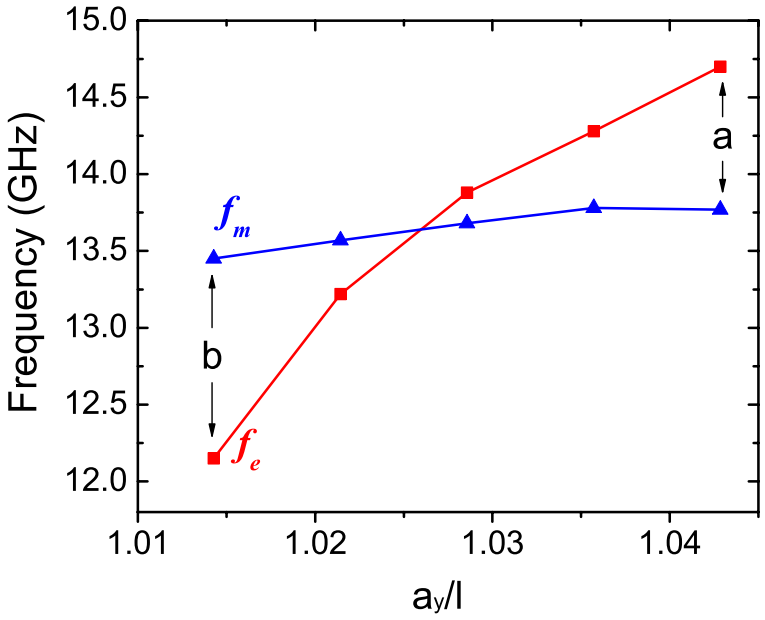

Figure 3.13 (Color online) Magnetic resonant frequency f_m cross over with electrical resonant frequency f_e as $a_y/l = 1 + b/l$ varies between 7.1mm and 7.3mm; $a_x = 20$mm.

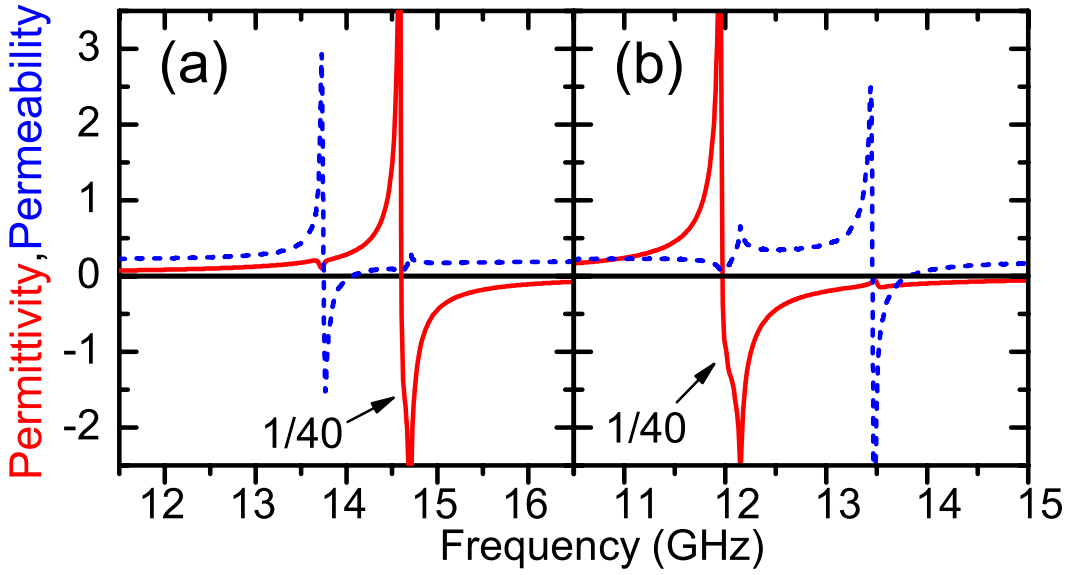

Figure 3.14 (Color online) Retrieved ϵ_{eff} (solid lines) and μ_{eff} (dotted lines) for two cut wires. (a) and (b) correspond to points a ($a_y = 7.3$mm, $a_x = 20$mm) and b ($a_y = 7.1$mm, $a_x = 20$mm) in Fig. 3.13. Notice that both responses are Lorentz like.

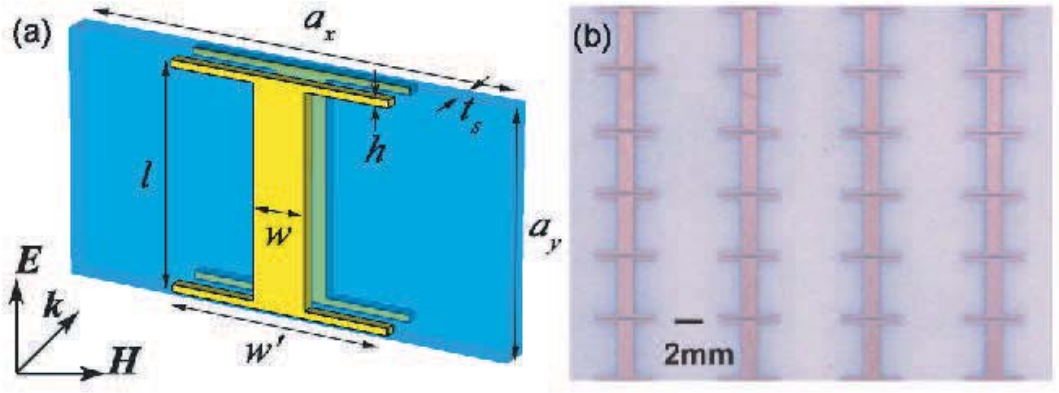

Figure 3.15 (a) Schematic representation of one unit cell of the wire-pair structure. (b) Photograph of fabricated microwave-scale wire-pair sample.

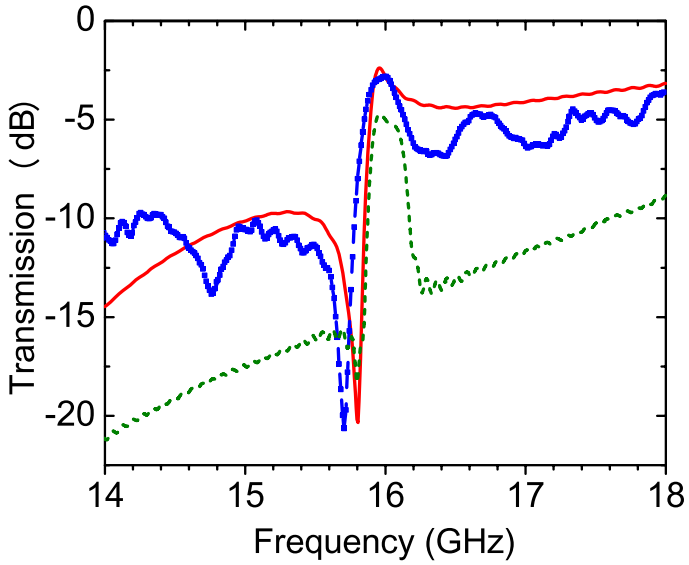

Figure 3.16 (Simulated (red solid curve) and measured (blue dotted curve) transmission spectra for electromagnetic radiation incident on the wire-pair structures. The green dashed curve shows the simulated transmission spectrum for a 5-layers sample.

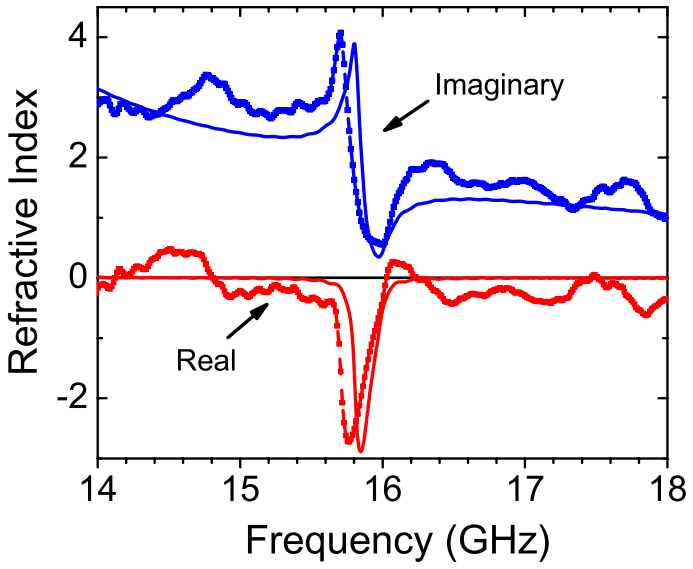

Figure 3.17 Extracted refractive index n of a periodic array of wire-pair unit cells, using the simulated (solid curves) and measured (dotted curves) transmission and reflection data. The red and blue curves show the real part of n and imaginary part of n respectively.

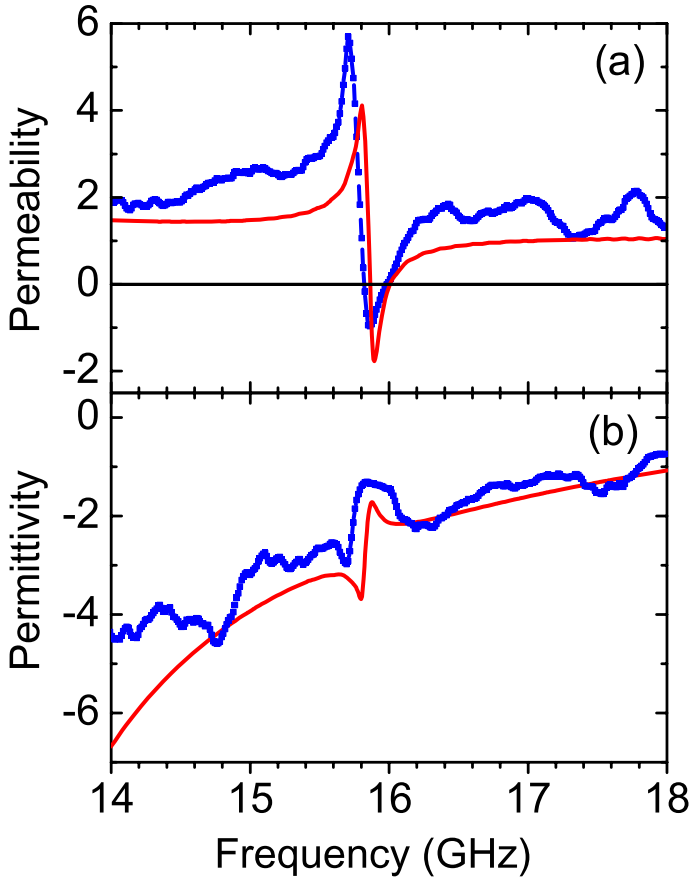

Figure 3.18 Extracted permittivity (a) and permeability (b) of a periodic array of wire–pair unit cells, using the simulated (red solid curves) and measured (blue dotted curves) transmission and reflection data.

CHAPTER 4. LHM BY THE SHORT WIRE PAIRS WITH THE LONG WIRES

Although the short wire pair can provide both the negative permeability, μ, and the negative permittivity, ϵ, it has been shown that it's very hard to overlap the magnetic and electric resonances in a common frequency band. As we have done with the SRR type LHMs, we can add wires arrays, which provide the negative permittivity, ϵ, into the short wire pair design. The resulting composite structures will possess both negative ϵ and μ, and therefore possess negative refractive index.

4.1 The Short Wire Pairs with the Long Wires Design

4.1.1 The geometry of the short wire pairs the with long wires

The basic structure of a single unit cell of the short wire pair NIM is shown in Fig. 4.1A. In the short wire pair arrangement, the conventional SRR is replaced with a pair of short parallel wires and the continuous wires are preserved. In our structure, two additional continuous wires are placed on either side of the short wire pair. Repeating this basic structure periodically in the x, y, and z directions would result in a NIM structure.

To examine the potential usefulness of short wire pair structures as NIMs, we characterized the properties of the short wire pair of Fig. 4.1A using simulations and microwave measurements and then used these results to determine the expected properties of NIMs built from the short wire pair building blocks. Simulations of short wire pair structures were done with CST Microwave Studio (Computer Simulation Technology GmbH, Darmstadt, Germany), which uses a finite-difference time-domain method to determine reflection/transmission properties of metallic-dielectric structures. In the simulations, the dielectric properties of the metal patches

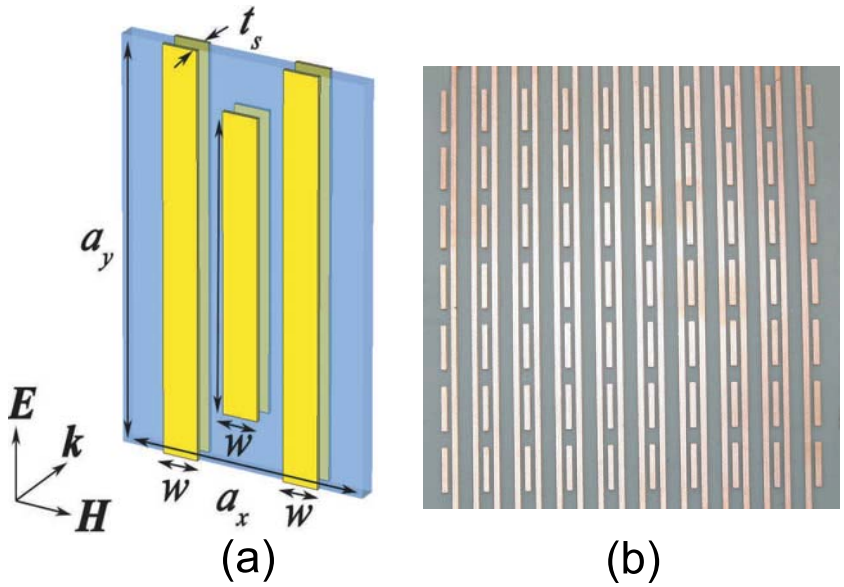

Figure 4.1 (a) Schematic representation of one unit cell of the short wire pair structure. (b) Photograph of one side of a fabricated microwave-scale short wire pair sample.

were handled with a frequency-dependent Drude model. The detailed calculations were used to determine reflection and transmission coefficients from a single unit cell. Experimental transmission and reflection data were obtained by building and measuring microwave-frequency versions of the short wire pair structures. These were fabricated using Rogers 5880 printed circuit board stock with dielectric-layer thickness of 254 μm and listed relative dielectric constant of 2.53. The circuit board was coated on both sides with 10-μm-thick layers of copper. The copper was formed in the short wire pair patterns using conventional photolithography techniques. For the samples reported here (both simulations and experiments), the widths of all metal lines was 1 mm. The length of the short wire pair was 7 mm, and the unit cell size was 9.5 $mm\times$ 7 $mm\times$ 2.274 mm. The total sample size was 7 $\times$ 10 $\times$ 1 unit cells, resulting in approximately square samples. A photograph of one side of a complete sample is shown in Fig. 4.1B. With these patterned dimensions on the printed-circuit board material, the resonances for NIM-behavior were expected to occur near 13.7 GHz

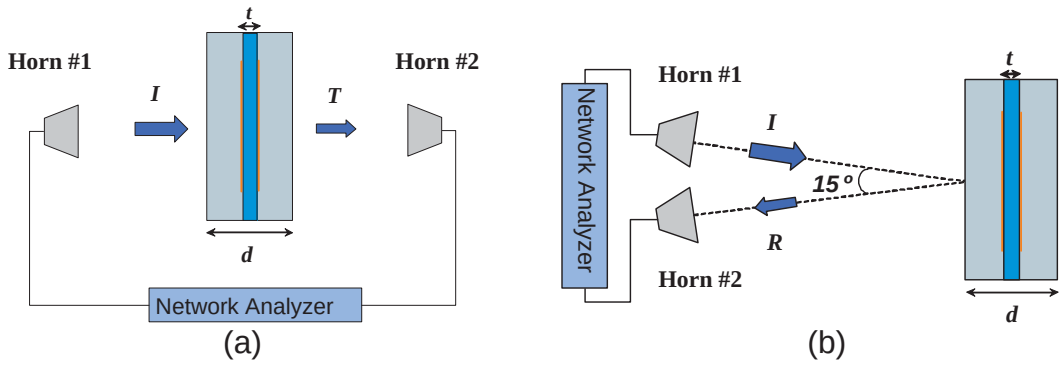

Figure 4.2 The experiment setup for the transmission measurement (a) and the reflection measurement (b).

4.1.2 The transmission and reflection response

Transmission and reflection properties of a single-layer structure were measured over the frequency range of 12 GHz - 16 GHz using a network analyzer (HP 8510) and a pair of standard gain horn antennas serving as source and receiver, as shown in Fig. 4.2. In the transmission measurements, the microwaves were incident normal to the sample surface, as shown in Fig. 4.2(a). This is a tremendous simplification relatively to the conventional SRRs and wires where the incident electromagnetic waves have to propagate parallel to the sample surface. With the conventional orientation of the SRRs, it is almost impossible to do these type of measurements at the THz region, since only single-layer samples are usually fabricated [36, 38]. Transmission measurements were calibrated to the transmission between the horns with the sample removed. As shown in Fig. 4.2(b) the reflection measurements were done by placing the source and receiving horns on the same side of the sample and bouncing the microwave signal off the sample. The source and receiver horns were each inclined with an angle of about 7.5° with respect to normal on the sample surface. The reflection measurement was calibrated using a sample-sized sheet of copper as reflecting mirror. In both measurements, the electric field of the incident wave was polarized parallel to the long dimension of the wires. (For perpendicular polarization, the transmission was nearly 100%, independent of frequency in the resonance region, and reflection was essentially zero.)

The calculated and measured transmission spectra are shown in Fig. 4.3(a). Figure 4.3(b)

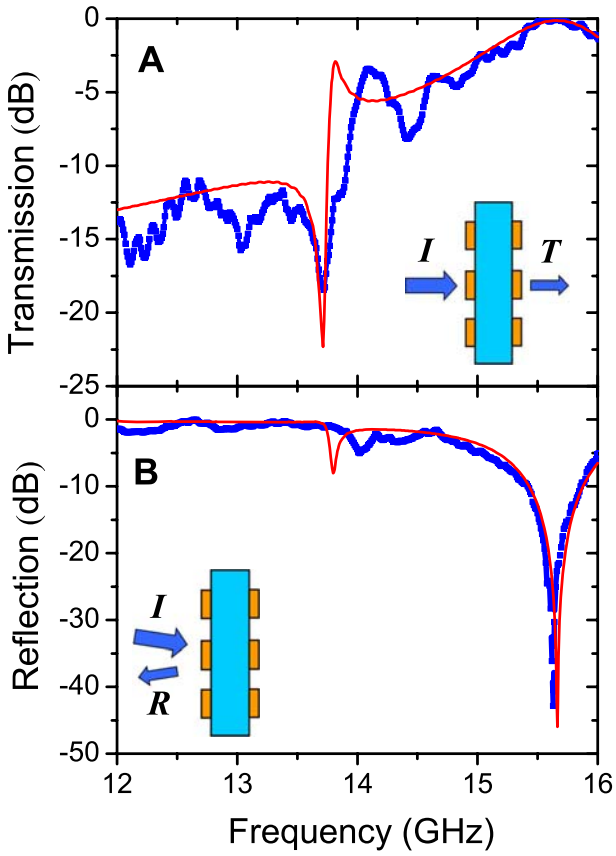

Figure 4.3 Simulated (red thin line) and measured (blue thick dotted line) response to electromagnetic radiation incident on the short wire pair structures: (a) transmission, (b) reflection.

shows the calculated and measured reflection spectra. There is good qualitative agreement between simulations and measurements. The measured spectrum does show resonance peaks and valleys due to reflections between the receiving horn and the sample. Also, there is a distinct frequency difference between critical points in the two sets of curves. The frequencies of measured transmission resonance peak and the corresponding reflection dip near 14.0 GHz are about 2% higher than in the simulations. There are there three potential causes for the shift: 1) The external resonances in the measurements may be masking the true peak (dip) in the measured data. 2) The actual dielectric constant of the circuit board material may be slightly lower than the value used in the simulations. 3) The wires on the front and back of the dielectric layer may be misaligned slightly, which would have the same effect as shortening

the wires. The dip in the reflection at 15.7 GHz is due to the fact that the sample impedance $z = 1$ at that frequency, and so no reflection is possible.

4.1.3 The effective parameters

Using the transmission and reflection results from a single layer, we can extract the effective refractive index that would result if a periodic multi-layer sample were built using the single-layer structure as a building block. The details of the numerical retrieval procedure have been described in detail elsewhere [28, 34, 33].

In performing the retrieval, we have assumed a z-direction size of the unit cell of 2.274 mm. This inter-layer spacing is an adjustable parameter in the retrieval process. Smaller spacing would lead to stronger negative index features in the periodic structure, as long as the distance between the short wires is small compared to the length of the unit cell, but may also result in more complicated fabrication procedures in building a multi-layer structure. In choosing 2.274 mm as the separation distance for the numerical extraction, we attempted to strike a balance between good negative-index properties and having a separation distance that is in line with the other feature sizes of the structure. The extracted permittivity, permeability, and refractive index are shown in the various parts of Fig. 4.4. The plots show that the real part of the permittivity is negative over most of the measured range. [1] The real part of the permeability is negative over a resonance band near 13.8 GHz for the simulation and at about 14.0 GHz for the measurement. Notice also that the product of $\mathrm{Im}(\epsilon)$ and $\mathrm{Im}(\mu)$ is negative. This is well known and real effect which comes from the periodic effects of the retrieval procedure [38]. It is not relevant to the discussion of our results. The extracted real part of the refractive index is negative [2] over a narrow band at 13.8 GHz for the simulations and 14.0 GHz in the

[1] We have also done experiments and simulations for samples with only pairs of short wires. For this case both the experiments and the simulations have shown that indeed is negative, however is not negative in this region and therefore n is also not negative. The extra continuous wires are needed to drive to become negative, without changing the magnetic response shown in Fig. 3(c).

[2] In lossy materials is possible to have the real part n to be negative, without having the real parts of ϵ and μ simultaneously negative. This is the case of the recent work of S. Zhang, W.J. Fan, N.C. Panoiu, K.J. Malloy, R.M. Osgood, S.R.J. Brueck. [Phys. Rev. Lett. 95,137404 (2005)]. This can happen if the imaginary parts of ϵ and μ are sufficiently large, because in a lossy material $n = n' + in''$, and we also have that $n = \epsilon z$ and

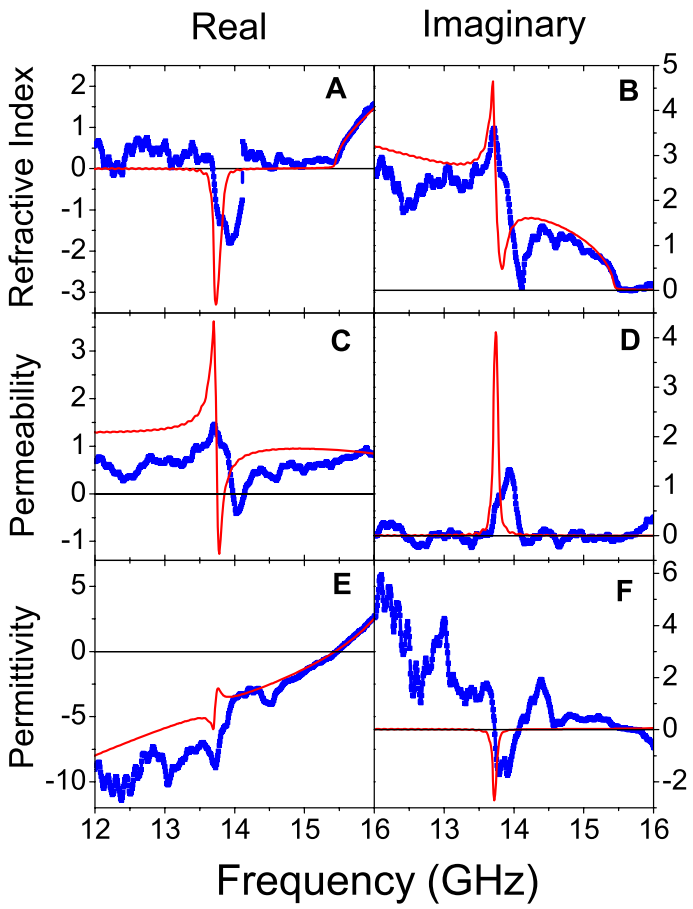

Figure 4.4 Extracted electromagnetic properties of a periodic array of short wire pair unit cells, using the simulated (red thin line) and measured (blue thick dotted line) data of Fig. 2. Real (A) and imaginary (B) part of the refractive index. Real (C) and imaginary (D) part of the permeability. Real (E) and imaginary (F) part of the permittivity. The negative-index behavior can be seen clearly near 14 GHz in (A).

experiments, dipping as low as -2 using measured data and to less than -3 from the simulation. The ratio of the imaginary part of n to the real part of n is $\frac{1}{4}$, which means that we have left-handed propagation with ϵ, μ and n negative. Our preliminary numerical results show if

$z = \sqrt{\mu/\epsilon}$. After some algebra we obtain that $n' = \epsilon' z' - \epsilon'' z''$ and $z = \sqrt{\mu'\epsilon' + \mu''\epsilon''/\epsilon^2 + i(\mu''\epsilon' - \mu'\epsilon''/\epsilon^2)}$, so it's possible to have $n' < 0$, provided that $\epsilon'' z'' > \epsilon' z'$. In this scenario which occurs at the low-frequency side of the $n < 0$ region in Fig. 3A, however, the imaginary parts lead to dominant losses such that we have a transmission gap with some negative phase shift rather than left-handed transmission (with some losses). This type of negative n should not be considered LH behavior. In our experiments, although we have considerable imaginary parts, the behavior is still dominated by the negative real part of n at the high-frequency side where we find the LH behavior. As one can see from the experimental data of Fig. 3A and Fig. 3B, we obtain $n'/n'' = 3.5$ at $n' = -1$, which ratio improves to ~ 15 for $n' = -0.76$. The simulation data gives at least $n'/n'' \approx 3.0$ for $n' = -1.7$.

our structure scale down by a factor of 200, it will give a negative index of refraction at THz frequencies, with both ϵ and μ negative.

4.2 The Fishnet Structure

As another variation of short wire pair design, the fishnet structure was introduced [47, 48], realizing both $\epsilon < 0$ and $\mu < 0$ in the infrared regime and later in the optical regime[49].

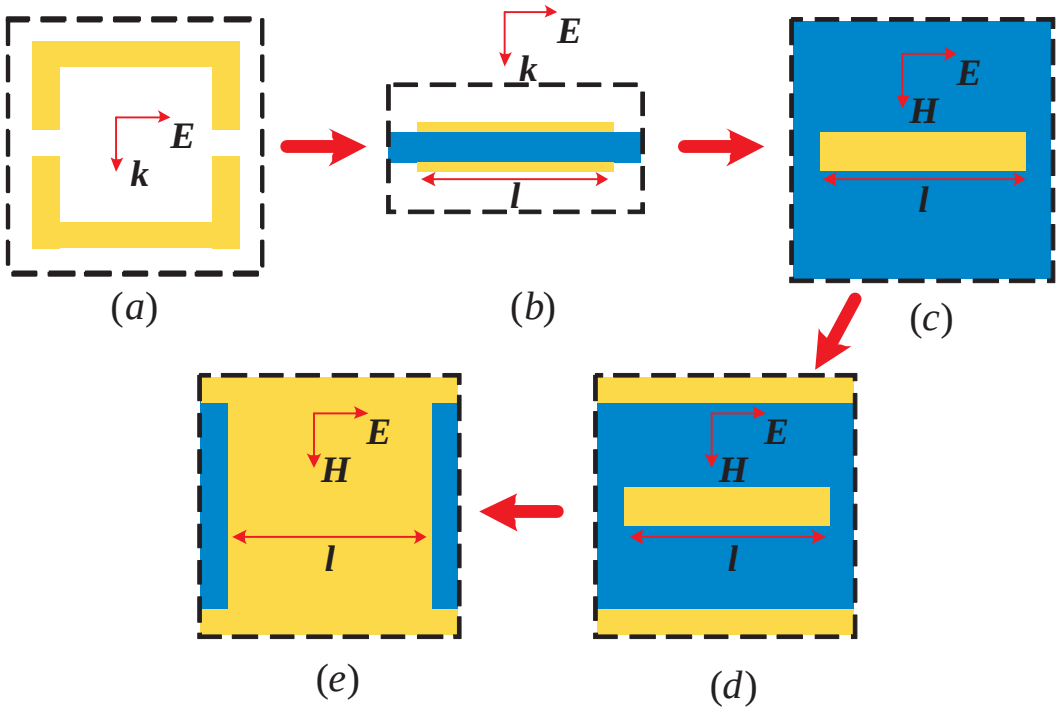

Figure 4.5 (Color online) The two cut single metallic SRR (a) can be transformed to a pair of parallel metallic bars separated by a dielectric (b, view in $(\vec{E}, \vec{k})$ plane; c, view in $(\vec{E}, \vec{H})$ plane). By adding continuous wires, design d (view in $(\vec{E}, \vec{H})$ plane) results, which can be modified to a fully connected one on both sides of the thin dielectric board (e). The dashed square defines the unit cells with dimension a_x (parallel to $\vec{H}$), a_y (parallel to $\vec{E}$) and a_z (parallel to $\vec{k}$).

Starting from a two-gap SRR 4.5(a), we can obtain the fishnet structure by a series of transformations. The short wire pair design shown in Figs 4.5(b,c) has distinct advantages over conventional SRRs. The incident electromagnetic wave is normal to the structure as shown in Fig. 4.5(b), which enables us to build NIMs by only one layer of sample and achieve

relatively strong responses. By adding two long wires as shown in Fig. 4.5(d), we obtained the left-handed materials discussed in the previous section. The last step is to increase the width of the short wires, and connect with the long wires. The resulting structure, shown in Fig. 4.5(d), is the fishnet structure.

4.3 Conclusions

We fabricated a composite LHM working at 13.7 GHz by using short wire pairs and long wires. The transmission and reflection coefficients were measured and showed good consistency with numerical simulations. By using a retrieval procedure, the effective parameters, ϵ, μ, and n, were calculated from measured T and R. This was the first time that a retrieval procedure was completed by using experimental data, which proves the negative refractive index experimentally. In addition, we discussed the relationship between three important LHM designs suitable for the optical regime: double gap SRRs, the short wire pairs, and the fishnet structure.

CHAPTER 5. LOSSES IN THE LEFT-HANDED MEDIUM

Since the original microwave experiments for the demonstration of negative index behavior in the split ring resonators (SRRs) and wires structures, new designs have been introduced, such as the short-wire pairs and the fishnet, that have pushed the existence of the negative refractive index into optical wavelengths [82, 1, 84]. However, both experiment and simulation results show that losses increase as the frequency increases. The transmission loss, $1-T$, at low frequencies [25] is small (of the order of 1-5 dB/λ), while as the frequency increases the loss increases, approaching values of almost 30 dB/λ at infrared frequencies [52]. Another factor to measure loss, namely the figure of merit, is the ratio of real and imaginary parts of the refractive index, $|\mathrm{Re}(n)/\mathrm{Im}(n)|$, drops from the order of 100 for SRRs at microwave frequency to 0.5 for the fishnet structure at optical frequency [49, 57]. So loss becomes a serious problem, which limits the potential applications of metamaterials such as perfect lens [58, 59]. Therefore we need to determine ways to reduce the losses, especially at high frequencies.

5.1 Numerical Simulations

In this chapter, we will study the losses in the fishnet structures through numerical simulations. Our numerical simulations were completed with CST Microwave Studio (Computer Simulation Technology GmbH, Darmstadt, Germany), which uses a finite-integration technique. In Fig. 5.1, we show the structures of the short-wire pairs and the fishnet designs.

The fishnet structure consists of double layer of infinite long metallic wire arrays along two orthogonal directions spaced by a dielectric spacer [47, 50, 51]. The wires along the magnetic field **H** direction act as a magnetic resonator, providing negative permeability μ due to anti-

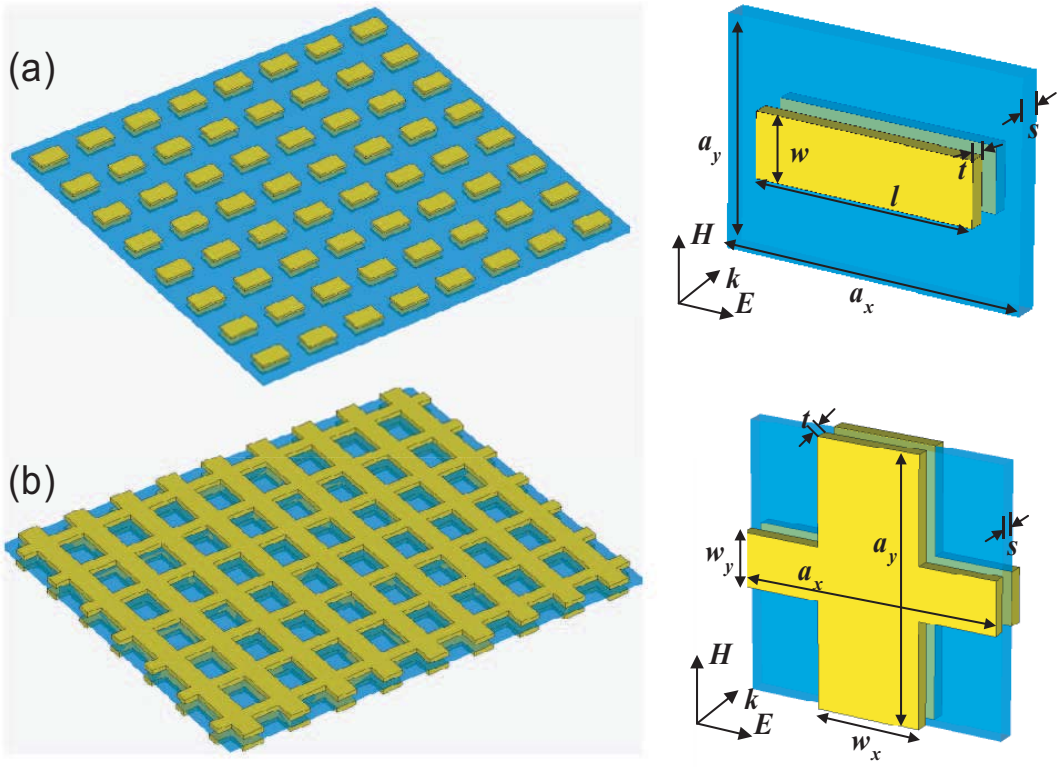

Figure 5.1 Geometries for short-wire pair arrays (a) and the fishnet structure (b). Both consist of a patterned metallic double layer (yellow, usually Au) separated by a thin dielectric (blue).

parallel currents induced by the magnetic field of the incident electromagnetic wave. The wires along the electric field **E** direction of the incident electromagnetic wave excite the plasmonic response and produce negative permittivity ϵ up to the plasma frequency. The fishnet structure has an intrinsic relation with the short-wire pairs [44, 43, 45] and the split ring resonator (SRRs) structure. The short-wire pairs geometry can be viewed as an extreme case of a two-gap SRR ring [46] shrunk along the direction of the gaps. By adding continuous wires, which provide negative permittivity ϵ, one is able to obtain the negative refractive index, n [45]. The fishnet structure can be obtained by increasing the width of the short wires, w, to form continuous wires along the **H** direction and by adding other continuous wires along the **E** direction [50]. The transformation from the two-gap SRR to the short-wire pairs and the fishnet structure has been studied elsewhere [46]. Before we present the results for the fishnet structures, we will present the dependence of the magnetic resonance frequency on the width and its length

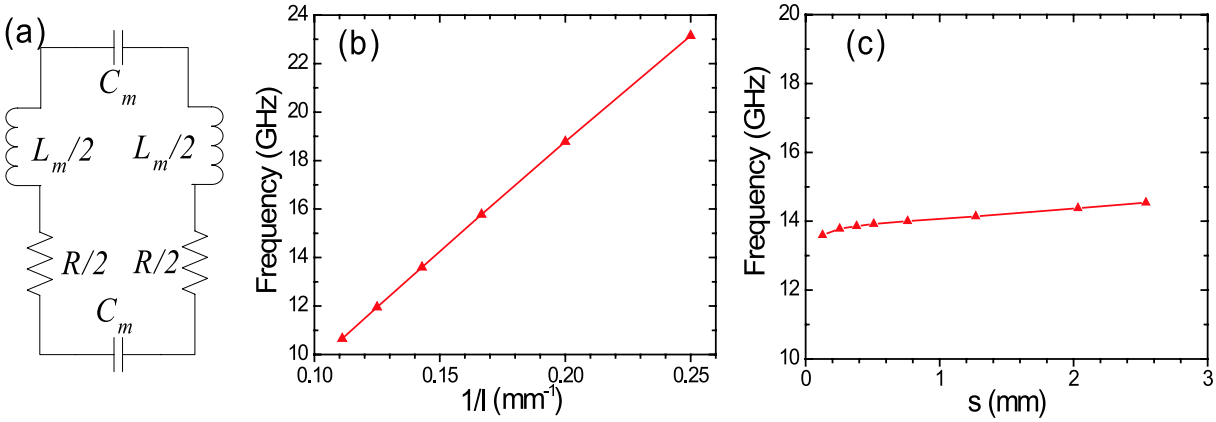

Figure 5.2 (a) An effective RLC circuit of the short-wire pairs structure shown in Fig. 5.1(a). (b) Linear dependence of the magnetic resonance frequency, f_m, on the length of the short-wire l. The other parameters are given by $s = 1.5$ mm, a_x=9.5 mm, a_y=20 mm, ϵ_r=2.53. (c) Dependence of the magnetic resonance frequency, f_m, on the thickness of the dielectric spacer, s. (w=1 mm, l=7 mm, a_x=9.5 mm, a_y=20 mm,ϵ_r=2.53).

of the short-wire pair. The short-wire pairs give a magnetic resonance response [44, 87], and can give a negative μ. The short-wire pairs structure has an interesting property that the resonance frequency, f_m, depends only on the length of the short-wire, l, among the geometric parameters, l, s, w and t. As shown in Fig. 5.2(b), the resonance frequency f_m, is a linear function of $1/l$, over a large range of l. On the other hand, we barely observe any change of f_m with the other parameters, s, w and t. Figure 5.2(c) shows the magnetic resonance frequencies f_m as the separation s increases from 0.2 mm to 2.6 mm. One can see that although s increases by a factor of 13, f_m only changes around 5% (from 13.6 to 14.54 GHz). This is due to the fact that the capacitance, $C_m = \epsilon_r(l \cdot w)/2s$, and the inductance, $L_m = \mu_r(l \cdot s)/w$, have the opposite dependence on the width, w, and separation between the two short-wire pairs, s (s is also the thickness of the dielectric spacer) as shown in Fig. 5.1(a). The total capacitance of the series RLC circuit is given by $C = \frac{1}{2}C_m$ and the total inductance is $L = L_m$, so the resonance frequency is given by $\omega_m = 1/\sqrt{LC} = 2c_0/l\sqrt{\epsilon_r\mu_r}$, where c_0 is the speed of light in the vacuum and ϵ_r and μ_r are the dielectric function and relative permeability of the dielectric spacer, respectively [46]. As a transformation of the short-wire pairs structure, the fishnet structure has the same property, i.e., the resonance frequency f_m does not depend on the separation, s.

This property gives us the opportunity to change L and C simultaneously without affecting the resonance frequency by changing the separation, s. The short-wire pairs structure does not give a negative n, but they give a negative μ, all the way to the optical wavelengths [44, 87]. We will concentrate all of our efforts in trying to reduce the losses in the fishnet design, which is the best design so far, for giving a negative n at the optical frequencies [49, 88].

5.2 Losses and the Effective Inductance L

The magnetic element of the fishnet structure (i.e. the long wires along the **H** direction), can be modeled as the same series RLC circuit as the short-wire pairs shown in Fig. 5.2(a). As we know, the loss of the RLC circuit depends upon the value of each circuit element and the quality factor, Q, is given by $Q = \frac{1}{2R}\sqrt{\frac{L}{C}}$. By increasing the inductance L or reducing the resistance R and capacitance C, we are able to increase the Q-factor and therefore reduce losses. The resistance of the metallic structure depends on the conductivity and the frequency because of the skin effect, so we can choose a good conductor such as copper, silver or gold to reduce the resistance [89]. The inductance, L, and the capacitance C, strongly depend on the geometric parameters of the structure and are relatively easy to be changed by modifying these parameters.

In the fishnet structure, the long wire along the **H** direction is like a magnetic resonator, which provides the negative μ by introducing a magnetic resonance over a finite frequency band. The magnetic permeability is given by as the following

$$\mu = 1 - \frac{A\omega^2}{\omega^2 - \omega_m^2 + \mathrm{i}\omega\Gamma_m} \tag{5.1}$$

where ω_m is the magnetic resonance frequency and Γ_m is the damping factor, which is inversely proportional to the effective inductance [90],

$$\Gamma_m \propto \frac{R}{L} \tag{5.2}$$

So we are able to reduce the loss by increasing the inductance of the structure.

There is a special reason for choosing the fishnet structure in our study of the losses. Since the loss increases as the magnetic resonance frequency increases [1, 84, 52], we must

compare the loss of metamaterials with different geometric parameters at the same resonance frequency. Because the fishnet structure has an intrinsic relation with the short-wire pairs, the magnetic resonance frequency f_m does not change with the thickness of the dielectric spacer, s. By increasing s, the effective inductance L will increase linearly with s, while the effective C decreases simultaneously with s and the product LC does not change, therefore, we are able to compare the losses at a fixed frequency. We first studied the reduction of losses

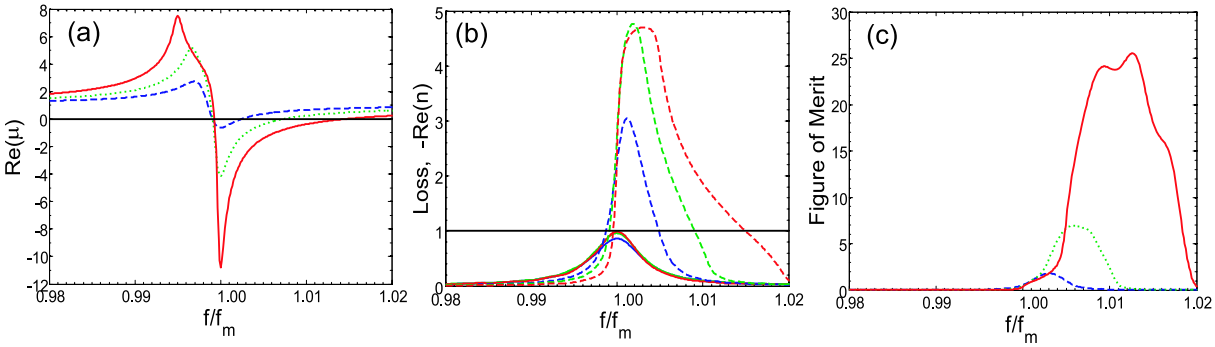

Figure 5.3 (a) Effective permeability for the fishnet structure for three different widths of the dielectric spacer, s=0.25 (blue dashed), 0.5 (green dotted) and 1.0 mm (red solid), respectively. The frequency f is normalized by the magnetic resonance frequency f_m (f_m =9.701, 9.689 and 9.604 GHz for s=0.25, 0.5 and 1.0 mm, respectively). (b) The normalized loss, $(1-R-T)/(1-R)$ (solid) , and the real part of refractive index, $-\mathrm{Re}(n)$ (dashed), as a function of the normalized frequency. (c) Figure of Merit, $|\mathrm{Re}(n)/\mathrm{Im}(n)|$, versus f/f_m.

for the fishnet structure at microwave frequencies. In Fig. 5.3(a) we present the effective permeability μ as a function of the normalized frequency. One can see that the magnitude of the magnetic resonance is significantly increased as the width of the dielectric spacer s increases. Fig. 5.3(b) shows the real part of the effective refractive index, $-\mathrm{Re}(n)$, calculated from numerical simulations employing a retrieval procedure [28, 91], and the normalized losses, defined as the ratio of $(1-R-T)/(1-R)$, where T and R are the transmittance and reflectance, respectively. One can see that, as the separation s increases from 0.25 to 1.0 mm, the frequency with a given value of $\mathrm{Re}(n)$=-1, shifts away from the center of the peak of the normalized loss. The underlying reason for this is the magnet resonance are becoming stronger as the inductance L increases, so that the frequency with a given value of $\mathrm{Re}(n)$=-1 moves away

from the resonance peak where high loss occurs. Figure 5.3(c) shows that the figure of merit (FOM), which is defined as $|\mathrm{Re}(n)/\mathrm{Im}(n)|$ and increases dramatically from 2 to 25. Further investigations show that an optimized fishnet structure at GHz frequencies can have a FOM in the order of 50. However, according to our simulations, the SRRs type metamaterial usually has a FOM larger than 100, due to the large effective inductance to effective capacitance ratio, L/C. It is very difficult to fabricate and characterize the SRRs at optical frequencies[1, 92], so we are forced to use the fishnet design, which gives $n < 0$ for perpendicular propagation.

Another way to increase the inductance, L, is to increase the relative permeability, μ_r, of the dielectric spacer. In order to keep the resonance frequency unchanged, we must decrease the dielectric constant, ϵ_r, of the spacer accordingly, i.e., to keep $\mu_r\epsilon_r$ as a constant. The magnitude of the magnetic resonance will increase dramatically as μ_r increases. In order to avoid the periodicity effects [41, 33] due to the strong magnetic resonance, we limited the range of μ_r to less than 2 and used a lossy material as the dielectric spacer with loss tangent, $\tan\delta = 1.5 \times 10^{-3}$. Figure 5.4(a) shows effective permeability, μ, as the permeability of the spacer μ_r changes from 1 to 2. One can see from Fig. 5.4(a) that the magnitude of the magnetic resonance increases by a factor of 2. In Fig. 5.4(b), the value of the real part of the refractive index, $\mathrm{Re}(n)$, increases and moves away from the center of the loss peak. The figure of merit, shown in Fig. 5.4(c), also increases by a factor of 2 and has a maximum value of 6.

We also examined the losses of the fishnet structure in the infrared and the optical regimes. Similar to the microwave frequency, the magnetic resonance become stronger as the separation, s, increases from 30 to 90 nm as shown in Fig. 5.5(a). Figure 5.5(b) shows the effective refractive index $\mathrm{Re}(n)$ versus the frequency at THz region. Notice that $n < 0$ at 370 THz, which is in the optical regime. In Fig. 5.5(c), one can see that the figure of merit increases from 4.2 to 10.0 (peak value) as the separation, s, changes from 30 to 90 nm. At frequencies above 100 THz, the losses of the fishnet structure increase rapidly as the resonance frequency increases [49, 47, 56]. In our simulations, we manage to achieve a FOM=2.5 at 620 THz (λ=484 nm) using silver (The permittivity of silver is described by the Drude model with the plasma frequency, f_p=2181 THz, and the damping frequency, f_c=14.4 THz, which is 3.3 times the

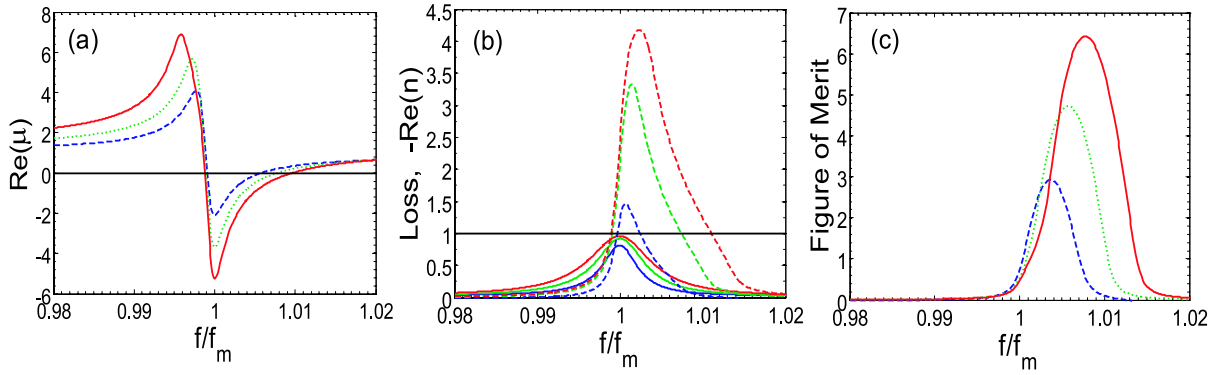

Figure 5.4 (a) Effective permeability for the fishnet structure with permeability of the dielectric spacer μ_r=1.0 (blue dashed), 1.4 (green dotted) and 2.0 (red solid), respectively. The dielectric constant is $\epsilon_r = 20/\mu_r$. The frequency f is normalized by the resonance frequency f_m (f_m =2.323, 2.325 and 2.330 GHz for μ_r=1.0, 1.4 and 2.0, respectively). (b) The normalized loss and the real part of refractive index (dashed). (c) Figure of Merit.

damping frequency of the bulk material to take into account the high loss in the thin layer of silver.) As a comparison, the best results so far in the optical regime, is FOM=0.5 at λ=784 nm [49]. So, our new fishnet design has reduced the losses and increased substantially the figure of merit.

It is worth to point out that one can not increase s in the fishnet design arbitrarily. The maximum value of s is limited by two facts. First, it is restricted by the unit cell size, a_z, in the propagating direction. The unit cell size, a_z, is limited by the homogenous assumption of left-handed materials, i.e. $a_z \ll \lambda$, and also by the requirement of negative permittivity, which is provided by the long wires along the electric field direction and will be diluted by a large unit cell. Second, according to our simulations, as s increases up to a certain value larger than the width of wires, w, the magnetic resonance will disappear. This is due to the fact that the short wires are decoupled from each other as $s \gg w$.

5.3 Conclusions

In summary, we proposed a simple and efficient way to reduce losses in the left-handed metamaterial designs by increasing the inductance to the capacitance ratio, L/C. We found

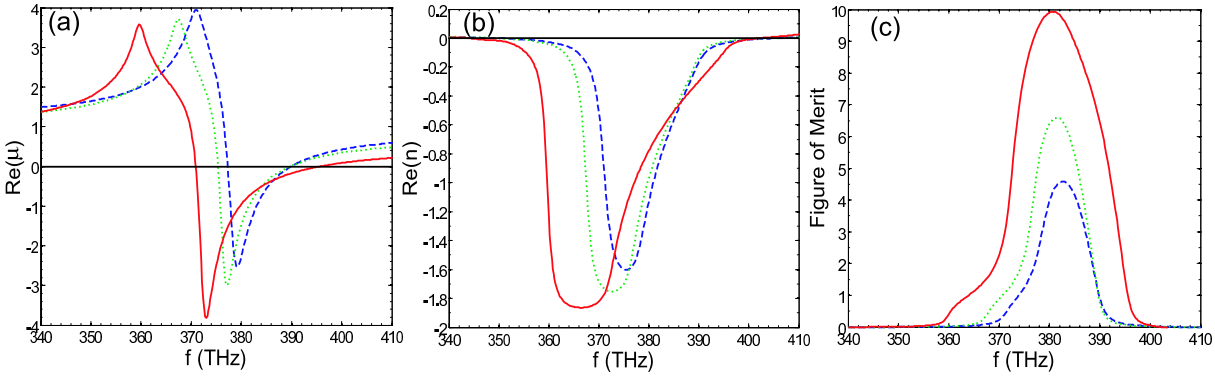

Figure 5.5 (a) Effective permeability for the fishnet structure for three different widths of the dielectric spacers, s=30 (blue dashed), 60 (green dotted), and 90 nm (red solid), respectively The other parameters are given by w_x = 100 nm, w_y=200 nm, a_x=a_y=300 nm, t=40 nm, ϵ_r=1.90. (b) The real part of refractive index (dashed). (c) Figure of Merit.

that the figure of merit of the fishnet structure can be as large as 50 at microwave frequencies. Our method is also valid in the infrared and in the optical regime, we should be able to obtain a figure of merit of 2.5 at λ=484 nm, which improved the figure of merit by a factor of 5, comparing with the best result at λ=784 nm so far. Although our approach is presented using the fishnet structure, it's a generic method and can also apply to other type left-handed material designs such as SRRs.

APPENDIX PHASE VELOCITY, GROUP VELOCITY, AND ENERGY VELOCITY IN LHM

Following the same definition as in right-handed materials, the phase velocity in left-handed materials is given by

$$\mathbf{v}_p = \frac{\omega}{|\mathbf{k}|}\hat{\mathbf{k}} = \frac{c_0}{|n|}\hat{\mathbf{k}}, \tag{A.3}$$

where $\hat{\mathbf{k}} = \mathbf{k}/|\mathbf{k}|$ is the unit vector along $\mathbf{k}$ direction. The group velocity is defined as

$$\mathbf{v}_g = \nabla_k \omega = \frac{\mathrm{d}\omega}{\mathrm{d}|\mathbf{k}|}\hat{\mathbf{k}}, \tag{A.4}$$

Using the dispersion relation $\mathbf{k} = \frac{\omega}{c_0}|n|\hat{\mathbf{k}}$, one can obtain

$$\mathbf{v}_g = \frac{c_0/|n|}{1 + \frac{\omega}{n}\frac{\mathrm{d}n}{\mathrm{d}\omega}}\hat{\mathbf{k}} = \frac{\mathbf{v}_p}{\alpha}. \tag{A.5}$$

Where $\alpha = 1 + \frac{\omega}{n}\frac{\mathrm{d}n}{\mathrm{d}\omega}$. Next, we will prove that α has the same sign as n.

$$\begin{aligned} \alpha &= 1 + \frac{\omega}{n}\frac{\mathrm{d}n}{\mathrm{d}\omega} = 1 + \frac{\mathrm{d}\ln|n|}{\mathrm{d}\ln\omega} \\ &= \frac{1}{2}\left(1 + \frac{\mathrm{d}\ln|\epsilon|}{\mathrm{d}\ln\omega}\right) + \frac{1}{2}\left(1 + \frac{\mathrm{d}\ln|\mu|}{\mathrm{d}\ln\omega}\right) \\ &= \frac{1}{2}\left(1 + \frac{\omega}{\epsilon}\frac{\mathrm{d}\epsilon}{\mathrm{d}\omega}\right) + \frac{1}{2}\left(1 + \frac{\omega}{\mu}\frac{\mathrm{d}\mu}{\mathrm{d}\omega}\right) \end{aligned} \tag{A.6}$$

Using inequality in Equation. 1.8, one can easily show that,

$$\begin{aligned} 1 + \frac{\omega}{\epsilon}\frac{\mathrm{d}\epsilon}{\mathrm{d}\omega} > 0, \quad 1 + \frac{\omega}{\mu}\frac{\mathrm{d}\mu}{\mathrm{d}\omega} > 0 \qquad \text{for} \qquad \epsilon > 0,\, \mu > 0 \\ 1 + \frac{\omega}{\epsilon}\frac{\mathrm{d}\epsilon}{\mathrm{d}\omega} < 0, \quad 1 + \frac{\omega}{\mu}\frac{\mathrm{d}\mu}{\mathrm{d}\omega} < 0 \qquad \text{for} \qquad \epsilon < 0,\, \mu < 0 \end{aligned}$$

and thus, one can get,

$$\begin{aligned} \alpha > 0 \qquad \text{for} \qquad \epsilon > 0,\, \mu > 0 \\ \alpha < 0 \qquad \text{for} \qquad \epsilon < 0,\, \mu < 0 \end{aligned} \tag{A.7}$$

So we have proven that α has the same sign as n does. Equation. A.7 and Equation. A.7 imply that the phase velocity, $\mathbf{v}_p$, and the group velocity, $\mathbf{v}_g$, are parallel in the right-handed medium and are anti-parallel in the left-handed medium.

The energy velocity is given by $\mathbf{v}_e = \bar{\mathbf{S}}/\bar{w}$ [13], where $\bar{\mathbf{S}}$ and $\bar{w}$ are the time average poynting vector and time average power density, respectively.

$$\begin{aligned}
\bar{\mathbf{S}} &= \frac{1}{2}\mathrm{Re}(E \times H^*) = \frac{|E_0|^2}{2\eta}\frac{n}{|n|}\hat{\mathbf{k}} \\
\bar{w} &= \frac{1}{4}\left[\frac{\mathrm{d}(\epsilon\omega)}{\mathrm{d}\omega}|E_0|^2 + \frac{\mathrm{d}(\mu\omega)}{\mathrm{d}\omega}|H_0|^2\right] \\
&= \frac{1}{4}|E_0|^2\left[\frac{\mathrm{d}(\epsilon\omega)}{\mathrm{d}\omega} + \frac{1}{\eta^2}\frac{\mathrm{d}(\mu\omega)}{\mathrm{d}\omega}\right]
\end{aligned}$$

therefore, the energy velocity is given by,

$$\begin{aligned}
\mathbf{v}_e &= \frac{\bar{\mathbf{S}}}{\bar{w}} = \frac{n}{|n|}\frac{2}{\epsilon\eta\left(1+\frac{\omega}{\epsilon}\frac{\mathrm{d}\epsilon}{\mathrm{d}\omega}\right) + \frac{\mu}{\eta}\left(1+\frac{\omega}{\mu}\frac{\mathrm{d}\mu}{\mathrm{d}\omega}\right)}\hat{\mathbf{k}} \\
&= \frac{n}{|n|}\frac{1}{\frac{1}{2}\frac{n}{c_0}\left(1+\frac{\omega}{\epsilon}\frac{\mathrm{d}\epsilon}{\mathrm{d}\omega}\right) + \frac{1}{2}\frac{n}{c_0}\left(1+\frac{\omega}{\mu}\frac{\mathrm{d}\mu}{\mathrm{d}\omega}\right)}\hat{\mathbf{k}} \\
&= \frac{c_0\hat{\mathbf{k}}}{|n|}\frac{1}{1+\frac{\mathrm{d}\ln|n|}{\mathrm{d}\ln\omega}} \\
&= \frac{\mathbf{v}_p}{\alpha}
\end{aligned} \tag{A.8}$$

Comparing equation A.5 to A.8, on immediately see that the energy velocity, $\mathbf{v}_e$, is same as the group velocity, $\mathbf{v}_g$. In a right handed medium, where $\alpha > 0$, $\mathbf{v}_g$ and $\mathbf{v}_e$ are in the same direction as $\mathbf{v}_p$ while in a left handed medium, where $\alpha < 0$, $\mathbf{v}_g$ and $\mathbf{v}_e$ are in the opposite direction of $\mathbf{v}_p$.

BIBLIOGRAPHY

[1] C. M. Soukoulis, S. Linden, and M. Wegener, "Negative refractive index at optical wavelengths," *Science*, vol. 315, no. 5808, pp. 47–49, 2007.

[2] V. G. Veselago, "Experimental demonstration of negative index of refraction," *Sov. Phys. Usp.*, vol. 10, p. 509, 1968.

[3] J. Pendry, A. Holden, W. Stewart, and I. Youngs, "Extremely low frequency plasmons in metallic mesostructures," *Physical Review Letters*, vol. 76, p. 4773, Jun 1996.

[4] J. Pendry, A. Holden, D. Robbins, and W. Stewart, "Magnetism from conductors and enhanced nonlinear phenomena," *IEEE Trans. Microwave Theroy Tech.*, vol. 47, p. 2075, Nov 1999.

[5] D. Smith, W. Padilla, D. Vier, S. Nemat-Nasser, and S. Schultz, "Composite medium with simultaneously negative permeability and permittivity," *Physical Review Letters*, vol. 84, p. 4184, May 2000.

[6] R. A. Shelby, D. R. Smith, and S. Schultz, "Experimental verification of a negative index of refraction," *Science*, vol. 292, pp. 77–79, Apr 2001.

[7] L. D. Landau, E. M. Lifshitz, and L. P. Pitaevskii, *Electrodynamics of Continuous Media*. Linacre House, Jordan Hill, Oxford, UK: Butterworth Heinemann, 1984.

[8] J. D. Jackson, *Classical Electrodynamics*. John Wiley, third ed., 1998.

[9] M. I. Stockman, "Criterion for negative refraction with low optical losses from a fundamental principle of causality," *Physical Review Letters*, vol. 98, no. 17, p. 177404, 2007.

[10] M. I. Stockman, "Stockman replies:," *Physical Review Letters*, vol. 99, no. 18, p. 189702, 2007.

[11] S. Foteinopoulou, E. N. Economou, and C. M. Soukoulis, "Refraction in media with a negative refractive index," *Physical Review Letters*, vol. 90, no. 10, p. 107402, 2003.

[12] A. L. Pokrovsky and A. L. Efros, "Sign of refractive index and group velocity in lefthanded media (vol 124, pg 283, 2002)," *Solid State Comm.*, vol. 125, no. 9, pp. 515–515, 2003.

[13] C. A. Balanis, *Advanced Engineering Electromagnetics*. John Wiley & Sons, 1989.

[14] R. A. Shelby, D. R. Smith, S. C. Nemat-Nasser, and S. Schultz, "Microwave transmission through a two-dimensional, isotropic, left-handed metamaterial," *Applied Physics Letters*, vol. 78, no. 4, pp. 489–491, 2001.

[15] M. Bayindir, K. Aydin, E. Ozbay, P. Markos, and C. M. Soukoulis, "Transmission properties of composite metamaterials in free space," *Applied Physics Letters*, vol. 81, no. 1, pp. 120–122, 2002.

[16] K. Li, S. J. McLean, R. B. Greegor, C. G. Parazzoli, and M. H. Tanielian, "Free-space focused-beam characterization of left-handed materials," *Applied Physics Letters*, vol. 82, no. 15, pp. 2535–2537, 2003.

[17] C. G. Parazzoli, R. B. Greegor, K. Li, B. E. C. Koltenbah, and M. Tanielian, "Experimental verification and simulation of negative index of refraction using snell's law," *Physical Review Letters*, vol. 90, no. 10, p. 107401, 2003.

[18] R. B. Greegor, C. G. Parazzoli, K. Li, B. E. C. Koltenbah, and M. Tanielian, "Experimental determination and numerical simulation of the properties of negative index of refraction materials," *Optics Express*, vol. 11, no. 7, pp. 688–695, 2003.

[19] R. Marques, J. Martel, F. Mesa, and F. Medina, "A new 2D isotropic left-handed metamaterial design: Theory and experiment," *Microwave Opt. Technology Lett.*, vol. 35, no. 5, pp. 405–408, 2002.

[20] J. T. Huangfu, L. X. Ran, H. S. Chen, X. M. Zhang, K. S. Chen, T. M. Grzegorczyk, and J. A. Kong, "Experimental confirmation of negative refractive index of a metamaterial composed of Omega-like metallic patterns," *Appl. Phys. Lett.*, vol. 84, no. 9, pp. 1537–1539, 2004.

[21] A. A. Houck, J. B. Brock, and I. L. Chuang, "Experimental observations of a left-handed material that obeys snell's law," *Physical Review Letters*, vol. 90, no. 13, p. 137401, 2003.

[22] L. Ran, J. Huangfu, H. Chen, Y. Li, X. Zhang, K. Chen, and J. A. Kong, "Microwave solid-state left-handed material with a broad bandwidth and an ultralow loss," *Physical Review B (Condensed Matter and Materials Physics)*, vol. 70, no. 7, p. 073102, 2004.

[23] A. F. Starr, P. M. Rye, D. R. Smith, and S. Nemat-Nasser, "Fabrication and characterization of a negative-refractive-index composite metamaterial," *Physical Review B (Condensed Matter and Materials Physics)*, vol. 70, no. 11, p. 113102, 2004.

[24] H. S. Chen, L. X. Ran, J. T. Huangfu, X. M. Zhang, K. S. Chen, T. M. Grzegorczyk, and J. A. Kong, "T-junction waveguide experiment to characterize left-handed properties of metamaterials," *J. Appl. Phys.*, vol. 94, no. 6, pp. 3712–3716, 2003.

[25] K. Aydin, K. Guven, M. Kafesaki, L. Zhang, C. M. Soukoulis, and E. Ozbay, "Experimental observation of true left-handed transmission peaks in metamaterials," *Optics Letters*, vol. 29, pp. 2623–2625, Nov 2004.

[26] C. G. Parazzoli, R. B. Greegor, K. Li, B. E. C. Koltenbah, and M. Tanielian, "Experimental verification and simulation of negative index of refraction using snell's law," *Phys. Rev. Lett.*, vol. 90, p. 107401, Mar 2003.

[27] T. Koschny, M. Kafesaki, E. N. Economou, and C. M. Soukoulis, "Effective medium theory of left-handed materials," *Physical Review Letters*, vol. 93, no. 10, 2004.

[28] D. R. Smith, S. Schultz, P. Markos, and C. M. Soukoulis, "Determination of effective permittivity and permeability of metamaterials from reflection and transmission coefficients,"

Physical Review B (Condensed Matter and Materials Physics), vol. 65, no. 19, p. 195104, 2002.

[29] S. O'Brien and J. B. Pendry, "Magnetic activity at infrared frequencies in structured metallic photonic crystals," *J. Physics-condensed Matter*, vol. 14, no. 25, pp. 6383–6394, 2002.

[30] X. D. Chen, T. M. Grzegorczyk, B. I. Wu, J. Pacheco, and J. A. Kong, "Robust method to retrieve the constitutive effective parameters of metamaterials," *Physical Review E*, vol. 70, no. 1, p. 016608, 2004.

[31] P. Markos and C. M. Soukoulis, "Transmission properties and effective electromagnetic parameters of double negative metamaterials," *Optics Express*, vol. 11, no. 7, pp. 649–661, 2003.

[32] T. Koschny, P. Markos, D. R. Smith, and C. M. Soukoulis, "Resonant and antiresonant frequency dependence of the effective parameters of metamaterials," *Physical Review E*, vol. 68, no. 6, p. 065602, 2003.

[33] T. Koschny, P. Markos, E. N. Economou, D. R. Smith, D. C. Vier, and C. M. Soukoulis, "Impact of inherent periodic structure on effective medium description of left-handed and related metamaterials," *Physical Review B (Condensed Matter and Materials Physics)*, vol. 71, no. 24, p. 245105, 2005.

[34] D. R. Smith, D. C. Vier, T. Koschny, and C. M. Soukoulis, "Electromagnetic parameter retrieval from inhomogeneous metamaterials," *Physical Review E*, vol. 71, no. 3, p. 036617, 2005.

[35] X. Chen, B.-I. Wu, J. A. Kong, and T. M. Grzegorczyk, "Retrieval of the effective constitutive parameters of bianisotropic metamaterials," *Physical Review E (Statistical, Nonlinear, and Soft Matter Physics)*, vol. 71, no. 4, p. 046610, 2005.

[36] T. J. Yen, W. J. Padilla, N. Fang, D. C. Vier, D. R. Smith, J. B. Pendry, D. N. Basov, and X. Zhang, "Terahertz magnetic response from artificial materials," *Science*, vol. 303, pp. 1494–1496, Mar 2004.

[37] N. Katsarakis, G. Konstantinidis, A. Kostopoulos, R. Penciu, T. Gundogdu, M. Kafesaki, E. Economou, T. Koschny, and C. M. Soukoulis, "Magnetic response of split-ring resonators in the far-infrared frequency regime," *Optics Letters*, vol. 30, pp. 1348–1350, Jun 2005.

[38] S. Linden, C. Enkrich, M. Wegener, J. F. Zhou, T. Koschny, and C. M. Soukoulis, "Magnetic response of metamaterials at 100 terahertz," *Science*, vol. 306, pp. 1351–1353, Nov 2004.

[39] C. Enkrich, M. Wegener, S. Linden, S. Burger, L. Zschiedrich, F. Schmidt, J. F. Zhou, T. Koschny, and C. M. Soukoulis, "Magnetic metamaterials at telecommunication and visible frequencies," *Physical Review Letters*, vol. 95, no. 20, p. 203901, 2005.

[40] N. Katsarakis, T. Koschny, M. Kafesaki, E. N. Economou, and C. M. Soukoulis, "Electric coupling to the magnetic resonance of split ring resonators," *Applied Physics Letters*, vol. 84, no. 15, pp. 2943–2945, 2004.

[41] J. F. Zhou, T. Koschny, M. Kafesaki, E. N. Economou, J. B. Pendry, and C. M. Soukoulis, "Saturation of the magnetic response of split-ring resonators at optical frequencies," *Physical Review Letters*, vol. 95, no. 22, p. 223902, 2005.

[42] M. W. Klein, C. Enkrich, M. Wegener, C. M. Soukoulis, and S. Linden, "Single-slit split-ring resonators at optical frequencies: limits of size scaling," *Optics Letters*, vol. 31, no. 9, pp. 1259–1261, 2006.

[43] V. M. Shalaev, W. S. Cai, U. K. Chettiar, H. K. Yuan, A. K. Sarychev, V. P. Drachev, and A. V. Kildishev, "Negative index of refraction in optical metamaterials," *Optics Letters*, vol. 30, pp. 3356–3358, Dec 2005.

[44] G. Dolling, C. Enkrich, M. Wegener, J. F. Zhou, and C. M. Soukoulis, "Cut-wire pairs and plate pairs as magnetic atoms for optical metamaterials," *Optics Letters*, vol. 30, pp. 3198–3200, Dec 2005.

[45] J. F. Zhou, L. Zhang, G. Tuttle, T. Koschny, and C. M. Soukoulis, "Negative index materials using simple short wire pairs," *Physical Review B (Condensed Matter and Materials Physics)*, vol. 73, no. 4, p. 041101, 2006.

[46] J. Zhou, E. N. Economon, T. Koschny, and C. M. Soukoulis, "Unifying approach to left-handed material design," *Opt. Lett.*, vol. 31, no. 24, pp. 3620–3622, 2006.

[47] G. Dolling, C. Enkrich, M. Wegener, C. M. Soukoulis, and S. Linden, "Simultaneous negative phase and group velocity of light in a metamaterial," *Science*, vol. 312, p. 892, may 2006.

[48] S. Zhang, W. Fan, N. C. Panoiu, K. J. Malloy, R. M. Osgood, and S. R. J. Brueck, "Experimental demonstration of near-infrared negative-index metamaterials," *Physical Review Letters*, vol. 95, no. 13, p. 137404, 2005.

[49] G. Dolling, M. Wegener, C. M. Soukoulis, and S. Linden, "Negative-index metamaterial at 780 nm wavelength," *Optics Letters*, vol. 32, no. 1, pp. 53–55, 2007.

[50] M. Kafesaki, I. Tsiapa, N. Katsarakis, T. Koschny, C. M. Soukoulis, and E. N. Economou, "Left-handed metamaterials: The fishnet structure and its variations," *Physical Review B (Condensed Matter and Materials Physics)*, vol. 75, no. 23, p. 235114, 2007.

[51] N. Katsarakis, M. Kafesaki, I. Tsiapa, E. N. Economou, and C. M. Soukoulis, "High transmittance left-handed materials involving symmetric split-ring resonators," *Photon. and Nanostruct.: Fundam. and Appl.*, vol. 5, p. 149, 2007.

[52] C. M. Soukoulis, J. Zhou, T. Koschny, M. Kafesaki, and E. N. Economou, "The science of negative index materials," *Journal of Physics: Condensed Matter*, vol. 20, no. 30, p. 304217, 2008.

[53] R. B. Greegor, C. G. Parazzoli, K. Li, and M. H. Tanielian, "Origin of dissipative losses in negative index of refraction materials," *Applied Physics Letters*, vol. 82, no. 14, pp. 2356–2358, 2003.

[54] J. F. Zhou, T. Koschny, L. Zhang, G. Tuttle, and C. M. Soukoulis, "Experimental demonstration of negative index of refraction," *Applied Physics Letters*, vol. 88, no. 22, p. 221103, 2006.

[55] M. Gokkavas, K. Guven, I. Bulu, K. Aydin, R. S. Penciu, M. Kafesaki, C. M. Soukoulis, and E. Ozbay, "Experimental demonstration of a left-handed metamaterial operating at 100 ghz," *Physical Review B (Condensed Matter and Materials Physics)*, vol. 73, no. 19, p. 193103, 2006.

[56] G. Dolling, C. Enkrich, M. Wegener, C. M. Soukoulis, and S. Linden, "Low-loss negative-index metamaterial at telecommunication wavelengths," *Optics Letters*, vol. 31, pp. 1800–1802, Jun 2006.

[57] U. K. Chettiar, A. V. Kildishev, H. K. Yuan, W. Cai, S. Xiao, V. P. Drachev, and V. M. Shalaev, "Dual-band negative index metamaterial: double negative at 813 nm and single negative at 772 nm," *Optics Letters*, vol. 32, pp. 1671–1673, June 2007.

[58] J. B. Pendry, "Negative refraction makes a perfect lens," *Physical Review Letters*, vol. 85, no. 18, pp. 3966–3969, 2000.

[59] J. B. Pendry and D. R. Smith, "The quest for the superlens," *Scientific American*, vol. 295, no. 1, pp. 60–67, 2006.

[60] J. Zhou, T. Koschny, and C. M. Soukoulis, "An efficient way to reduce losses of left-handed metamaterials," *Opt. Express*, vol. 16, no. 15, pp. 11147–11152, 2008.

[61] A. K. Popov and V. M. Shalaev, "Compensating losses in negative-index metamaterials by optical parametric amplification," *Opt. Lett.*, vol. 31, no. 14, pp. 2169–2171, 2006.

[62] A. D. Boardman, Y. G. Rapoport, N. King, and V. N. Malnev, "Creating stable gain in active metamaterials," *J. Opt. Soc. Am. B-optical Phys.*, vol. 24, no. 10, pp. A53–A61, 2007.

[63] S. Tretyakov, I. Nefedov, A. Sihvola, S. Maslovski, and C. Simovski, "Waves and energy in chiral nihility," *J. Electromagnetic Waves Applications*, vol. 17, no. 5, pp. 695–706, 2003.

[64] J. B. Pendry, "A Chiral Route to Negative Refraction," *Science*, vol. 306, no. 5700, pp. 1353–1355, 2004.

[65] S. Tretyakov, A. Sitivola, and L. Jylha, "Backward-wave regime and negative refraction in chiral composites," *Photonics Nanostructures-fundamentals Applications*, vol. 3, no. 2-3, pp. 107–115, 2005.

[66] Y. Jin and S. He, "Focusing by a slab of chiral medium," *Opt. Express*, vol. 13, no. 13, pp. 4974–4979, 2005.

[67] C. Monzon and D. W. Forester, "Negative refraction and focusing of circularly polarized waves in optically active media," *Physical Review Letters*, vol. 95, no. 12, p. 123904, 2005.

[68] A. V. Rogacheva, V. A. Fedotov, A. S. Schwanecke, and N. I. Zheludev, "Giant gyrotropy due to electromagnetic-field coupling in a bilayered chiral structure," *Physical Review Letters*, vol. 97, no. 17, p. 177401, 2006.

[69] E. Plum, V. A. Fedotov, A. S. Schwanecke, N. I. Zheludev, and Y. Chen, "Giant optical gyrotropy due to electromagnetic coupling," *Applied Physics Letters*, vol. 90, no. 22, p. 223113, 2007.

[70] T. Vallius, K. Jefimovs, J. Turunen, P. Vahimaa, and Y. Svirko, "Optical activity in subwavelength-period arrays of chiral metallic particles," *Applied Physics Letters*, vol. 83, no. 2, pp. 234–236, 2003.

[71] M. Decker, M. W. Klein, M. Wegener, and S. Linden, "Circular dichroism of planar chiral magnetic metamaterials," *Opt. Lett.*, vol. 32, no. 7, pp. 856–858, 2007.

[72] Y. Svirko, N. Zheludev, and M. Osipov, "Layered chiral metallic microstructures with inductive coupling," *Applied Physics Letters*, vol. 78, no. 4, pp. 498–500, 2001.

[73] V. A. Fedotov, P. L. Mladyonov, S. L. Prosvirnin, A. V. Rogacheva, Y. Chen, and N. I. Zheludev, "Asymmetric propagation of electromagnetic waves through a planar chiral structure," *Physical Review Letters*, vol. 97, no. 16, p. 167401, 2006.

[74] B. Bai, Y. Svirko, J. Turunen, and T. Vallius, "Optical activity in planar chiral metamaterials: Theoretical study," *Physical Review A (Atomic, Molecular, and Optical Physics)*, vol. 76, no. 2, p. 023811, 2007.

[75] M. Thiel, G. von Freymann, and M. Wegener, "Layer-by-layer three-dimensional chiral photonic crystals," *Opt. Lett.*, vol. 32, no. 17, pp. 2547–2549, 2007.

[76] L. Jelinek, R. Marqués, F. Mesa, and J. D. Baena, "Periodic arrangements of chiral scatterers providing negative refractive index bi-isotropic media," *Physical Review B (Condensed Matter and Materials Physics)*, vol. 77, no. 20, p. 205110, 2008.

[77] J. A. Kong, *Electromagnetic Wave Theory*. Cambridge, 2000.

[78] C. Monzon, "Radiation and scattering in "homogeneous general biisotropic regions"," *IEEE Trans. Antennas Propag.*, vol. 38, no. 2, p. 227, 1990.

[79] E. Plum1, J. Zhou, J. Dong, V. A. Fedotov1, T. Koschny, C. Soukoulis, and N. I. Zheludev, "Metamaterial with negative index due to chirality," *Nature Material*, submitted,2008.

[80] S. O'Brien, D. McPeake, S. A. Ramakrishna, and J. B. Pendry, "Near-infrared photonic band gaps and nonlinear effects in negative magnetic metamaterials," *Phys. Rev. B*, vol. 69, p. 241101, Jun 2004.

[81] D. R. Smith, J. B. Pendry, and M. C. K. Wiltshire, "Metamaterials and negative refractive index," *Science*, vol. 305, no. 5685, pp. 788–792, 2004.

[82] C. M. Soukoulis, M. Kafesaki, and E. N. Economou, "Negative-index materials: New frontiers in optics," *Advanced Materials*, vol. 18, pp. 1941–1952, Aug 2006.

[83] S. Linden, C. Enkrich, G. Dolling, M. W. Klein, J. F. Zhou, T. Koschny, C. M. Soukoulis, S. Burger, F. Schmidt, and M. Wegener, "Photonic metamaterials: Magnetism at optical frequencies," *IEEE Journal of Selected Topics in Quantum Electronics*, vol. 12, pp. 1097–1105, Invited Paper,Dec 2006.

[84] V. M. Shalaev, "Optical negative-index metamaterials," *Nature Photonics*, vol. 1, no. 1, pp. 41–48, 2007.

[85] T. Koschny, L. Zhang, and C. M. Soukoulis, "Isotropic three-dimensional left-handed metamaterials," *Physical Review B (Condensed Matter and Materials Physics)*, vol. 71, no. 12, p. 121103, 2005.

[86] R. Marqués, F. Medina, and R. Rafii-El-Idrissi, "Role of bianisotropy in negative permeability and left-handed metamaterials," *Phys. Rev. B*, vol. 65, p. 144440, Apr 2002.

[87] W. S. Cai, U. K. Chettiar, H. K. Yuan, V. C. de Silva, A. V. Kildishev, V. P. Drachev, and V. M. Shalaev, "Metamagnetics with rainbow colors," *Optics Express*, vol. 15, no. 6, pp. 3333–3341, 2007.

[88] U. K. Chettiar, A. V. Kildishev, H. K. Yuan, W. S. Cai, S. M. Xiao, V. P. Drachev, and V. M. Shalaev, "Dual-band negative index metamaterial: double negative at 813nm and single negative at 772nm," *Optics Lett.*, vol. 32, no. 12, pp. 1671–1673, 2007.

[89] P. Markos and C. M. Soukoulis, *Wave Propagation: From Electrons to Photonic Crystals and Left-handed Materials*. New Jersey: Princeton University Press, 2008.

[90] M. Gorkunov, M. Lapine, E. Shamonina, and K. H. Ringhofer, "Effective magnetic properties of a composite material with circular conductive elements," *European Phys. J. B*, vol. 28, no. 3, pp. 263–269, 2002.

[91] J. F. Zhou, T. Koschny, M. Kafesaki, and C. M. Soukoulis, "Size dependence and convergence of the retrieval parameters of metamaterials," *Photonics Nanostructures-fundamentals Applications*, vol. 6, no. 1, pp. 96–101, 2008.

[92] C. M. Soukoulis, "Bending back light: The science of negative index materials," *Opt. Photon. News*, vol. 17, no. 6, pp. 16–21, 2006.

PUBLICATIONS[1] OF JIANGFENG ZHOU

1. S. Linden, C. Enkrich, M. Wegener, J. Zhou, T. Koschny, and C. M. Soukoulis, "Magnetic response of metamaterials at 100 terahertz," *Science*, vol. 306, pp. 1351–1353, Nov 2004.

2. **J. Zhou, T. Koschny, M. Kafesaki, E. N. Economou, J. B. Pendry, and C. M. Soukoulis, "Saturation of the magnetic response of split-ring resonators at optical frequencies," *Physical Review Letters*, vol. 95, no. 22, p. 223902, 2005.**

3. G. Dolling, C. Enkrich, M. Wegener, J. Zhou, and C. M. Soukoulis, "Cut-wire pairs and plate pairs as magnetic atoms for optical metamaterials," *Optics Letters*, vol. 30, pp. 3198–3200, Dec 2005.

4. C. Enkrich, R. Perez-Willard, D. Gerthsen, J. Zhou, T. Koschny, C. M.Soukoulis, M. Wegener, and S. Linden, "Focused-ion-beam nanofabrication of near-infrared magnetic metamaterials," *Advanced Materials*, vol. 17, pp. 2547–+, Nov 2005.

5. C. Enkrich, M. Wegener, S. Linden, S. Burger, L. Zschiedrich, F. Schmidt, J. Zhou, T. Koschny, and C. M. Soukoulis, "Magnetic metamaterials at telecommunication and visible frequencies," *Physical Review Letters*, vol. 95, no. 20, p. 203901, 2005.

6. **J. Zhou, L. Zhang, G. Tuttle, T. Koschny, and C. M. Soukoulis, "Negative index materials using simple short wire pairs," *Physical Review B (Condensed Matter and Materials Physics)*, vol. 73, no. 4, p. 041101, 2006.**

[1] Publications directly relevant to this thesis are typed in bold.

7. **J. Zhou, T. Koschny, L. Zhang, G. Tuttle, and C. M. Soukoulis, "Experimental demonstration of negative index of refraction," *Applied Physics Letters*, vol. 88, no. 22, p. 221103, 2006.**

8. **J. Zhou, E. N. Economon, T. Koschny, and C. M. Soukoulis, "Unifying approach to left-handed material design," *Opt. Lett.*, vol. 31, no. 24, pp. 3620–3622, 2006.**

9. S. Linden, C. Enkrich, G. Dolling, M. W. Klein, J. Zhou, T. Koschny, C. M. Soukoulis, S. Burger, F. Schmidt, and M. Wegener, "Photonic metamaterials: Magnetism at optical frequencies," *IEEE Journal of Selected Topics in Quantum Electronics*, vol. 12, pp. 1097–1105, Invited Paper,Dec 2006.

10. M. Kafesaki, T. Koschny, J. Zhou, N. Katsarakis, I. Tsiapa, E. N. Economou, and C. M. Soukoulis, "Electromagnetic behavior of left-handed materials," *Physica B*, vol. 394, p. 148, 2007.

11. **J. Zhou, T. Koschny, and C. M. Soukoulis, "Magnetic and electric excitations in split ring resonators," *Opt. Express*, vol. 15, no. 26, pp. 17881–17890, 2007.**

12. J. Zhou, T. Koschny, M. Kafesaki, and C. M. Soukoulis, "Size dependence and convergence of the retrieval parameters of metamaterials," *Photonics Nanostructures-fundamentals Applications*, vol. 6, no. 1, pp. 96–101, 2008.

13. **C. M. Soukoulis, J. Zhou, T. Koschny, M. Kafesaki, and E. N. Economou, "The science of negative index materials," *Journal of Physics: Condensed Matter*, vol. 20, no. 30, p. 304217, 2008.**

14. **J. Zhou, T. Koschny, and C. M. Soukoulis, "An efficient way to reduce losses of left-handed metamaterials," *Opt. Express*, vol. 16, no. 15, pp. 11147–11152, 2008.**